UQAC
Université du Québec
à Chicoutimi

Elevated-temperature mechanical, creep and fatigue behavior of aluminum-copper cast aluminum alloys

By

Peng Hu

Under the supervision of Prof. X.-Grant Chen, co-supervision of Prof. Kun Liu and industrial supervision of Dr. Lei Pan

Manuscript-Based Thesis presented to the University of Quebec at Chicoutimi with a view to obtaining the degree of Philosophy Doctor (Ph. D.) in Engineering.

Defended on 30 November 2023

BOARD OF EXAMINERS:

Prof. Dilip Sarkar, department of Applied Sciences at UQAC, President of the board of examiners

Dr. Alexandre Maltais, Rio Tinto Aluminum, Saguenay, Quebec, External Member of examiners

Prof. Zhan Zhang, department of Applied Sciences at UQAC, Internal Member of examiners

Prof. X.-Grant Chen, department of Applied Sciences at UQAC, Internal Member of examiners

Prof. Kun Liu, department of Applied Sciences at UQAC, Internal Member of examiners

Québec, Canada

Résumé

Les alliages coulés en aluminium ont gagné une utilisation extensive dans l'industrie automobile en tant que substituts de la fonte grise dans la fabrication de composants cruciaux des moteurs à combustion, y compris les blocs moteurs et les culasses. Notamment, les alliages coulés Al-Cu ont attiré une attention substantielle pour leur application dans les moteurs à combustion interne en raison de leur rapport élevé résistance-poids et de leurs performances mécaniques supérieures, à la fois à température ambiante et à température élevée. Cependant, les avancées continues dans la technologie des moteurs nécessitent un fonctionnement dans des conditions élevées, notamment des températures de fonctionnement élevées (~300 °C) et des pressions de combustion améliorées (~200 bars). Par conséquent, il est nécessaire d'améliorer davantage les caractéristiques à température élevée, notamment la résistance, la résistance au fluage et l'endurance à la fatigue, des alliages Al-Cu pour répondre aux exigences évolutives des moteurs futurs. Des enquêtes récentes ont révélé que les propriétés à haute température des alliages Al-Cu peuvent être considérablement améliorées par microalliage. Ainsi, ce projet se concentre sur l'incorporation d'éléments de microalliage, notamment le magnésium et les éléments de transition (titane, zirconium, vanadium), pour examiner de manière approfondie leur influence sur les propriétés à température élevée des alliages coulés Al-Cu 224.

Dans la première partie, l'influence du microalliage avec Mg (0-0,36 % en poids) sur la résistance à température élevée et la résistance au fluage des alliages coulés Al-Cu 224 a été étudiée. Les alliages contenant du Mg ont donné des précipités θ′ plus fins et plus denses après une stabilisation à haute température (300 °C/100 h) que l'alliage sans Mg, ce qui a amélioré la limite d'élasticité à la fois à température ambiante et à 300 °C. Des tests de fluage en compression ont été menés à 300 °C sur une large gamme de contraintes appliquées (45-100 MPa). Les résultats ont montré que la résistance au fluage augmentait avec la teneur croissante en Mg à toute contrainte appliquée fixe, et l'alliage avec 0,36 % en poids de Mg présentait la meilleure résistance au fluage parmi les quatre alliages étudiés. Pendant la déformation de fluage, les précipités θ′ continuaient à grossir. Cependant, le microalliage au Mg stabilisait considérablement les précipités θ′ dans la matrice en ralentissant le processus de grossissement. Une rupture évidente a été observée dans les courbes de taux de fluage avec différents exposants de contrainte (n). En dessous de la rupture dans le régime de faible contrainte (LSR), l'exposant de contrainte (n) était d'environ 3, tandis qu'il augmentait à 9-12 au-dessus de la rupture dans le régime de haute contrainte (HSR). Dans le LSR, le fluage était contrôlé par la montée de la dislocation, et il se transformait en bouclage d'Orowan dans le HSR.

Dans la deuxième partie, les effets des ajouts individuels et combinés d'éléments de transition (TE) Zr, Ti et V sur l'évolution de la microstructure et les propriétés mécaniques et de fluage à température élevée des alliages coulés Al-Cu 224 ont été étudiés. Tous les alliages avaient une microstructure de précipités mixtes θ″- et θ′-Al_2Cu après un traitement thermique T7. Pendant l'exposition thermique à 300 °C, θ″ se transformait en θ′ en tant que phase de renforcement prédominante. La résistance au

grossissement de θ′ pendant l'exposition thermique et la déformation par fluage ultérieure étaient grandement améliorées par l'addition d'ET. Individuellement, l'ajout de Zr a démontré la meilleure efficacité pour stabiliser θ′, tandis que la combinaison Zr + V et Ti + Zr + V a atteint la plus haute efficacité. L'addition d'ET a généralement amélioré la limite d'élasticité (LE) à 300 ℃, et les alliages ZrV et TiZrV ont atteint la LE la plus élevée. Une corrélation étroite entre la LE et la distribution et la stabilité thermique de θ′ a été observée. La résistance au fluage à des températures élevées a été affectée par la stabilité thermique de θ′ et la taille des grains. Les alliages contenant du Zr (ZrV, Zr et TiZrV) présentent une résistance au fluage supérieure. En termes de propriétés globales, l'addition combinée de l'alliage TiZrV a présenté la meilleure performance à température élevée.

Dans la troisième partie, les effets de l'ajout de Mg sur les comportements de déformation cyclique et de durée de vie en fatigue des alliages coulés Al-Cu 224 ont été étudiés lors de la fatigue cyclique isotherme à 300 ℃ et de la fatigue thermomécanique hors phase (OP-TMF) dans la plage de température de 60 à 300 ℃. Les résultats montrent que tous les alliages testés ont subi un ramollissement cyclique à la fois lors de la LCF et de l'OP-TMF, tandis que le rapport de ramollissement des alliages contenant du Mg était inférieur à celui de l'alliage de base sans Mg en raison du taux de grossissement plus faible des précipités θ'-Al_2Cu. À la fois en LCF et en TMF, la porosité en surface et les particules intermétalliques cassantes étaient considérées comme sources d'amorçage de fissures. Les durées de vie en TMF étaient inférieures aux durées de vie en LCF pour la même amplitude de contrainte en raison de l'effet combiné des dommages dus aux charges mécaniques et thermiques cycliques. En LCF, l'ajout de Mg a amélioré les performances en fatigue en raison de la coexistence des précipités θ″ et θ′ et de la résistance thermique supérieure de θ′; en TMF, il a conduit à une légère réduction des performances en fatigue. Le modèle d'énergie d'hystérésis a été appliqué avec succès pour prédire les durées de vie en LCF et en TMF. Les résultats prédits concordent bien avec les durées de vie en LCF et en TMF mesurées expérimentalement.

Abstract

Aluminum cast alloys have gained extensive utilization within the automotive industry as substitutes for gray cast iron in the fabrication of crucial combustion engine components, including engine blocks and cylinder heads. Notably, Al–Cu cast alloys have garnered substantial attention for their applications in internal combustion engines due to their high strength-to-weight ratio and superior mechanical performance, both at ambient and elevated temperatures. However, the ongoing advancements in engine technology necessitate operation under elevated conditions, including high operating temperatures (~300 ℃) and enhanced combustion pressures (~200 bar). Consequently, this arises a need to further enhance the elevated-temperature performances, encompassing strength, resistance to creep, and fatigue endurance, of Al-Cu alloys to align with the evolving demands of future engines. Recent investigations have revealed that the high-temperature properties of Al-Cu alloys can be significantly improved by microalloying. Hence, this project focuses on the incorporation of microalloying elements, specifically magnesium and transition elements (titanium, zirconium, vanadium), to comprehensively investigate their influence on the elevated-temperature properties of Al-Cu 224 cast alloys.

In the first part, the influence of microalloying with Mg (0–0.36 wt.%) on the elevated-temperature strength and creep resistance of Al-Cu 224 cast alloys was investigated. The Mg-containing alloys yielded finer and denser θ′ precipitates after high-temperature stabilization (300 ℃/100 h) than the Mg-free alloy, which improved the yield strength at both room temperature and 300 ℃. Compressive creep tests were conducted at 300 ℃ over a wide range of the applied stresses (45–100 MPa). The results showed that the creep resistance increased with increasing Mg content at any fixed applied stress, and the alloy with 0.36 wt.% Mg exhibited the best creep resistance among the four alloys studied. During creep deformation, the θ′ precipitates continued to coarsen. However, Mg microalloying greatly stabilized the θ′ precipitates in the matrix by slowing down the coarsening process. An obvious break was observed in the creep rate curves with different stress exponents (n). Below the break in the low-stress regime (LSR), stress exponent (n) was ~ 3, whereas it increased to 9-12 above the break in the high-stress regime (HSR). In the LSR, the creep was controlled by the dislocation climbing, and it transformed into the Orowan looping in the HSR.

In the second part, the effects of individual and combined additions of transition elements (TEs) Zr, Ti, and V on the microstructure evolution and elevated-temperature mechanical and creep properties of Al-Cu 224 cast alloys were investigated. All alloys had a mixed precipitate microstructure of θ″- and θ′-Al_2Cu after T7 heat treatment. During the thermal exposure at 300 ℃, θ″ transferred into θ′ as the predominant strengthening phase. The coarsening resistance of θ′ during the thermal exposure and further creep deformation was greatly improved by the addition of TEs. Individually, Zr addition demonstrated the best efficiency in stabilizing θ′, while the combination of Zr + V and Ti + Zr + V achieved the highest efficiency. The addition of TEs generally improved the yield strength (YS) at 300 ℃, and the ZrV and TiZrV alloys achieved the highest YS. A close correlation between the YS and the distribution and thermal

stability of θ′ was observed. The creep resistance at elevated temperatures was affected by the thermal stability of θ′ and grain size. Zr-containing alloys (ZrV, Zr, and TiZrV) exhibit superior creep resistance. In terms of comprehensive properties, the combined addition of TiZrV alloy exhibited the best elevated-temperature performance.

In the third part, the effects of Mg addition on the cyclic deformation and fatigue life behaviors of Al-Cu 224 cast alloys were investigated under isothermal low cycle fatigue (LCF) at 300 ℃ and out-of-phase thermo-mechanical fatigue (OP-TMF) in the temperature range 60–300 ℃. The results show that all tested alloys experienced cyclic softening during both LCF and OP-TMF, whereas the softening ratio of Mg-containing alloys was lower than that of the base alloy free of Mg because of the lower coarsening rate of θ'-Al_2Cu precipitates. Under both LCF and TMF, near-surface porosity and brittle intermetallic particles were considered sources of crack initiation. TMF lives were inferior to LCF lives under the same strain amplitude because of the combined damage effect of the cyclic mechanical and thermal loadings. Under LCF, the addition of Mg enhanced the fatigue performance because of the co-existing θ″ and θ′ precipitates and the higher thermal resistance of θ′; under TMF, it led to a slight reduction in fatigue performance. The hysteresis energy model was successfully applied to predict the LCF and TMF lifetimes. The predicted results agree well with the experimentally measured LCF and TMF lifetimes.

Table of Contents

List of Tables

List of Figures

List of Symbols

Al	Aluminum
Si	Silicon
Cu	Copper
Fe	Iron
Mn	Manganese
Ni	Nickle
Cr	Chromium
Sr	Strontium
Na	Sodium
Ti	Titanium
V (element)	Vanadium
Zr	Zirconium
Sc	Scandium
Mg	Magnesium
La	Lanthanum
Co	Cobalt
Sn	Tin
Ag	Silver
B	Boron
Ar	argon
°C	temperature unit on Celsius scale
K	temperature unit on Kelvin scale
bar	unit of pressure
T	temperature

T_M	absolute melting temperature
ε	steady-state creep rate
σ	stress
σ_{Or}	Orowan stress
λ	interparticle spacing
d	average particle diameter
N_v	number density
t_t	measured thickness of the precipitate
b	Burger's vector
ν	Poisson's ratio
G	shear modulus.
A	material constant
n	stress exponent
Q	apparent activation energy
R	ideal gas constant
N	number of cycles
α-Al	matrix of aluminum
wt.%	weight percentage
at%	atomic percentage
h	hour
min	minute
s	second
mm	millimeter
μm	micrometer
nm	nanometer

V (unit)	voltage
kV	kilovolt
ml	milliliter
%	percentage
θ″	theta double prime phase
θ′	theta prime phase
θ	equilibrium theta phase
γ	gamma prime phase
MPa	Megapascal
N_f	fatigue life of materials
$\Delta\sigma/2$	stress amplitude
$\sigma_{f'}$	fatigue strength coefficient
b	fatigue strength exponent
$\Delta\varepsilon_p/2$	plastic strain amplitude
$\Delta\varepsilon_t/2$	total strain amplitudes
$\varepsilon_{f'}$	fatigue ductility coefficient
c	fatigue ductility exponent
R_ε	strain ratio
$\Delta\sigma_{max}$	maximum stress amplitude
$\Delta\sigma_{half}$	stress amplitude at the half lifetime
D_i	damage parameter of the ith cycle
W_i	hysteresis energy of the ith cycle
W_o	intrinsic fatigue damage capacity
W_s	saturation hysteresis energy
β	fatigue damage exponent

List of Abbrevations

GBS	grain boundary sliding
SDAS	secondary dendrite arm spacing
FCP	fatigue crack propagation
LSR	low-stress regime
HSR	high-stress regime
OM	optical microscopy
SEM	scanning electron microscopy
TEM	transmission electron microscopy
EDS	energy-dispersive X-ray spectroscopy
SADP	selected area diffraction pattern
CBED	two-beam convergent beam diffraction pattern
SSS	supersaturated solid solution
GP	Guinier Preston
TEs	transition elements
YS	yield strength
LCF	low cycle fatigue
HCF	high cycle fatigue
TMF	thermomechanical fatigue
OP	out-of-phase
IP	in-phase
SR	softening ratio
LPF	life prediction factor
ACMZ	Al-6.1Cu-0.42Mn-0.15Zr

Dedication

I wholeheartedly dedicate this thesis to my loving parents, Xueli Hu and Cuiying Xiang. Their unwavering support and encouragement have been a constant source of strength, and I am forever grateful for their love and understanding.

In addition, I extend a special dedication to my dear wife, Liying Cui. Her constant companionship, love, support, and understanding have been the pillars that propel me forward, even during the most challenging times.

Finally, this thesis is dedicated to my esteemed supervisors, Prof. X.-Grant Chen, Prof. Kun Liu, and Dr. Lei Pan. Their invaluable guidance and expertise have shaped my research and pushed me to be a better scholar.

Acknowledgements

I would like to take this moment to extend my heartfelt gratitude to those individuals who have provided invaluable assistance, encouragement, and support throughout my Ph.D. journey at the University of Quebec at Chicoutimi (UQAC).

Foremost, I wish to convey my sincere appreciation to my supervisor, Prof. X.-Grant Chen, for affording me the opportunity to pursue my studies in Canada. His expert guidance, unwavering support, and insightful mentorship have not only enriched my research but have also fostered my growth as a dedicated researcher. His academic prowess, innovative thinking, and forward-looking approach have been a constant source of inspiration throughout my Ph.D. tenure.

Equally significant, I extend my deep gratitude to my co-supervisor Prof. Kun Liu and industrial supervisor Dr. Lei Pan, whose consistent guidance, encouragement, and timely assistance have been instrumental in the successful completion of this thesis. Their invaluable contributions and counsel have played a pivotal role in shaping my research endeavors.

I am also indebted to Prof. Mousa Javidani for his invaluable insights and support in the realm of academic research. I extend my appreciation to Prof. Zhang for imparting his expertise in TEM and SEM training, as well as his invaluable suggestions for microstructure characterization. Gratitude is also extended to Prof. Emad Elgallad for his guidance in DSC training, and to Mr. Zhixing Chen for his dedicated experimental training and assistance.

I would like to express my sincere thanks to the dedicated technicians of CURAL, namely Dany Racine, Samuel Dessureault, and Félix Tremblay, whose unwavering assistance and support have greatly contributed to the success of my Ph.D. studies.

Additionally, I extend my gratitude to my colleagues at CURAl, whose collaborative efforts, scientific insights, and unwavering support have enriched my research journey. I would like to mention Jovid Rakhmonov, Mohamed Qassem, Ahmed Y. Al-Gendy, Ali Elashery, Mohammadreza Mofarrehi, Siamak Nikzad Khangholi, Mohamed Ahmed, Zimeng Wang, Chaima Hajji, Liying Cui, Shuai Wang, Cong Li, Dong Li, Mani Mohan Tiwari, Abhishek Ghosh, Esmaeil Pourkhorshid, Quan Shao, Alyaa Aly, Mohammad Khoshghadam, Farnaz Yavari, Behrouz Abnar, Ali Faraj, Layla Mohammadzadeh, Musa Muhammed, Siavash Imanian Ghazanlou, Xavier Tremblay, and Eric Kojo Kweitsu. Their camaraderie and collective efforts have truly enriched my academic journey.

Above all, I am profoundly grateful for the unwavering support, consistent encouragement, and strength provided by my parents and my wife. Their steadfast belief in me has been an unwavering pillar of support throughout my Ph.D. endeavor.

I extend my sincere appreciation to all the sponsors who have played a crucial role through their financial contributions and collaborative efforts. Specifically, my gratitude goes to the Natural Science and Engineering Research Council of Canada

(NSERC) and Rio Tinto Aluminum through the NSERC Industry Research Chair in the Metallurgy of Aluminum Transformation at Université du Québec à Chicoutimi (UQAC).

Finally, I wish to reiterate my profound gratitude to all those who have contributed to the completion of my successful thesis. Your support has been instrumental, and I am truly grateful for the roles you have played in my academic journey.

Chapter 1

Introduction

1.1 Background

1.1.1 Application of aluminum alloys in automobile industry

In recent years, there has been intense focus on employing aluminum alloys for critical engine components, notably engine blocks and cylinder heads. The transition from cast iron to aluminum cylinder heads offers several vital advantages [1]:

1. An aluminum engine block typically exhibits a notable weight reduction of 40% to 55% compared to an equivalent gray cast iron block, contributing to the weight reduction.
2. The casting and machining of aluminum alloys necessitate lower energy and costs, augmented by a high degree of recycling that further contributes to cost reduction.
3. Aluminum alloys exhibit a substantial thermal conductivity advantage, ranging from three to four times higher than that of gray cast iron. This characteristic renders them particularly appealing for cylinder head applications.
4. Replacement of cast iron with aluminum blocks and cylinder heads can effectively lower the engine's center of gravity within a vehicle, thereby enhancing its maneuverability and handling characteristics.

However, it should be noted that there are several primary disadvantages associated with applying aluminum in car engines. These include lower stiffness,

susceptibility to high-temperature creep deformation, and inferior wear characteristics [1]. Thus, special design considerations including ambient and elevated-temperature strength, creep and fatigue resistance should be taken into consideration.

The predominant aluminum cast alloys utilized for engine components encompass the Al-Si (e.g., 356/A356) and Al-Si-Cu (e.g., 319/A319) alloy series [2, 3]. Nonetheless, current engine developments necessitate elevated operating temperatures (~300 ℃) and higher combustion pressures (~200 bar) [4]. The inadequate high-temperature performances exhibited by Al-Si and Al-Si-Cu cast alloys (such as 356/319 types) make them unsuitable for future engine requirements, limiting their application temperature to below 250 ℃ [5-7]. Conversely, Al-Cu cast alloys with superior elevated-temperature properties present promising alternatives for structural engine components [8-10]. Therefore, the Al-Cu 224 cast alloys were selected as the experimental materials to investigate its mechanical behavior, creep performance, and fatigue characteristics at elevated temperatures.

1.1.2 Creep deformation

1.1.2.1 Definition

The phenomenon of material creep, occurring under conditions of constant temperature, is characterized by a gradual and substantial permanent inelastic deformation over an extended duration due to sustained exposure to constant stresses that remain below the material's yield strength. This intricate phenomenon of creep is observed to occur when the operational temperature (T) surpasses a critical range of 0.3 to 0.5 times the absolute melting temperature (T_M). Experimental investigations

concerning creep are conventionally conducted through the test of tension, compression, or torsion, whereby the material is subjected to either constant stress or a consistent load. The tests under constant stress offer insights into the fundamental mechanisms governing creep, while constant-load stress provide perspectives from an engineering standpoint. Throughout the experimental procedure, the temperature remains unchanged, and a continuous record of elongation is maintained.

A typical creep response curve, as depicted in Fig. 1.1, can be divided into three stages: primary creep, secondary creep, and tertiary creep [11]. Primary creep occurs subsequently after the initial instantaneous deformation, wherein the rate of creep exhibits a decline over time. This stage is characterized by an augmentation in the material's resistance to creep deformation due to strain hardening, resulting in the slowdown of creep rate. The subsequent stage, termed secondary creep, is highlighted by a consistent creep rate provided by the equilibrium established between thermal recovery and strain hardening. As the progression of creep deformation advances, this equilibrium becomes disrupted, leading to the inception of tertiary creep. In this stage, the creep rate experiences a rapid escalation culminating in eventual rupture.

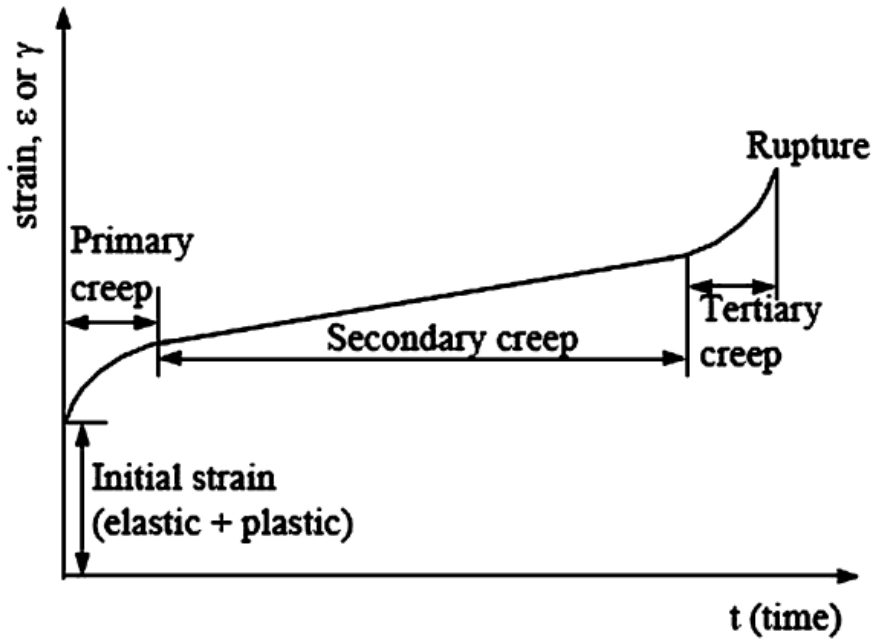

Fig. 1.1 A typical creep curve of metal or alloy [12].

The minimum rate of plastic deformation observed in a creep test after the application of load is termed secondary creep rate or steady-state creep [12, 13]. The steady-state creep rate (ε), as a function of stress (σ) and temperature (T) at elevated temperatures can be described by Equation 1.1 [14-16]:

$$\varepsilon = A\sigma^n \exp\left(\frac{-Q}{RT}\right) \quad (1.1)$$

where A is the material constant, n is the stress exponent, Q is the apparent activation energy, and R is the ideal gas constant.

1.1.2.2 Creep mechanisms

Creep deformation varies according to different temperature and stress intervals, depending on the subsequent different processes:

1. Dislocation creep

Dislocation creep is caused by the progressive propagation of dislocations throughout the crystalline lattice, delineated concerning both their interaction with the encompassing crystal and their relative movement. This movement transpires along a designated glide plane, effectively segregating the crystal into distinct regions. This migration necessitates the rupture of all interatomic bonds within the plane, consequently producing the expectation that this advancement is facilitated through the cleavage of bonds, succeeded by the establishment of fresh bonds with minimal energy requisites. This mechanism gives rise to the formation of a linear lattice defect recognized as a dislocation. The dislocation, characterized by its capacity for traversal within the crystal lattice, persists until it encounters a grain boundary, subsequently culminating in its dissolution, thereby causing the shearing of the entire crystal. Factors that affect the movement of dislocation encompass diverse ways. The anisotropic properties of certain materials contribute to the phenomenon wherein dislocations, move along multiple glide planes, exhibit different velocities depending on the specific plane traversed. Furthermore, dislocations encounter an array of obstacles during their trajectory, including interactions with other dislocations or point defects, which can slow down or even stop moving altogether [12].

2. Diffusion creep

Diffusion creep denotes the plastic deformation observed in crystalline solids, wherein vacancy diffusion within the crystal lattice serves as the underlying mechanism. This deformation process exhibits increased sensitivity to temperature and ensues from the migration of crystalline defects through the lattice structure. When an anisotropic compression force is applied to the crystal, inducing greater compression

in one direction compared to another, these defects migrate to the crystal's faces aligned with the compression axis. This relocation of defects generates a net mass transfer, thereby causing a reduction in the crystal's dimension along the axis of maximum compression [12].

This migration of defects is because of the movement of vacancies, wherein the migration of vacancies corresponds to the net mass transfer in the opposing direction. In polycrystalline materials subjected to external stress, tensile stress impacts vacancies along grain boundaries, while compressive stress leads to a reduction in vacancies. The resulting flow of vacancies driven by stress and aimed at reestablishing equilibrium, is identified as diffusion creep. This vacancy flux induces elongation within individual grains along the axis of tensile loading, concurrently prompting the accumulation of particles at grain boundaries that align parallel to the tensile axis. Conversely, a reduction in particle concentration is evident at boundaries perpendicular to the axis of tensile loading [17].

3. Grain boundary sliding

Grain boundary sliding (GBS) includes inter-grain displacement that occurs at elevated temperatures and low strain rates. Within this process, crystalline entities undergo mutual sliding, with no alteration in their intrinsic crystal geometry. Consequently, the resultant grain structure and textural arrangement in the deformed product are closely like those of the initial material. This phenomenon of grain boundary sliding is facilitated either through dislocation or diffusive mechanisms. Notably, when an array of elongated grains aligns in a contiguous manner, the

propensity for deformation via grain boundary sliding is enhanced. Such elongated grains possess a mechanical interdependence that instigates their rotation in response to applied stress—a mechanical characteristic not shared by spherical grains.

Several strategies can be proposed for enhancing the creep resistance of aluminum alloys based on the creep mechanism mentioned above. These approaches encompass: (i) the improvement of the stabilization of precipitates in precipitation-hardening alloys to weaken coarsening at elevated temperatures [18-21], (ii) the introduction of thermally durable dispersoids within the matrix [22-24], and (iii) the introduction of secondary phases along grain boundaries, aiming at impeding grain boundary sliding [12, 15].

1.1.3 Fatigue damage

1.1.3.1 Fatigue fracture mechanism

Within the domain of materials science, fatigue is the gradual deterioration of a material caused by repetitive loading, leading to progressive and localized structural deterioration alongside the propagation of cracks. The duration of fatigue lifetime until failure consists of two distinct phases: the initial stage characterized by crack initiation and the subsequent phase denoting the growth of the crack.

Fatigue crack initiation and propagation arise as consequences of cyclic slip, which corresponds to cyclic plastic deformation or dislocation movements. The occurrence of fatigue happens under stress amplitudes below the yield stress threshold. Within this lower stress regime, plastic deformation is confined to a limited subset of

material grains, particularly those positioned near the material's surface. This microplasticity predominantly occurs in surface grains due to the reduced constraints imposed on the slip. On the free surface of a material, one side interfaces interact with the material itself while the other side is with the surrounding environment, typically in the form of a gaseous (e.g., air) or liquid (e.g., seawater) medium. Consequently, the plastic deformation within surface grains experiences fewer constraints from neighboring grains compared to subsurface grains, thereby enabling deformation at lower stress levels. Fatigue phenomena occurs primarily at the material's surface in the initial phase of crack initiation [25].

Throughout the subsequent crack growth phase, the presence of microcracks contributes to a non-uniform stress distribution at a microscale, resulting in a stress concentration at the microcrack tip. Consequently, the microcrack becomes more susceptible to further enlargement due to the augmented stress concentration at its tip. The resistance to crack growth, once the crack penetrated the material, is intrinsically reliant on the material's bulk properties. Thus, crack growth transforms from a surface-centric phenomenon to one that operates within the material's volume [25].

The stage of crack propagation is characterized by the gradual, continuous expansion of the crack until it ultimately attains a critical size incapable of withstanding the applied load. At this juncture, the material undergoes an abrupt and catastrophic failure, recognized as the final fracture.

1.1.3.2 Types of fatigue regime

Fatigue behavior can be categorized based on loading conditions and the number of cycles leading to failure, delineated as follows:

High-cycle fatigue (HCF) encompasses a substantial volume of cycles ($N > 10^5$ cycles) under elastically applied stress conditions. Tests for HCF are typically conducted for 10^7 cycles, occasionally extending to 5×10^8 cycles for nonferrous metals. Despite the applied stress remaining within the elastic realm, localized plastic deformation can occur at the crack tip [26].

Distinct from HCF, the issue of low-cycle fatigue (LCF) exhibits unique characteristics. While HCF on a macroscopic scale occurs within the elastic domain, LCF is typified by macroscopic plastic deformation transpiring in each cycle. Under LCF, failure may happen within a modest cycle count, such as 1000 cycles or less. The inception of small cracks is expedited, and due to the elevated stress levels, ultimate failure materializes while the cracks remain small. Manifestations of visible crack propagation are seldom observed. Under constant-amplitude loading conditions, LCF leads to pronounced plastic deformation during the initial cycle, succeeded by substantially diminished strain amplitudes in subsequent cycles.

Thermomechanical fatigue (TMF) arises due to the combination of thermal and mechanical loading, wherein stress, strain, and temperature dynamically fluctuate. Such loading profiles often inflict greater damage compared to conditions of isothermal loading. The conditions conducive to thermomechanical fatigue are commonly encountered during the operational cycles of high-temperature components

and equipment, particularly during the start-up and shut-down phases. In a TMF test, two primary cycles are typically employed: (a) the in-phase cycle (IP), characterized by the same phase of mechanical and thermal strains (e.g., maximum strain aligning with maximum temperature); and (b) the out-of-phase cycle (OP), wherein maximum mechanical strain coincides with minimal temperature. In-phase loading is prone to inducing creep damage under tensile stresses at elevated temperatures. Conversely, out-of-phase loading is more likely to trigger oxidation damage, as an oxide film could develop under compression at higher temperatures and subsequently fracture during the subsequent low-temperature tensile phase of the loading cycle, where the oxide film becomes more brittle [27].

During the service of cylinder heads, the mechanics underlying fatigue failure can be elucidated as follows. Upon engine ignition, the valve bridge undergoes heating, elevating the temperature to a notable extent (exceeding 523 K) concerning the circumference of the combustion chamber. The bridge segment is inclined to expand, despite being constrained by a fixed water-cooled flame deck. This constraint produces a localized compressive stress field within the bridge section, consequently prompting compressive yielding. The maximum stress arises when the temperature differential between the combustion chamber and the water-cooled flame deck attains its highest point, particularly at maximum operational speed. However, upon engine shutdown, the bridge segment contracts while cooling back to ambient temperature. The regions that underwent yielding are unable to revert to their initial state, resulting in the emergence of tensile stresses within these sectors [28-30]. Consequently, the stress distribution within the yielded regions of the cylinder head is compressive at elevated

temperatures but becomes tensile as temperatures decline. Consequently, the cylinder head is perceived to be subjected to out-of-phase thermomechanical fatigue (OP-TMF) loading, thus, this kind of fatigue regime was chosen to investigate in this study.

1.1.3.3 Factors affecting fatigue resistance

1) Casting defects

Most castings typically encompass a combination of oxide films and pores, varying in types and sizes. The presence of casting defects in aluminum castings intricately complicates the interaction among different stages of fatigue failure. According to fracture mechanics principles, the existence of a solitary defect leads to stress concentration within the adjacent matrix. In cases where a defect of a specific size is considered, the stress intensity factor experiences an approximate 55% increase if the defect is positioned at the free surface, as opposed to being positioned at the center of the sample [31]. This concentrated stress around the defect accelerates the onset of crack initiation. The fatigue characteristics of a material are closely linked to the dimensions of defects: larger defect sizes correlate with diminished fatigue lifetime. When evaluating defects of a given size, porosity seems to exert a more detrimental influence on fatigue life in comparison to oxide films, despite the sharper nature of cracks originating from oxide films compared to the curvature of pores [32, 33].

2) Secondary dendrite arm spacing

Secondary dendrite arm spacing (SDAS) is employed to characterize the extent of equiaxed dendritic formations. The dimension of SDAS predominantly relies on cooling-curve parameters such as the cooling rate, overall solidification period, and

temperature conditions. Generally, smaller SDAS values correlate with enhanced fatigue performance, while augmented SDAS values correlate with reduced fatigue resistance [34]. This correlation can be ascribed to the fact that reduced SDAS values yield a more uniform microstructure with fewer defects and diminished property variability. Consequently, this produces a more uniform distribution of stresses during repetitive loading, thereby enhancing the material's resistance to fatigue-induced failure [35].

3) Intermetallic phases

Aluminum alloys frequently exhibit pronounced clustering of intermetallic phases [36, 37]. These intermetallics, particularly in the form of sizable clusters, can exert a notable detrimental impact on the alloys' susceptibility to fatigue cracking [38-40]. Mechanical characterization of these phases reveals their distinctively heightened stiffness and hardness compared to the α-Al matrix [41], consequently subjecting them to elevated stresses due to load distribution. Particles like eutectic Si particles [42-45] and primary Si particles [39, 46] and diverse intermetallic compounds such as β-Al_5SiFe [47], α-$Al_{15}(FeMn)_3Si_2$ [48], Al_9FeNi [49], and $Al_3(NiCu)_2$ [39, 46, 50] are anticipated to actively contribute to the initiation and progression of fatigue cracks. Their involvement relies on factors like interface failure or fracture mechanisms, depending on their dimensions, morphology, and alignment relative to the loading axis [39, 51].

4) Chemical composition-alloying and impurity elements

Firstly, the addition of various trace elements has demonstrated the capability to alter brittle phases and enhance fatigue resistance. For instance, the β-Al_5SiFe phase within the Al-Si alloy has been identified as susceptible to crack propagation and fracture [3, 47]. Nevertheless, the introduction of elements like Mn and Cr facilitates the transformation of the β-Al_5SiFe phase into the less detrimental α-Al_8Fe_2Si phase [52, 53]. Furthermore, certain trace elements, such as Sr and Na, exert a modifying influence on the Al-Si eutectic microstructure, consequently enhancing fatigue performance [54, 55]. Additionally, certain microalloying elements (such as Mn, Mg, Ti, Zr, V, and Sc) [8, 56-63] exhibit the potential to enhance high-temperature strength and subsequently improve fatigue behavior.

5) Precipitates and dispersoids

The second phases present in aluminum alloys can be categorized into three primary groups [64, 65]: (a) Inclusions, characterized by their relatively large particle size (>5 μm), consist of impurities originating from the manufacturing process, such as aluminum oxide and other compounds derived from the slag. (b) Dispersoids, defined as thermodynamically stable particles within the size range of 0.1 to 1 μm, precipitate during thermomechanical processing and exhibit resistance to dissolution at solution heat treatment temperatures, as typically associated with subsequent tempering treatments. (c) Precipitates, generated through controlled precipitation of hard particles via TMP (Thermomechanical Processing), reintegrate into the matrix at elevated temperatures.

Dispersoids and precipitates can significantly impact both the crack initiation and crack propagation phases of fatigue failure, through contradictory roles [64, 65]. These second-phase particles are typically hard intermetallic compounds with distinct elastic and plastic deformation behaviors compared to the metallic aluminum matrix. Fine non-shearable particles, responsible for inducing dislocations to bypass them through looping mechanisms, facilitate dislocation distribution by encouraging non-planar slip. This reduces dislocation pileups and consequently retards crack initiation. On the other hand, shearable particles promote planar slip, facilitating crack closure, crack branching, crack deflection, and slip reversal during stress reversals. As a result, they contribute to a decrease in the fatigue crack propagation (FCG) rate. Hence, the simultaneous enhancement of fatigue resistance and FCP resistance could potentially be achieved through a bimodal combination of shearable and non-shearable strengthening precipitates and/or dispersoids, offering a promising method for improvement [66].

1.2 Problem statement

Owing to the increasing scarcity of non-renewable resources and the need for environmental protection, the enhancement of engine efficiency and reduction of fuel consumption have attracted widespread attention. An effective strategy involves diminishing engine weight, a path that has promoted the increasing utilization of aluminum cast alloys in place of grey cast iron for vital combustion engine components such as engine blocks and cylinder heads. This shift is attributed to the advantageous attributes of aluminum alloys, including their notable strength-to-weight ratio, castability, and thermal conductivity. Normally, a higher engine efficiency requires more rigorous operational conditions, characterized by elevated temperatures and pressures [4]. Consequently, the application of widely employed Al-Si and Al-Si-Cu aluminum cast alloys are limited due to their thermal instability at high temperatures (> 250 ℃) [5-7]. In contrast, Al-Cu alloys with better high-temperature performances [8-10] emerge as promising alternatives worthy of consideration for structural engine component applications.

In light of more demanding conditions within the combustion engine, the significance of high-temperature properties such as strength, creep resistance, and fatigue resistance in cast aluminum alloys becomes critical. Recent research has demonstrated the efficacy of microalloying in enhancing the thermal stability of precipitates as a method for effectively enhancing the high-temperature properties of precipitation-strengthened aluminum alloys [15-18]. Despite this, there is a scarcity of studies investigating the impact of micro alloying elements on the behavior of Al-Cu alloys at elevated temperatures, particularly in relation to elevated-temperature creep,

low-cycle fatigue (LCF), and thermo-mechanical fatigue (TMF). Consequently, the present study aims to conduct a comprehensive investigation into the influence of microalloying with magnesium (Mg) and transition elements (TEs) on the mechanical, creep, and fatigue behavior of Al-Cu alloys at elevated temperatures.

1.3 Objectives

The general objective of this study is to investigate how the micro alloying elements, Mg and transition elements, impact the elevated-temperature performances (such as thermal resistance, yield strength, creep resistance, LCF and TMF) of the Al-Cu alloy. To attain this general goal, we have delineated specific objectives that revolve around selecting experimental conditions and influential parameters. These objectives for each subproject can be outlined as follows:

Part 1: Effect of Mg microalloying on elevated-temperature creep resistance of Al–Cu 224 cast alloys

a. Investigate the influence of Mg microalloying on the elevated-temperature strength of Al–Cu 224 cast alloys.
b. Investigate the impact of Mg microalloying on the elevated-temperature creep resistance of Al–Cu 224 cast alloys.
c. Study the creep mechanism under different loadings.

Part 2: Effects of individual and combined additions of transition elements (Zr, Ti and V) on the microstructure stability and elevated-temperature properties of Al–Cu 224 cast alloys

a. Investigate the effect of transition elements on the microstructure stability of Al–Cu 224 cast alloys.
b. Investigate the influence of transition elements on the elevated-temperature mechanical properties of Al–Cu 224 cast alloys.

c. Investigate the impact of transition elements on the elevated-temperature creep behavior of Al–Cu 224 cast alloys.

Part 3: Effect of Mg on the elevated-temperature low cycle fatigue and thermo-mechanical fatigue behaviors of Al-Cu cast alloys

a. Investigate the influence of Mg microalloying on the elevated-temperature low cycle fatigue and thermomechanical fatigue behavior of Al-Cu cast alloys.
b. Compare the behavior between low cycle fatigue and thermomechanical fatigue.
c. Establish an accurate lifetime prediction model.

1.4 Originality statement

This project comprehensively investigates the influence of Mg and TEs on the elevated-temperature strength, creep, LCF, and OP-TMF behavior. The following topics address specific aspects within this thesis that are characterized by either gap in existing literature or the absence of systematic investigations.

In the first part, the influence of microalloying with Mg (0–0.36 wt.%) on the elevated-temperature strength and creep resistance of Al-Cu 224 cast alloys was investigated. Within this study, two distinct stress regimes were observed, corresponding to disparate creep mechanisms: low-stress regime (associated with dislocation climbing) and high-stress regime (linked to Orowan looping). Notably, the introduction of Mg microalloying yielded enhancements in the creep resistance of Al-Cu alloys, with the alloy containing 0.36 wt.% Mg demonstrating the most optimal creep resistance.

In the second part, eight Al-Cu 224 alloys with different combinations of Zr, Ti, and V additions were designed, including the base alloy, three alloys with individual additions, three alloys with binary combinations, and one alloy with the ternary combination. The effect of these eight distinct combinations on elevated-temperature mechanical and creep properties was systematically investigated. In terms of comprehensive properties, the combined addition of TiZrV alloy exhibited the best elevated-temperature performance.

In the third part, the effects of Mg addition on the cyclic deformation and fatigue life behaviors of Al-Cu 224 cast alloys were investigated under isothermal low cycle

fatigue (LCF) at 300 ℃ and out-of-phase thermo-mechanical fatigue (OP-TMF) in the temperature range 60–300 ℃. A comprehensive analysis was conducted, encompassing microstructural transformations, fracture characteristics, and the underlying damage mechanisms inherent to both LCF and OP-TMF. Additionally, the hysteresis energy model was applicable for predicting the LCF and TMF lifetimes of Al-Cu alloys with relatively high accuracy.

1.5 Thesis outlines

The current Ph.D. thesis consists of five parts.

Chapter 1 introduces the background of this project, encompassing the application of aluminum alloys, creep, and fatigue damages. It also outlines the identified challenges, objectives, and presents the originality statement of this thesis.

Chapter 2 presents the study "Effect of Mg microalloying on elevated-temperature creep resistance of Al-Cu 224 cast alloys", published in Materials Science and Engineering: A (2022, doi.org/10.1016/j.msea.2022.143649). This paper focuses on the effect of microalloying with Mg (0–0.36 wt.%) on the elevated-temperature strength and creep resistance of Al-Cu 224 cast alloys. A wide range of applied stress was designed to investigate the elevated-temperature creep behavior of different Mg-containing alloys, and the creep mechanisms were also comprehensively revealed based on the stress exponent and the TEM images.

Chapter 3 highlights the investigation "Effects of individual and combined additions of transition elements (Zr, Ti and V) on the microstructure stability and elevated-temperature properties of Al-Cu 224 cast alloys", published in Materials Science and Engineering: A (2023, doi.org/10.1016/j.msea.2023.144718). The effects of individual and combined additions of transition elements (TEs) Zr, Ti, and V on the microstructure evolution and elevated-temperature mechanical and creep properties of Al-Cu 224 cast alloys were investigated in this paper. Additionally, the comparison of the overall performance at elevated temperature for different TEs-containing alloys was performed.

Chapter 4 shows the research "Effect of Mg on elevated-temperature low cycle fatigue and thermo-mechanical fatigue behaviors of Al-Cu cast alloys", published in Materials Science and Engineering: A (2023, doi.org/10.1016/j.msea.2023.145588). The effects of Mg addition on the cyclic deformation and fatigue life behaviors of Al-Cu 224 cast alloys were investigated under isothermal low cycle fatigue (LCF) at 300 ℃ and out-of-phase thermo-mechanical fatigue (OP-TMF) in the temperature range 60–300 ℃. Additionally, a comparison between LCF and OP-TMF behavior of Al-Cu alloys was conducted. Furthermore, a hysteresis energy model was applied to predict the LCF and TMF lifetimes.

In Chapter 5, the general conclusions and recommendations for the future work were drawn. Subsequent to the primary chapters, a list of publications is provided. Additionally, Appendix I was also attached, offering the supplementary data pertaining to Chapter 2.

References

[1] K. Hoag, B. Dondlinger, K. Hoag and B. Dondlinger, 2016. Cylinder block and head materials and manufacturing. Vehicular engine design, pp.97-115.

[2] S. Roy, L. F. Allard, A. Rodriguez, T. R. Watkins & A. Shyam, Comparative evaluation of cast aluminum alloys for automotive cylinder heads: part I—microstructure evolution, Metall. Mater. Trans. A 48.5 (2017): 2529-2542. https://doi.org/10.1007/s11661-017-3985-1

[3] M. Javidani & D. Larouche, Application of cast Al–Si alloys in internal combustion engine components, Int. Mater. Rev. 59.3 (2014): 132-158. https://doi.org/10.1179/1743280413Y.0000000027

[4] European Aluminium Association, The aluminium automotive manual, Join. Dissim. Mater. (2015): 1-31.

[5] M. Wang, J. C. Pang, S. X. Li & Z. F. Zhang, Low-cycle fatigue properties and life prediction of Al-Si piston alloy at elevated temperature, Mater. Sci. Eng. A 704 (2017): 480-492. https://doi.org/10.1016/j.msea.2017.08.014

[6] F.J. Feikus, Optimization of Al-Si cast alloys for cylinder head applications, American Foundrymen's Society, Inc, Trans. Am. Foundrym. Soc., 106 (1998): 225-231.

[7] W. Kasprzak, D. Emadi, M. Sahoo, M. and M. Aniolek, Development of aluminium alloys for high temperature applications in diesel engines, Mater. Sci. Forum. 618 (2009): 595-600. https://doi.org/10.4028/www.scientific.net/MSF.618-619.595

[8] J. Rakhmonov, K. Liu, L. Pan, F. Breton & X. G. Chen, Enhanced mechanical properties of high-temperature-resistant Al–Cu cast alloy by microalloying with Mg, J. Alloys Compd. 827 (2020): 154305. https://doi.org/10.1016/j.jallcom.2020.154305

[9] L. Cui, Z. Zhang & X. G. Chen, Development of lightweight Al-based entropy alloys for elevated temperature applications, J. Alloys Compd. 938 (2023): 168619. https://doi.org/10.1016/j.jallcom.2022.168619

[10] D. Li, K. Liu, J. Rakhmonov & X. G. Chen, Enhanced thermal stability of precipitates and elevated-temperature properties via microalloying with transition metals (Zr, V and Sc) in Al–Cu 224 cast alloys, Mater. Sci. Eng. A 827 (2021): 142090. https://doi.org/10.1016/j.msea.2021.142090

[11] M. Pekguleryuz & M. Celikin, Creep resistance in magnesium alloys, Int. Mater. Rev. 55.4 (2010): 197-217. https://doi.org/10.1179/095066010X12646898728327

[12] K. R. Athul, U. T. S. Pillai, A. Srinivasan, B.C. Pai, A review of different creep mechanisms in Mg alloys based on stress exponent and activation

energy, Adv. Eng. Mater. 18 (2016) 770-794. https://doi.org/10.1002/adem.201500393

[13] C. B. Fuller, D. N. Seidman, D. C. Dunand, Acta Mater. 51 (2003) 4803-4814.

[14] L. Jin, K. Liu, X. G. Chen, Evolution of dispersoids and their effects on elevated-temperature strength and creep resistance in Al-Si-Cu 319 cast alloys with Mn and Mo additions, Mater. Sci. Eng. A 770 (2020) 138554. https://doi.org/10.1016/j.msea.2019.138554

[15] D. Yao, W. Zhao, H. Zhao, F. Qiu, Q. Jiang, High creep resistance behavior of the casting Al–Cu alloy modified by La, Scripta Mater. 61 (2009) 1153-1155. https://doi.org/10.1016/j.scriptamat.2009.09.007

[16] M. E. Kassner, Fundamentals of creep in metals and alloys, Butterworth-Heinemann, 2015.

[17] T. G. Langdon, Mater. Sci. Eng. A 283.1-2 (2000): 266-273.

[18] S. Mondol, S. Kashyap, S. Kumar, K. Chattopadhyay, Improvement of high temperature strength of 2219 alloy by Sc and Zr addition through a novel three-stage heat treatment route, Mater. Sci. Eng. A 732 (2018) 157-166. https://doi.org/10.1016/j.msea.2018.07.003

[19] B. Rouxel, M. Ramajayam, T. J. Langan, J. Lamb, P.G. Sanders, T. Dorin, Effect of dislocations, Al3 (Sc, Zr) distribution and ageing temperature on θ′ precipitation in Al-Cu-(Sc)-(Zr) alloys. Mater. 9 (2020) 100610. https://doi.org/10.1016/j.mtla.2020.100610

[20] A. Shyam, S. Roy, D. Shin, J. D. Poplawsky, L. F. Allard, Y. Yamamoto, J. R. Morris, B. Mazumder, J. C. Idrobo, A. Rodriguez, T. R. Watkins, J. A. Haynes, Elevated temperature microstructural stability in cast AlCuMnZr alloys through solute segregation, Mater. Sci. Eng. A 765 (2019) 138279. https://doi.org/10.1016/j.msea.2019.138279

[21] B. K. Milligan, S. Roy, C. S. Hawkins, L. F. Allard, A. Shyam, Impact of microstructural stability on the creep behavior of cast Al–Cu alloys, Mater. Sci. Eng. A 772 (2020) 138697. https://doi.org/10.1016/j.msea.2019.138697

[22] D. N. Seidman, E. A. Marquis, D. C. Dunand, Precipitation strengthening at ambient and elevated temperatures of heat-treatable Al (Sc) alloys, Acta Mater. 50 (2002) 4021-4035. https://doi.org/10.1016/S1359-6454(02)00201-X

[23] C. B. Fuller, D. N. Seidman, D. C. Dunand, Mechanical properties of Al (Sc, Zr) alloys at ambient and elevated temperatures, Acta Mater. 51 (2003) 4803-4814. https://doi.org/10.1016/S1359-6454(03)00320-3

[24] Y. H. Gao, C. Yang, J. Y. Zhang, L. F. Cao, G. Liu, J. Sun & E. Ma, Stabilizing nanoprecipitates in Al-Cu alloys for creep resistance at 300° C. Mater. Res. Lett., 7 (2019) 18-25. https://doi.org/10.1080/21663831.2018.1546773

[25] J. Schijve, Fatigue of structures and materials. Dordrecht: Springer Netherlands, 2009.

[26] F.C. Campbell, ed. Fatigue and fracture: understanding the basics. ASM International, 2012.

[27] D. Socie and B. Socie, Thermomechanical fatigue made easy, the 6th Engineering society international conference on durability and fatigue. Cambridge. 2007.

[28] T. Takahashi, T. Nagayoshi, M. Kumano and K.Sasaki, Thermal plastic-elastic creep analysis of engine cylinder head, SAE Trans. (2002): 276-284.

[29] M.M. Rahman, A.K. Ariffin, S. Abdullah, R. AB and M.S.M. Sani, Assessment of Multiaxial Fatigue Behaviour of Cylinder Head for a New Free Piston Linear Engine, Proceedings of the int. conference on mechanical engineering (ICME2007) Dhaka, Bangladesh. 2007.

[30] S. Trampert, T. Gocmez and S. Pischinger, Thermomechanical fatigue life prediction of cylinder heads in combustion engines, (2008): 012806. https://doi.org/10.1115/1.2771251

[31] D.A. Gerard and D.A. Koss, Porosity and crack initiation during low cycle fatigue, Mater. Sci. Eng. A 129.1 (1990): 77-85. https://doi.org/10.1016/0921-5093(90)90346-5

[32] M. J. Couper, A. E. Neeson and J. R. Griffiths, Casting defects and the fatigue behaviour of an aluminium casting alloy, Fatigue Fract. Eng. Mater. Struct. 13.3 (1990): 213-227. https://doi.org/10.1111/j.1460-2695.1990.tb00594.x

[33] Q. G. Wang, D. Apelian and D. A. Lados, Fatigue behavior of A356-T6 aluminum cast alloys. Part I. Effect of casting defects, J. Light Met. 1.1 (2001): 73-84. https://doi.org/10.1016/S1471-5317(00)00008-0

[34] H. Sehitoglu, T. J. Smith and H. J. Maier. Thermo-mechanical deformation of Al319-T7B with small secondary dendrite arm spacing, Thermo-mechanical Fatigue Behavior of Materials: Third Volume. ASTM International, 2000. https://doi.org/10.1520/STP15253S

[35] Q. G. Wang, D. Apelian and D. A. Lados, Fatigue behavior of A356/357 aluminum cast alloys. Part II–Effect of microstructural constituents, J. Light Met. 1.1 (2001): 85-97. https://doi.org/10.1016/S1471-5317(00)00009-2

[36] S.J. Barnes and K. Lades, The evolution of aluminium based piston alloys for direct injection diesel engines, No. 2002-01-0493. SAE Tech. Paper., 2002. https://doi.org/10.4271/2002-01-0493

[37] A.J. Moffat, Micromechanistic analysis of fatigue in aluminium silicon casting alloys, Diss. University of Southampton, 2007.

[38] T.O. Mbuya, Y. Gu, R.C. Thomson and P.A. Reed, Effect of intermetallic particles and grain boundaries on short fatigue crack growth behaviour in a cast Al–4Cu–3Ni–0.7 Si piston alloy, Fatigue Fract. Eng. Mater. Struct. 40.9 (2017): 1428-1442. https://doi.org/10.1111/ffe.12586

[39] A.J. Moffat, B.G. Mellor, C.L. Chen, R.C. Thomson and P.A.S. Reed, Microstructural analysis of fatigue initiation in Al-Si casting alloys, Materials science forum. Vol. 519. Trans Tech Publications Ltd, 2006. https://doi.org/10.4028/www.scientific.net/MSF.519-521.1083

[40] T.O. Mbuya, I. Sinclair, A.J. Moffat and P.A. Reed, Analysis of fatigue crack initiation and S–N response of model cast aluminium piston alloys, Mater. Sci. Eng. A 528.24 (2011): 7331-7340. https://doi.org/10.1016/j.msea.2011.06.007

[41] C.L. Chen, A. Richter and R.C. Thomson, Mechanical properties of intermetallic phases in multi-component Al–Si alloys using nanoindentation, Intermetallics. 17.8 (2009): 634-641. https://doi.org/10.1016/j.intermet.2009.02.003

[42] Y.X. Gao, J.Z. Yi, P.D. Lee and T.C. Lindley, A micro-cell model of the effect of microstructure and defects on fatigue resistance in cast aluminum alloys, Acta materialia 52.19 (2004): 5435-5449. https://doi.org/10.1016/j.actamat.2004.07.035

[43] K. Shiozawa, Y. Tohda and S.M. Sun, Crack initiation and small fatigue crack growth behaviour of squeeze-cast Al-Si aluminium alloys, Fatigue Fract. Eng. Mater. Struct. 20.2 (1997): 237-247. https://doi.org/10.1111/j.1460-2695.1997.tb00281.x

[44] A. Plumtree and S. Schafer, Initiation and short crack behaviour in aluminium alloy castings, Mechanical Engineering Publications, The Behaviour of Short Fatigue Cracks, (1986): 215-227.

[45] J.Z. Yi, Y.X. Gao, P.D. Lee and T.C. Lindley, Microstructure-based fatigue life prediction for cast A356-T6 aluminum-silicon alloys, Metall. Mater. Trans. B 37 (2006): 301-311. https://doi.org/10.1007/BF02693159

[46] M.R. Joyce, C.M. Styles and P.A.S. Reed, Elevated temperature short crack fatigue behaviour in near eutectic Al–Si alloys, Int. J. Fatigue. 25.9-11 (2003): 863-869. https://doi.org/10.1016/S0142-1123(03)00157-9

[47] J.Z. Yi, Y.X. Gao, P.D. Lee and T.C. Lindley, Effect of Fe-content on fatigue crack initiation and propagation in a cast aluminum–silicon alloy (A356–T6), Mater. Sci. Eng. A 386.1-2 (2004): 396-407. https://doi.org/10.1016/j.msea.2004.07.044

[48] M. J. Caton, J. Wayne Jones, J. M. Boileau and J. E. Allison, The effect of solidification rate on the growth of small fatigue cracks in a cast 319-type aluminum alloy, Metall. Mater. Trans. A 30 (1999): 3055-3068. https://doi.org/10.1007/s11661-999-0216-4

[49] Q. Zhang, Z. Zuo and J. Liu, Stepped-isothermal fatigue analysis of engine piston, Fatigue Fract. Eng. Mater. Struct. 4 (2014): 417-426. https://doi.org/10.1111/ffe.12125

[50] C. M. Styles and P. A. S. Reed, Fatigue of an Al-Si gravity die casting alloy, Materials science forum. Vol. 331. Trans Tech Publications Ltd, 2000. https://doi.org/10.4028/www.scientific.net/MSF.331-337.1457

[51] Gall, Yang, Horstemeyer, McDowell and Fan, The influence of modified intermetallics and Si particles on fatigue crack paths in a cast A356 Al alloy, Fatigue Fract. Eng. Mater. Struct. 23.2 (2000): 159-172. https://doi.org/10.1046/j.1460-2695.2000.00239.x

[52] H.Y. Kim, S.W. Han and H.M. Lee, The influence of Mn and Cr on the tensile properties of A356–0.20 Fe alloy, Mater. Lett. 60.15 (2006): 1880-1883. https://doi.org/10.1016/j.matlet.2005.12.042

[53] H.Y. Kim, T.Y. Park, S.W. Han and H.M. Lee, Effects of Mn on the crystal structure of α-Al (Mn, Fe) Si particles in A356 alloys, J. Cryst. Growth. 291.1 (2006): 207-211. https://doi.org/10.1016/j.jcrysgro.2006.02.006

[54] S. Hegde and K.N. Prabhu, Modification of eutectic silicon in Al–Si alloys, J. Mater. Sci. 43 (2008): 3009-3027. https://doi.org/10.1007/s10853-008-2505-5

[55] S. Kumai, A. Sekikawa, J.Q. Hu, Y. Higo and S. Nunomura, Effects of roughness-induced crack closure on fatigue crack growth in AC4CH cast aluminium alloys, Int. J. Fatigue. 2.19 (1997): 184.

[56] A. Shyam, Y. Yamamoto, D. Shin, S. Roy, J.A. Haynes, P.J. Maziasz, A. Sabau, A.F. Rodriguez-Jasso, J.A. Gonzalez-Villarreal, J. Talamantes-Silva, L. Zhang, C.R. Glaspie, S. Mirmiran, Aluminum alloy compositions and methods of making and using the same. 2017, US Patent App. 15/160,926.

[57] J. D. Poplawsky, B.K. Milligan, L.F. Allard, D. Shin, P. Shower, M.F. Chisholm, A. Shyam, The synergistic role of Mn and Zr/Ti in producing θ′/L12 co-precipitates in Al-Cu alloys, Acta Mater. 194 (2020) 577-586. https://doi.org/10.1016/j.actamat.2020.05.043

[58] S. Mondol, S.K. Makineni, S. Kumar and K. Chattopadhyay, Enhancement of high temperature strength of 2219 alloys through small additions of Nb and Zr and a novel heat treatment, Metall. Mater. Trans. A 49 (2018): 3047-3057. https://doi.org/10.1007/s11661-018-4614-3

[59] D. Shin, A. Shyam, S. Lee, Y. Yamamoto, J.A. Haynes, Solute segregation at the Al/θ′-Al_2Cu interface in Al-Cu alloys, Acta Mater. 141 (2017) 327-340. https://doi.org/10.1016/j.actamat.2017.09.020

[60] Y. H. Gao, L.F. Cao, C. Yang, J.Y. Zhang, G. Liu, J. Sun, Co-stabilization of θ′-Al_2Cu and Al_3Sc precipitates in Sc-microalloyed Al–Cu alloy with enhanced creep resistance, Mater. Today Nano 6 (2019): 100035. https://doi.org/10.1016/j.mtnano.2019.100035

[61] Y.H. Gao, L.F. Cao, J. Kuang, J.Y. Zhang, G. Liu, J. Sun, Assembling dual precipitates to improve high-temperature resistance of multi-microalloyed Al–Cu alloys, J. Alloys Compd. 822 (2020): 153629. https://doi.org/10.1016/j.jallcom.2019.153629

[62] B.A. Chen, G. Liu, R.H. Wang, J.Y. Zhang, L. Jiang, J.J. Song, J. Sun, Effect of interfacial solute segregation on ductile fracture of Al–Cu–Sc alloys, Acta mater. 61.5 (2013) 1676-1690. https://doi.org/10.1016/j.actamat.2012.11.043

[63] C. Yang, P. Zhang, D. Shao, R.H. Wang, L.F. Cao, J.Y. Zhang, G. Liu, B.A. Chen, J. Sun, The influence of Sc solute partitioning on the microalloying effect and mechanical properties of Al-Cu alloys with minor Sc addition, Acta Mater. 119 (2016) 68-79. https://doi.org/10.1016/j.actamat.2016.08.013

[64] J.C.M. Li, Microstructure and properties of materials. World Scientific, 2 (1996) 1-13.

[65] R. Srinivasan, and M.A. Imam, Role of dispersoids on the fatigue behavior of aluminum alloys: a review, Fatigue of Materials III Advances and Emergences in Understanding: Proceedings of the Third Biennial Symposium. Hoboken, NJ, USA: John Wiley & Sons, Inc. (2014) 11-22. http://doi.org/10.1002/9781119041498

[66] P. Li, H. Li, X. Liang, L. Huang, K. Zhang & Z. Chen, Enhanced low-cycle fatigue and crack propagation resistance of an Al-Cu-Mg-Si forging alloy by non-isothermal aging, Mater. Sci. Eng. A 732 (2018): 341-349. https://doi.org/10.1016/j.msea.2018.07.002

Chapter 2

Effect of Mg microalloying on elevated-temperature creep resistance of Al-Cu 224 cast alloys

(Published in the journal of Materials Science and Engineering: A

doi.org/10.1016/j.msea.2022.143649)

Abstract

The influence of microalloying with Mg (0–0.36 wt.%) on the elevated-temperature strength and creep resistance of Al-Cu 224 cast alloys was investigated. The Mg-containing alloys yielded finer and denser θ′ precipitates after high-temperature stabilization (300 ℃/100 h) than the Mg-free alloy, which improved the yield strength at both room temperature and 300 ℃. Compressive creep tests were conducted at 300 ℃ over a wide range of the applied stresses (45–100 MPa). The results showed that the creep resistance increased with increasing Mg content at any fixed applied stress, and the alloy with 0.36 wt.% Mg exhibited the best creep resistance among the four alloys studied. During creep deformation, the θ′ precipitates continued to coarsen. However, Mg microalloying greatly stabilized the θ′ precipitates in the matrix by slowing down the coarsening process. An obvious break was observed in the creep rate curves with different stress exponents (n). Below the break in the low-stress regime (LSR), stress exponent (n) was ~ 3, whereas it increased to 9-12 above the break in the high-stress regime (HSR). In the LSR, the creep was controlled by the dislocation climbing, and it transformed into the Orowan looping in the HSR.

Keywords: Al-Cu alloy; Mg addition; Elevated-temperature mechanical properties; Creep resistance; Creep mechanism.

2.1 Introduction

Along with elevated-temperature strength, creep resistance is one of the most important considerations in the safety design of automotive engine components, which are projected to service at 300–350 ℃, for enhancing the engine efficiency and fulfilling the emission standard requirements [1, 2]. Al-Cu cast alloys are widely used in the automotive and aircraft industries because they exhibit the highest mechanical strength among the various Al cast alloys [3]. However, the creep resistance of Al-Cu cast alloys decreases significantly because of the rapid coarsening of the main strengthening θ′ phase at >250 ℃ [4-6]. Hence, it is necessary to improve the creep resistance for critical applications at high temperatures.

Several approaches have been proposed to improve the creep resistance of aluminum alloys at high temperatures, such as (i) stabilizing the precipitates to avoid coarsening at high temperatures in precipitation-hardening alloys, (ii) introducing thermally stable dispersoids in the matrix, and (iii) introducing secondary phases at the grain boundary to impede grain boundary sliding [6, 7].

Increasing the high-temperature stability of precipitates has been proven to be an effective method for improving creep resistance [6, 8-13]. Several studies have reported that the addition of Sc and Zr to Al-Cu alloys promotes the formation of fine and densely distributed θ″ and θ′ precipitates and suppresses the coarsening of these precipitates at high temperatures [8, 9]. In addition, the formation of nano-sized Al_3(Sc, Zr) dispersoids, which are thermally stable at 300–350 ℃, can pin the dislocations and show excellent elevated-temperature creep resistance [10-12]. Other studies reported

that the addition of Mn and Zr can prevent the transformation of the main strengthening θ′ phase to the equilibrium θ phase up to 350 °C by segregating Mn and Zr at the precipitate interfaces, enhancing the creep resistance [13, 14]. Yao et al. [6] reported that La-added Al-Cu cast alloys exhibited good thermal stability and creep resistance owing to the formation of the $Al_{11}La_3$ phase, which inhibited grain boundary migration and dislocation movement during creep deformation. Recently, Rakhmonov et al. [2] investigated the effect of Mg microalloying on the elevated-temperature mechanical properties of Al-Cu 224 cast alloys. The results showed that the addition of Mg could significantly promote the precipitation of θ′ strengthening phase and hence improve the elevated-temperature mechanical properties, which are expected to have the benefit on the creep resistance of Al-Cu alloys.

To study the creep behavior of metals, creep tests with a constant load and a fixed temperature in tensile or compression creep are often conducted, and the creep strain is plotted as a function of time. A typical creep curve exhibits three creep stages: the primary creep stage, the secondary creep stage, which is often referred to as the steady-state creep, and the tertiary creep stage [7, 15]. The minimum creep rate in the steady-state stage is often used to characterize creep properties. The relationship between the minimum creep rate (ε) and applied stress (σ) is described by the classical power-law equation [5, 6, 16]:

$$\varepsilon = A\sigma^n \exp\left(\frac{-Q}{RT}\right) \quad (2.1)$$

where A is the material constant, n is the stress exponent, Q is the apparent activation energy, T is the absolute temperature (K), and R is the ideal gas constant. The value of

stress exponent *n* is closely related to the creep mechanism, as revealed in previous studies [17-19]. However, precipitation-hardening alloys have exhibited significantly different creep behaviors. Some reports have shown that precipitation-hardened alloys display higher stress sensitivity of creep rate than pure metals [20-22]. Moreover, a pronounced break has been observed in the creep curves of some precipitation-hardened alloys [20, 21, 23-26]. The different slopes below and above the break indicated different creep mechanisms, which was confirmed in well-known high-temperature γ-hardened Ni-based alloys [20, 21]. These features were also observed in Al-Mn alloys [23], Cu-Co alloys [24], Sn-Ag/Cu solders [25] and Al-Fe, V, Si alloys [26]. Surprisingly, few studies have focused on the creep behavior over a range of applied stresses in the precipitation-strengthened Al-Cu alloys [14, 27-29].

In our previous works [2, 30], we found that microalloying with Mg could promote the precipitation of θ′ and enhance the elevated-temperature mechanical properties in Al-Cu 224 alloys. However, above a certain Mg level (0.19 wt.% in [2] and 0.24 wt.% in [30]), the elevated-temperature strength declined with increasing Mg level. In the present work, we extended the Mg levels (0 to 0.36 wt.%) to study the effect of Mg microalloying on the creep resistance of Al-Cu 224 alloys over a wide range of applied stress (45–100 MPa), in order to better assess the potential of those Al-Cu alloys for elevated temperature applications. The microstructures before and after creep deformation were examined using scanning and transmission electron microscopies. Different creep mechanisms were explored in relation to the stress exponents and microstructure evolution.

2.2 Experimental procedures

Four Al-Cu 224 alloys with varying Mg contents, 0–0.36 wt.%, were prepared. The alloys were melted in an electric resistance furnace and degassed with pure Argon for 10 min, and then grain-refined with an Al-5Ti-1B master alloy. The molten metal was cast into a permanent wedge mold. The pouring temperature was 720 ℃ and the preheating temperature of the wedge mold was 250 ℃. Chemical compositions of the alloys analyzed using optical emission spectroscopy are listed in Table 2.1. A rectangular sample cut from the bottom of the wedge casting was used in the investigations. T7 heat treatment was first applied to all cast samples; it included the following steps: 1) a two-step solution treatment conducted first at 495 °C for 2 h and then at 528 °C for 10 h, followed by water quenching; 2) artificial aging at 200 °C for 4 h. To study the elevated-temperature strength and creep behavior, all T7-treated samples were further exposed at 300 °C for 100 h to stabilize the microstructure, which was designated as T7A treatment.

Table 2.1 Chemical composition of 224 cast alloys (wt.%).

Alloy	Cu	Mn	Mg	Si	Fe	Ti	V	Zr	Al
0Mg	4.68	0.34	**0.01**	0.04	0.11	0.17	0.21	0.14	Bal.
0.12Mg	4.69	0.34	**0.12**	0.04	0.11	0.17	0.21	0.15	Bal.
0.24Mg	4.71	0.36	**0.24**	0.04	0.08	0.15	0.18	0.14	Bal.
0.36Mg	4.86	0.35	**0.36**	0.05	0.12	0.17	0.21	0.14	Bal.

The compressive tests at room temperature and 300 ℃ were conducted using a Gleeble 3800 thermo-mechanical simulator unit with a fixed strain rate of 10^{-3} s^{-1} to obtain the stress-strain curves. The 0.2% offset yield strengths of the experimental alloys were determined from the corresponded stress-train curves. Cylindrical specimens (diameter = 10 mm, height = 15 mm) were machined for compressive testing. At least three samples were tested for each condition, and their averages were calculated. Compressive creep tests were performed on the T7A-treated samples at 300 °C using the same cylindrical sample size used in the compressive yield strength tests. Seven different stresses were applied in the creep tests for each alloy, varying from 45 to 100 MPa. At least three tests were conducted for each creep condition and the average value was used.

The microstructures of all experimental alloys were characterized using optical microscopy (OM), scanning electron microscopy (SEM), and transmission electron microscopy (TEM). To reveal the grain structure, the polished samples were etched using Keller's reagent. At least 500 grains were quantified using ImageJ software for each alloy to obtain the average grain size. To observe the microstructural evolution during creep deformation, the samples were quenched at different stages and etched with Keller's reagent for SEM observation. The samples before and after the creep test were prepared for TEM observation to study precipitate evolution. The creep TEM samples were cut perpendicular to the compressive axis at the center. All TEM samples were ground to approximately 40–60 μm and then subjected to a twin-jet electrochemical process at -20 ℃ with a voltage of 20 V in a solution comprising 200 mL methanol and 75 mL nitric acid. TEM was performed at 200 kV to characterize

the precipitates, including the selected area diffraction pattern (SADP). TEM foil thickness was measured using the two-beam convergent beam diffraction pattern (CBED) [31]. Quantification of the θ′-Al_2Cu precipitates, such as the number density and volume fraction, was conducted on several TEM images using a previously described method [32, 33]. At least 1000 precipitates were quantified for each alloy and condition to obtain the average values.

2.3 Results

2.3.1 Microstructure

Fig. 2.1 shows the typical as-cast and T7A-treated microstructures of the 0.12Mg alloy. The as-cast grain structure comprised fine equiaxed grains, and the average grain size of all the experimental alloys was ~40 μm, irrespective of the different Mg contents (Fig. 2.1a). After T7A treatment (Fig. 2.1b), all the experimental alloys displayed a similar microstructure, comprising α-Al grains, Al_3(Ti, Zr, V), and Al_7Cu_2(Fe, Mn) intermetallic. The backscatter SEM image indicates that the platelet Fe-rich phase, Al_7Cu_2(Fe, Mn) (bright phase indicated by the red arrows), was mainly located at the grain boundaries, while the roundish Al_3(Ti, Zr, V) (dark phase indicated by the red arrows) was randomly distributed in the matrix.

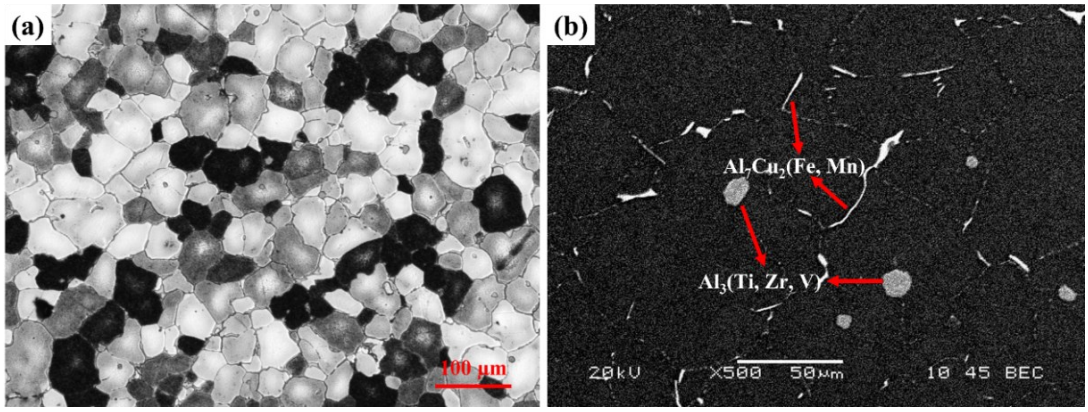

Fig. 2.1 Typical microstructure of 0.12Mg alloy: (a) OM image showing the as-cast grain structure and (b) backscatter SEM image showing two intermetallic phases after T7A.

The bright-field TEM images observed along the $<001>_{\alpha\text{-Al}}$ of the experimental alloys after T7A treatment are shown in Fig. 2.2. The microstructure of the Al-Cu 224 alloys after T7 aging generally comprised a mixture of fine θ″ and θ′ strengthening phases [2, 30, 34]. After stabilization at 300 °C for 100 h (T7A), the precipitate microstructure was predominantly θ′ in all the investigated alloys, which was confirmed by the characteristic spots and streaks of θ′, shown by the white arrows in the SADP (Fig. 2.2f) [8]. However, their characteristics varied with Mg content; the θ′ plates in the Mg-containing alloys (Fig. 2.2b-d) were finer and denser than those in the Mg-free alloy (Fig. 2.2a), which is further confirmed by the quantitative results listed in Table 2.2. For example, the thickness and length decreased from 14.7 nm and 286.2 nm in the 0Mg alloy to 8.9 nm and 82.7 nm in the 0.36Mg alloy, respectively. Meanwhile, the number density of θ′ significantly increased from 8.4×10^{-8} to 9.8×10^{-7} nm^{-3}.

It is also observed that with increasing Mg content, another phase (cubic σ-$Al_5Cu_6Mg_2$) started to precipitate in the Al matrix, confirmed by TEM-EDS results. Up to 0.24%Mg, there was only a trace amount of cubic σ-$Al_5Cu_6Mg_2$ detectable.

However, with 0.36% Mg addition, the number of cubic σ-$Al_5Cu_6Mg_2$ particles significantly increased (Fig. 2.2e). The formation of σ-$Al_5Cu_6Mg_2$ would consume the Cu solutes in the Al matrix leading to the decrease of volume fraction of θ′ in 0.36Mg alloy.

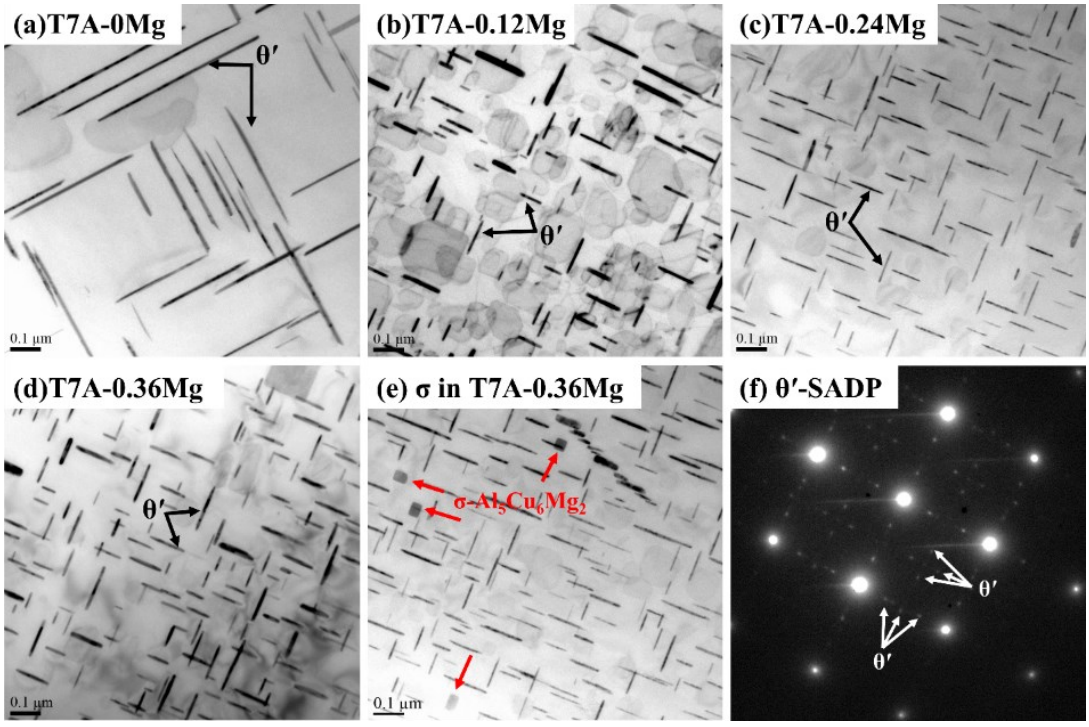

Fig. 2.2 Bright-field TEM images of experimental alloys after T7A: (a) 0Mg, (b) 0.12Mg, (c) 0.24Mg, (d) 0.36 Mg alloy and (e) showing σ-$Al_5Cu_6Mg_2$ in 0.36Mg alloy, and (f) displaying the typical SADP of θ′ in (a-d) viewed along $<001>_{\alpha\text{-Al}}$.

Table 2.2 Summary of quantitative TEM results of θ′ phase after T7A treatment.

Alloy	Quantified particles	Length (nm)	Thickness (nm)	Number density (nm^{-3})	Volume fraction (%)
0Mg	θ′	286.2±149.0	14.7±4.8	8.4×10-8	6.1
0.12Mg		159.6±96.5	12.4±5.6	2.7×10-7	5.2
0.24Mg		97.6±34.5	9.2±2.8	7.1×10-7	4.7
0.36Mg		82.7±33.5	8.9±3.4	9.8×10-7	4.1

2.3.2 Mechanical properties

Compressive yield strengths of the alloys at room temperature and 300 °C after T7A treatment are shown in Fig. 2.3. The yield strength at room temperature increased from 197 MPa in the Mg-free (0Mg) alloy to 212 MPa in the 0.12Mg alloy and further to 256 MPa in the 0.24Mg alloy, and then, it decreased to 219 MPa in the 0.36Mg alloy. A similar trend was found for the yield strength at 300 °C, where it increased from 122 MPa in the Mg-free alloy to 142 MPa in the 0.24Mg alloy, and then decreased to 134 MPa in the 0.36Mg alloy. The decrease of the yield strength in the 0.36Mg alloy at both room temperature and 300 °C could be attributed to the precipitation and the increased number of cubic σ-$Al_5Cu_6Mg_2$ particles, which consumed the Cu solutes in the Al matrix leading to the decrease of volume fraction of θ′ precipitates. Clearly, the Mg addition generally improves the yield strength at room temperature as well as at 300 °C after T7A treatment, and the alloy with 0.24% Mg showed the best mechanical strength.

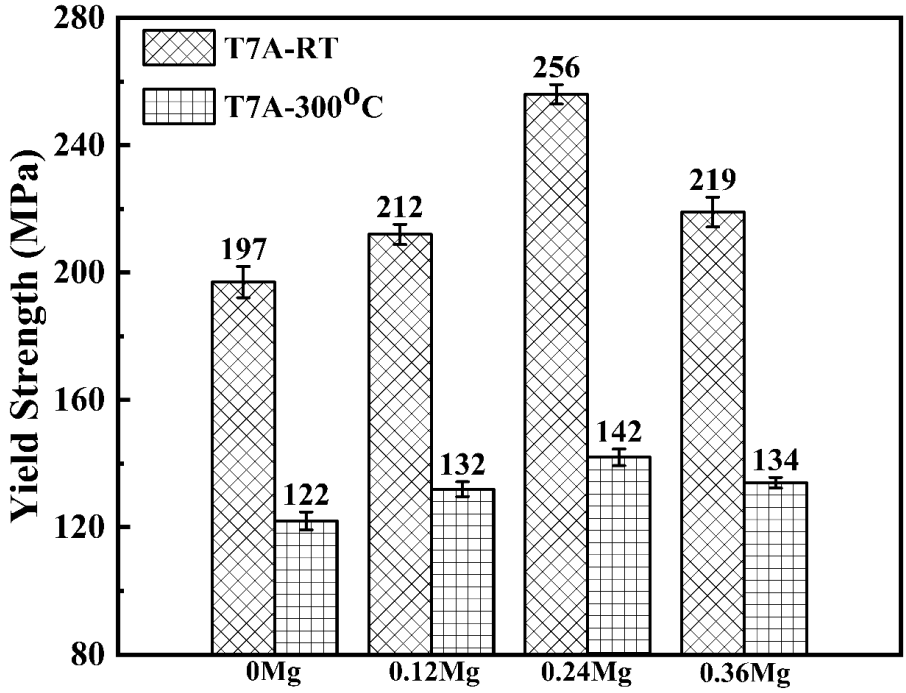

Fig. 2.3 Compressive yield strength of 224 experimental alloys at room temperature and 300 ℃ after T7A heat treatment.

2.3.3 Creep behavior

Fig. 2.4 shows the typical compressive creep curves of the experimental alloys examined at 300 °C for up to 100 h at 65 MPa and 95 MPa. At low applied stresses (for example, 65 MPa), the creep curves displayed two typical stages: primary stage and secondary (quasi-steady) stage. Due to work hardening, the creep rate in the primary stage continued to decrease (Fig. 2.4a and c). With further deformation, the creep rate finally reached the lowest level and barely changed with increasing time (Fig. 2.4c) due to the balance between work hardening and thermal softening. The constant creep rate in the quasi-steady stage is often referred to as the minimum creep rate. The minimum creep rates in this study are the average values measured from the quasi-steady stage. At high applied stresses (for example, 95 MPa), a tertiary stage appeared followed by the quasi-steady stage (Fig. 2.4b and d), in which the creep strain

increased sharply (Fig. 2.4b) and the creep rate increased gradually. The creep deformation in the tertiary stage becomes unstable, accompanied by microstructure failure (breakdown of the intermetallic components and grains and occurrences of cracking), which will be discussed later in detail. This creep behavior was also observed in another study [35].

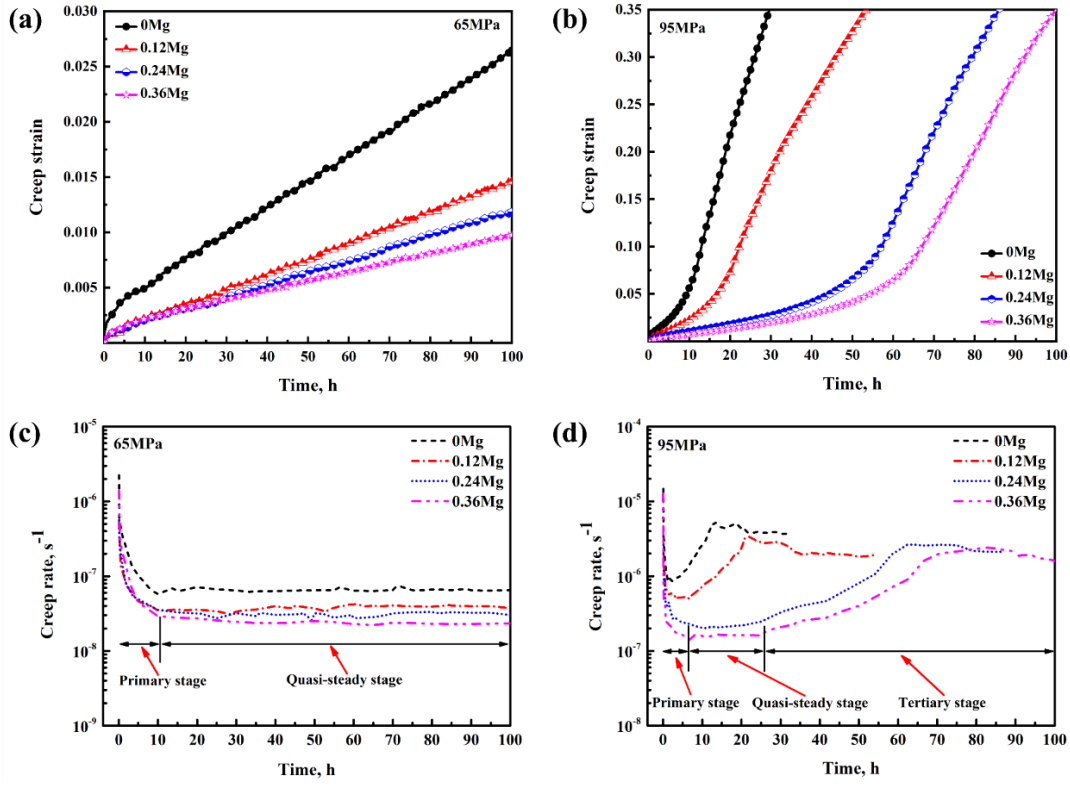

Fig. 2.4 Typical creep curves of experimental alloys at (a) 65 MPa and (b) 95 MPa, and the creep rate curves at (c) 65 MPa and (d) 95 MPa. The schematic indication of the creep stages in Fig. 2.4d is based on 0.24Mg and 0.36Mg creep rate curves.

The minimum creep rates as a function of the applied stress are logarithmically displayed in Fig. 2.5. For all four alloys tested, two regimes were observed based on the slope of the creep rate vs. applied stress curves (for example, low-stress regime (LSR) = 45–75 MPa, high-stress regime (HSR) = 90–100 MPa), and they were separated by the break of the overall curves. In Fig. 2.5, a linear fit of the double-logarithmic plot was applied to each regime to calculate the stress exponents

corresponding to the two regimes. For all the alloys, the slope of the creep rate curves changed sharply from the LSR to the HSR. An obvious break in the creep rate curves was also observed for various precipitation-hardened alloys [20, 21, 23-26]. In the LSR, n = ~3 for all the experimental alloys, whereas it changed considerably to >9 after an applied stress of 75 MPa in the HSR. With increasing Mg content, the minimum creep rates decreased in the LSR as well as HSR, indicating enhanced creep resistance due to Mg addition. The 0.36Mg alloy exhibited the lowest minimum creep rate, and hence, the best creep resistance at 300 °C.

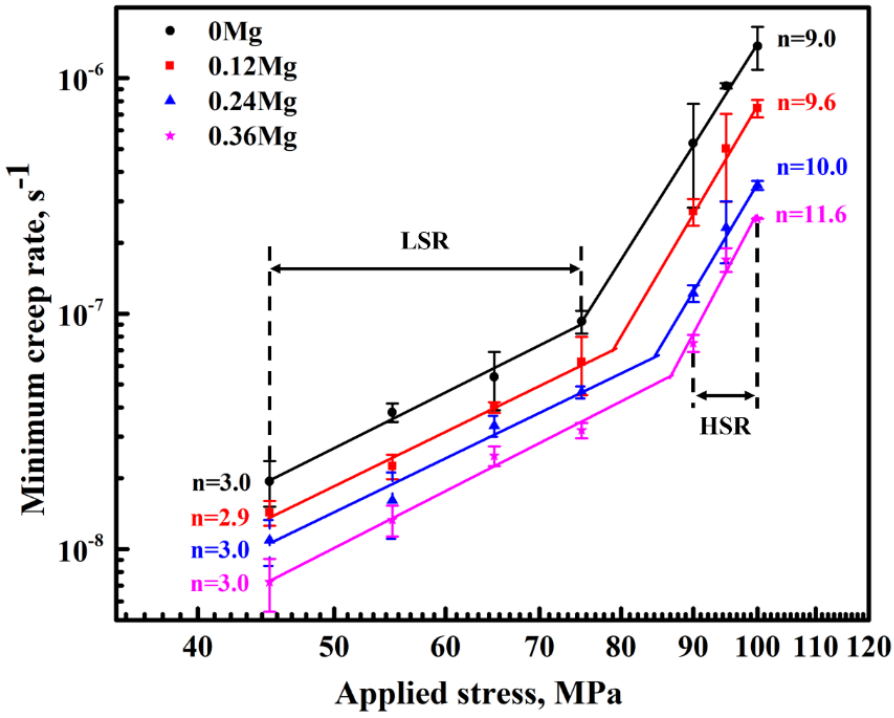

Fig. 2.5 Minimum creep rate as a function of applied stress (logarithmic scale) for different Mg-containing alloys at 300 °C.

The total strain after 100 h of creep and the time to failure were also used to characterize the creep properties of the LSR and HSR, respectively (Fig. 2.6). In the LSR, the total strain increased with increasing applied stress; however, the total strain decreased remarkably with increasing Mg level (Fig. 2.6a) at a given stress. For

instance, the average total strain decreased from 0.022 for the 0Mg alloy to 0.008 for the 0.36Mg alloy at 65 MPa applied stress. In the HSR, the time to failure is the creep duration before the tertiary creep. During creep at high applied stresses, the 0Mg alloy quickly entered the tertiary creep (in <10 h), indicating poor creep resistance. In contrast, the time to failure of the Mg-containing alloys was much longer (Fig. 2.6b). The results of the total strain and the time to failure also confirmed that the creep resistance improved with increasing Mg content, and the 0.36Mg alloy exhibited the best creep resistance among the four alloys studied.

It is worthwhile to mention that for aluminum alloys in elevated temperature applications, the elevated-temperature strength and creep resistance are two important design aspects to be considered. Although the 0.36Mg alloy showed the highest creep resistance, the 0.24Mg alloy exhibited the best mechanical strength and second highest creep resistance among the four alloys studied. Based on the two aspects above, the 0.24Mg alloy is considered to be the optimum one for the overall performance at elevated temperatures.

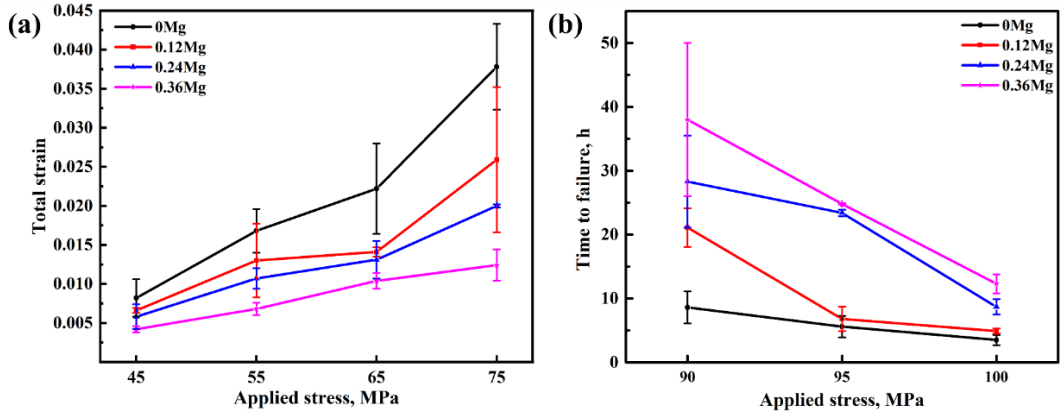

Fig. 2.6 (a)Total strain after 100 h and (b) the time to failure as function of the applied stress in experimental alloys.

As observed in Fig. 2.4(b) and 4(d), there was a distinct change in the creep rate in the tertiary stage of creep, where it initially increased sharply and then slowed down to an approximately stable value, as schematically shown in Fig. 2.7(a). To reveal the different failure modes in the tertiary stage of creep, the creep samples were interrupted at different phases of the tertiary stage and quenched with water, and the quenched microstructures were observed. For the 0Mg alloy, at the beginning of the tertiary stage, several broken intermetallics on the grain boundaries and a few cracks in the grain interiors were observed, as indicated by the white arrows in Fig. 2.7(b). Thus, the sliding of the broken grains under high applied stress caused a sharp increase in the creep rate, and their failure modes were believed to be the sliding of the broken grains. As the creep deformation continued to the middle of the tertiary stage (Fig. 2.7(c)), small crush bands were formed by the severe breakage of intermetallics and grains. Further creep deformation caused the crush bands and the broken grains to merge (Fig. 2.7(d)), slowing the creep rate and becoming relatively stable. After the sliding of the broken grains, the failure mode was the merging of the crush bands and the broken grains.

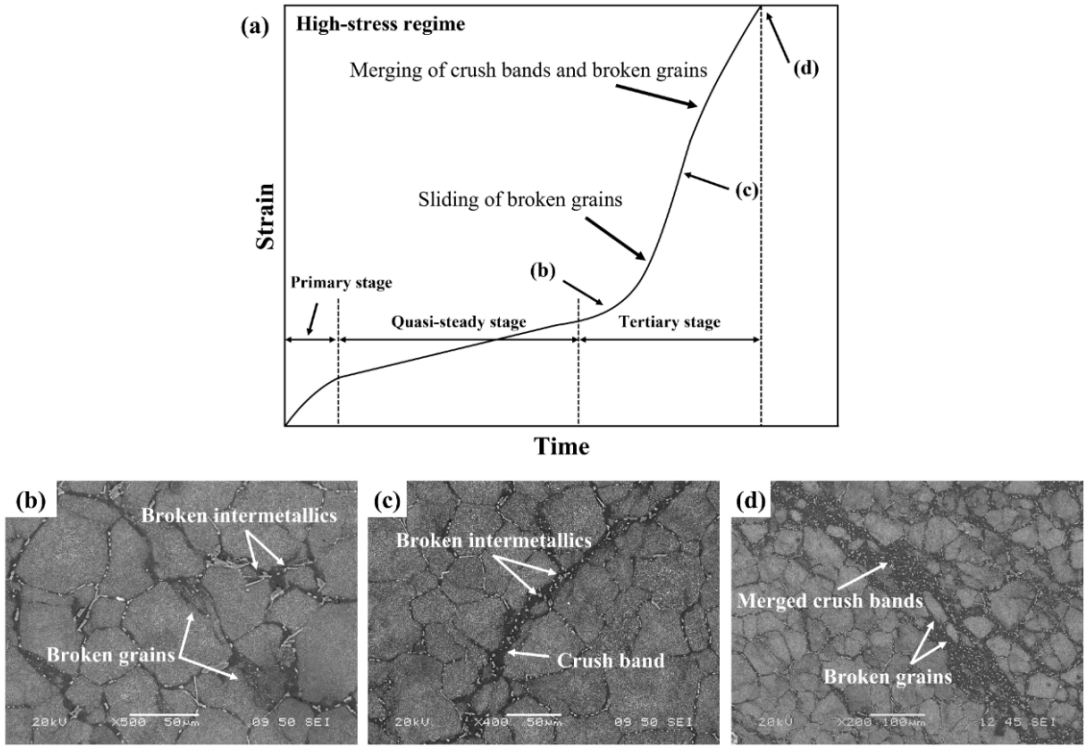

Fig. 2.7 (a)Schematic compressive creep stages in the high-stress regime and the failure modes in the third stage of creep. The microstructures of crept 0Mg alloy quenched at (b) beginning of the third stage, (c) middle of the third stage and (d) end of the creep test.

The microstructural evolution in the tertiary stage of the HSR indicates the existence of severe plastic deformation during creep. Unlike the LSR in the elastic deformation zone, the HSR was in the elastic-plastic deformation zone before reaching the engineering yield stress, as illustrated by the compressive stress-strain curves in Fig. 2.8. During creep in the HSR, plastic deformation was activated to some extent. It took much longer for the Mg-containing alloys to reach the tertiary stage (Fig. 2.4(d) and 6(b)), and these alloys suffered less plastic deformation compared to the base alloy. The grain boundary structures revealed that large and sparse particles occurred on the grain boundaries of the 0Mg alloy (Fig. 2.9(a)), while there were smaller and denser particles covering almost the entire grain boundaries in the Mg-containing alloys (0.24Mg alloy, Fig. 2.9(b)). These particles were identified as the equilibrium θ-Al_2Cu

phase according to the SEM-EDS results (Al-69.7 at%, Cu-30.3 at%) and their morphologies. The addition of Mg possibly promoted the formation of θ-Al_2Cu particles on the grain boundaries and inhibited coarsening during T7A treatment, although the mechanism is not yet well understood. The uniformly distributed θ-Al_2Cu particles and their high coverage on the grain boundaries enhance the stability of the grain structure and inhibit grain boundary migration during plastic deformation [14].

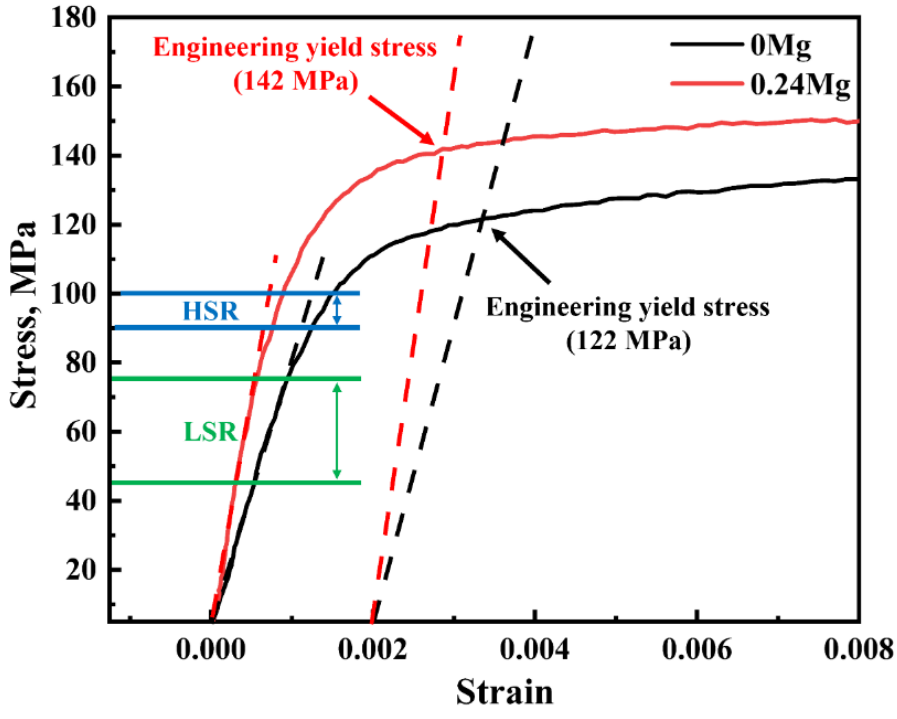

Fig. 2.8 Compressive stress-strain curves of 0Mg and 0.24Mg alloys tested at 300 ℃.

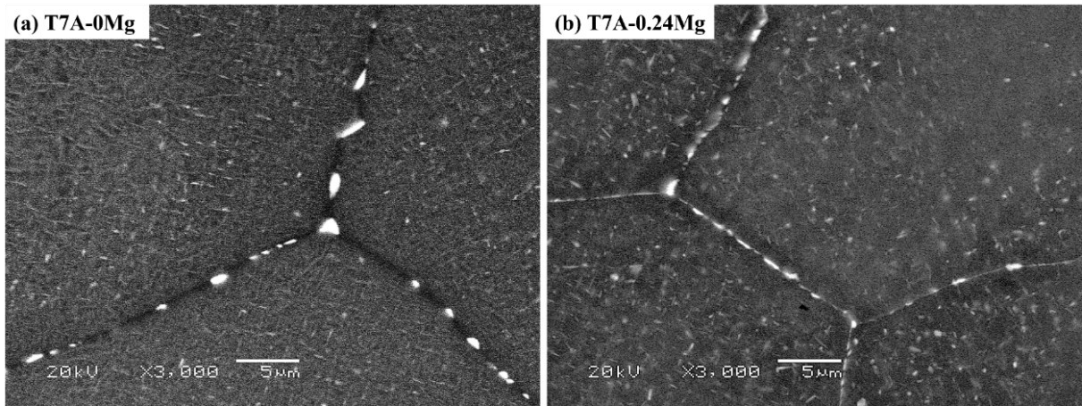

Fig. 2.9 Backscattered electron image of the grain boundary structure covered by θ-Al_2Cu particles: (a) 0Mg alloy and (b) 0.24Mg alloy after T7A condition. Note the higher coverage of the grain boundaries by particles in 0.24Mg than 0Mg alloy.

2.3.4 Precipitate evolution after creep deformation

The precipitate evolution after creep deformation was examined by TEM, and typical bright-field TEM images along $<001>_{\alpha\text{-Al}}$ are shown in Fig. 2.10. Here, the applied stresses of 65 MPa and 90 MPa were selected to represent the precipitates in the LSR and HSR, respectively. The selected diffraction patterns (not shown here) confirmed that the dominant precipitate after the creep test in both the LSR and HSR was still θ′ for all the experimental alloys. A few equilibrium θ particles were also observed after the creep process. The quantitative results are presented in Table 2.3. Compared with the θ′ plates before creep (Fig. 2.2 and Table 2.2), the θ′ precipitates after creep became longer and thicker. Take 0Mg alloy as example, the length and thickness after creep at 65 MPa increased 13.2% and 12.9%, respectively. High external stress increased the size of the θ′ precipitates. For example, when the applied stress increased from 65 to 90 MPa, the length and thickness of the θ′ plates increased from 324 and 17 nm to 359 and 20 nm, representing an increase of 10.8 % and 19.3%, respectively, in the 0Mg alloy. However, for the Mg-containing alloys, the length and thickness of θ′ increased to a lesser extent. In addition, the number density of θ′ in all

the experimental alloys decreased when the stress increased from 65 to 90 MPa. Again, the Mg-containing alloys showed a much higher number density of θ′ than the Mg-free base alloy, which was one order of magnitude higher. The TEM results indicated that the Mg-containing alloys have a better coarsening resistance of θ′ precipitates during creep deformation relative to the Mg-free alloy.

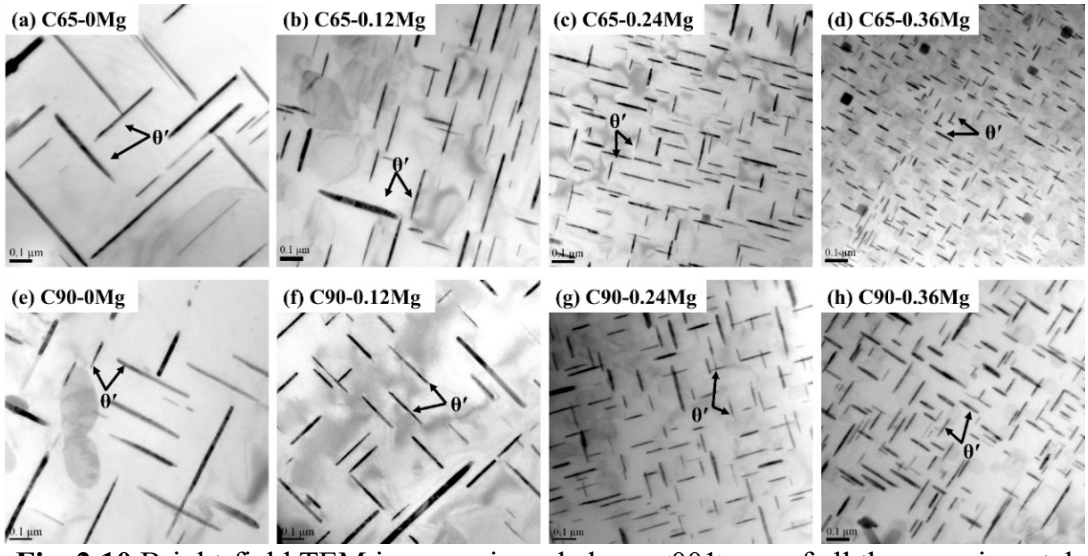

Fig. 2.10 Bright-field TEM images viewed along $<001>_{\alpha\text{-Al}}$ of all the experimental alloys after creep for 100 h at the applied stress of 65 MPa (C65) and 90 MPa (C90).

Table 2.3 Summary of quantitative TEM results of θ′ precipitates after creep.

Alloy	Quantified particles	Condition (Applied stress)	Length (nm)	Thickness (nm)	Number density (nm^{-3})	Volume fraction (%)
0Mg	θ′	C65	324.1±139.4	16.6±6.6	4.0×10^{-8}	7.6
		C90	359.1±180.9	19.8±7.9	3.5×10^{-8}	8.9
0.12Mg		C65	221.0±89.3	15.8±5.4	1.2×10^{-7}	6.4
		C90	234.0±81.0	16.6±6.4	1.0×10^{-7}	7.3
0.24Mg		C65	101.5±37.8	9.9±3.5	4.2×10^{-7}	4.9
		C90	120.0±53.1	12.7±4.6	3.7×10^{-7}	5.2
0.36Mg		C65	89.2±46.7	9.7±4.0	6.8×10^{-7}	4.0
		C90	96.4±38.9	11.4±3.2	5.9×10^{-7}	5.0

2.4 Discussion

2.4.1 Effect of Mg on the coarsening of θ′ precipitates during thermal exposure and creep process

In our previous study [2, 30], it is observed that after the T7 aging treatment, the main precipitates in the 0Mg alloy were θ″, whereas a mixed microstructure of θ′ and θ″ as strengthening phases was found in the Mg-containing alloys. After stabilizing at 300 °C for 100 h (T7A treatment) in the present study, all precipitation microstructures of the four alloys transformed to θ′ precipitates as the predominant strengthening phase, accompanied by coarsening during stabilization (Fig. 2.2). The θ″ plates in the 0Mg alloy dissolved quickly and formed fewer and thicker θ′ particles, whereas the Mg-containing alloys mainly experienced lateral growth at the expense of small θ″

precipitates during the high-temperature stabilization at 300 °C. Clearly, Mg microalloying increased the coarsening resistance of the θ′ precipitates, resulting in a finer size and a higher number density of the θ′ precipitates than in the 0Mg alloy after T7A treatment (Table 2.2). With increasing Mg content, the θ′ precipitates became finer and denser in the matrix.

During creep deformation, under external stress and high temperature, the θ′ precipitates continued to coarsen in all the Mg-free and Mg-containing alloys; however, the dominant precipitates were still θ′ particles after the creep process (Fig. 2.10), which generally provided a reasonable creep resistance in the LSR (Fig. 2.4a). The high applied stress resulted in severe coarsening of θ′ precipitates as a high number density of dislocations would be generated during creep deformation that promoted the element diffusion and hence the coarsening of precipitates. This accelerated the creep progress in the HSR (Fig. 2.4b). The TEM results (Fig. 2.10) revealed that the Mg-containing alloys exhibited a higher coarsening resistance of θ′, even under external stress during creep exposure, than the Mg-free alloy. Fig. 2.11 shows a comparison of the precipitate characteristics before and after creep for the 0Mg and 0.24Mg alloys. The 0Mg alloy exhibited coarse precipitates prior to creep, and the precipitates became much coarser after creep, whereas the 0.24Mg alloy had fine precipitates before creep and the coarsening during creep increased to a much lesser extent. This indicates that Mg microalloying greatly stabilized the θ′ precipitates in the matrix by slowing down the coarsening process of the precipitates during either thermal exposure (T7A) or high-temperature creep deformation, which provided improved creep resistance in the Mg-containing alloys.

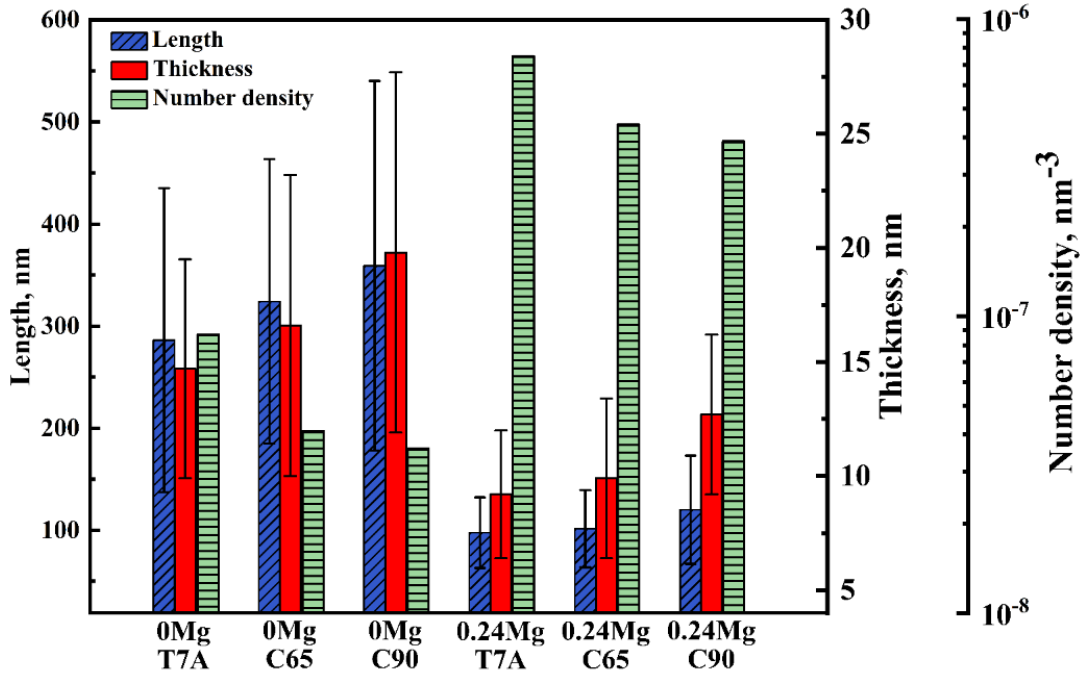

Fig. 2.11 Characteristics of precipitates after creep deformation from T7A-treated 0Mg alloy and 0.24Mg alloy.

2.4.2 Creep mechanism

The precipitation-hardened Al-Cu alloys in this study displayed different creep behaviors than pure aluminum. An obvious break was observed in the creep rate-stress curves (Fig. 2.5), where the *n* was approximately 3 below the break, while it was >9 above the break, which is much greater than the value of 4.4 in pure aluminum [16, 36]. It has been reported that the stress exponent is related to the creep mechanism [17-19]. Unlike pure metals and solid-solution alloys, precipitation-hardened alloys containing the break showed a different relationship between the stress exponent and creep mechanism. When the value of *n* is much higher than 5 (above the break), the dominant creep mechanism is believed to be Friedel cutting (coherent particles) or Orowan bypassing (semi-coherent and incoherent particles) [20, 21, 23, 25]; whereas a value of *n* at 3–4 indicates that dislocations can bypass the precipitates by thermally-

activated climbing [16, 20, 21, 37]. A schematic representation of the interaction between dislocations and the precipitates is shown in Fig. 2.12 [38, 39].

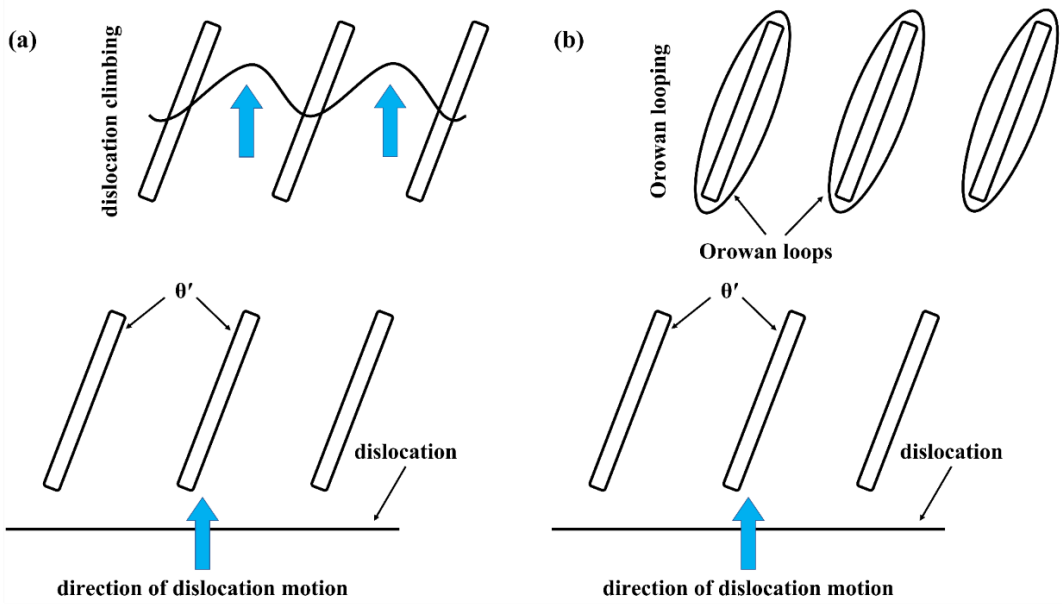

Fig. 2.12 Schematic representation of (a) dislocation climbing [38] and (b) Orowan looping [39].

A chart of the minimum creep rate, $\dot{\varepsilon}^{1/n}$, versus the applied stress is plotted in Fig. 2.13, where the value of n = 3 gives the best linear fit in the LSR for all the experimental alloys. Hence, the creep deformation for all experimental alloys in the LSR was assumed to be controlled by dislocation climbing. Threshold stress was not observed in the LSR for all the experimental alloys when the data were extrapolated to $\dot{\varepsilon}$ = 0 (see Fig. 2.13). Several studies also confirmed that threshold stress was not found in dispersion-hardened Al-Mg alloys [40], Al-Fe, V, Si alloy [26] and γ′-hardened Ni-base alloy [20, 21]. In the HSR, the creep behavior of all the alloys was dominated by Orowan looping. In this case, extrapolating the data to $\dot{\varepsilon}$ = 0 in the HSR can yield the experimental Orowan loop stress, as previously found [20, 23, 25, 26]. An upward trend was observed as the Mg content increased from 0 to 0.36 wt.%: 63

MPa (0Mg), 65 MPa (0.12Mg), 66 MPa (0.24Mg) and 72 MPa (0.36Mg). Meanwhile, the stress for the Orowan loop can be calculated using the following equation [21, 25]:

$$\sigma_{Or} = \frac{0.4Gb}{\pi\lambda} \cdot \frac{ln(d/b)}{(1-\nu)^{\frac{1}{2}}} \tag{2.2}$$

where λ is the interparticle spacing, d is the average particle diameter, b is Burger's vector, ν is Poisson's ratio, and G is the shear modulus. Based on Eq. 2.2, the theoretical Orowan looping stresses were calculated as 66 MPa (0Mg), 67 MPa (0.12Mg), 70 MPa (0.24Mg) and 72 MPa (0.36Mg), which is in good agreement with the experimental data shown in Fig. 2.13.

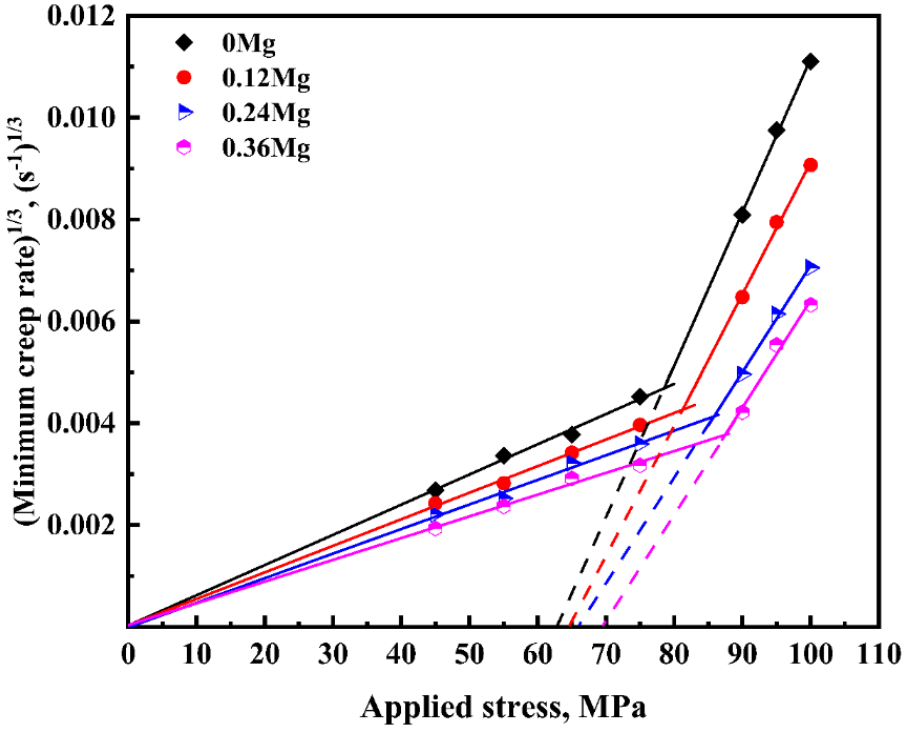

Fig. 2.13 Plot of $\dot{\varepsilon}^{1/n}$ vs applied stress, using a value of 3 for n.

The interactions between the precipitates and dislocations in the quasi-steady stage were observed using TEM. Fig. 2.14(a) and 14(b) show typical weak-beam dark-field TEM images viewed along $<001>_{\alpha\text{-Al}}$ of the 0.24Mg alloy at the quasi-steady

stage under applied stresses of 65 and 95 MPa. In the LSR (65 MPa), some dislocation segments climbed above the precipitates, as indicated by the red arrows in Fig. 2.14(a). Characteristics of Orowan looping, such as closed loops and dislocation pairs [20] were not observed. Hence, it is suggested that the creep mechanism in the LSR is dislocation climbing. In the crept HSR sample (Fig. 2.14(b)), some dislocation loops on the broad face of the θ′ plates were observed, which was also previously confirmed [41]. Fig. 2.14(c) provides another example of 0Mg alloy at the quasi-steady stage under an applied stress of 95 MPa, in which many dislocation loops are left on the θ′ plates. Therefore, it is reasonable to believe that Orowan looping is the dominant creep mechanism in the HSR. The thinner and denser θ′ particles observed in the Mg-containing alloys (Fig. 2.2) exhibited a higher hindering effect on dislocation climbing and Orowan looping during creep deformation than the Mg-free alloy, resulting in a higher creep resistance.

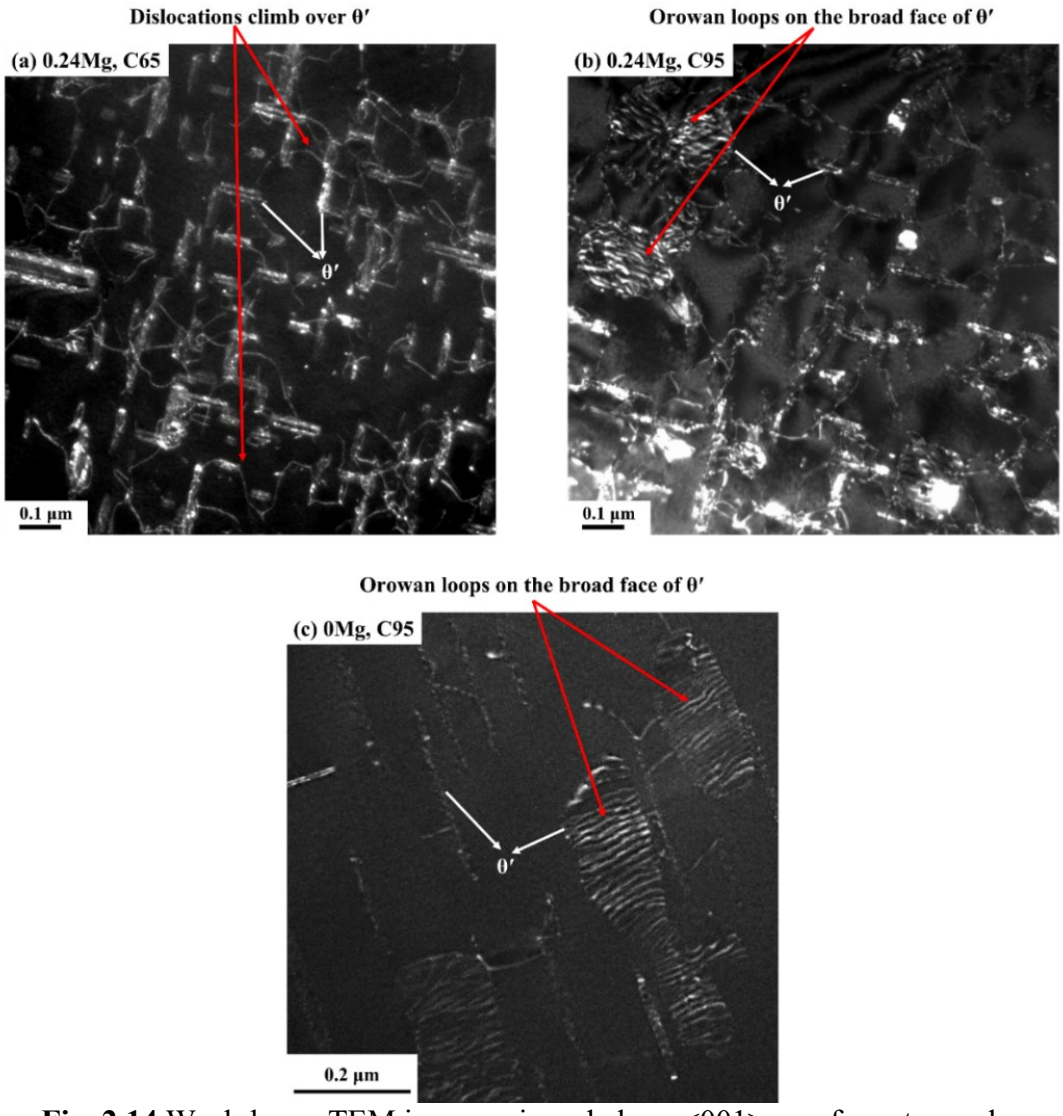

Fig. 2.14 Weak-beam TEM images viewed along <001>$_{\alpha\text{-Al}}$ of crept samples quenched at the steady-state stage, (a) 0.24Mg alloy, 65 MPa (LSR) and (b) 0.24Mg alloy, 95 MPa (HSR) and (c) 0Mg alloy, 95 MPa (HSR).

As mentioned above, when the applied stress was sufficiently high to overcome the Orowan loop stress provided by the semi-coherent θ′ precipitates, Orowan looping dominated the creep deformation in the HSR. In the LSR, the applied stress is insufficient to operate by Orowan looping, and dislocations bypass the precipitates by thermally activated climbing. Interestingly, in the tertiary stage in the HSR, the active creep mechanism of the 224 alloys transferred from micro-scale (Orowan looping) to macro-scale (grain structure collapsing and sliding). In general, the addition of Mg

enhanced the creep resistance of the Al-Cu 224 cast alloys through the stabilization of the θ′ precipitates during thermal exposure and creep owing to the great hindering effect of the dislocation motion in the matrix (dislocation climbing and Orowan looping). Furthermore, the formation of the θ-Al_2Cu particles with high coverage on the grain boundaries in the Mg-containing alloys provided supplementary support for creep resistance by inhibiting grain rotation and grain boundary migration, particularly in the HSR.

2.4.3 Comparison of the creep data of various aluminum alloys

Fig. 2.15 provides the comparison of the minimum creep rates of several alloys in Al-Cu-(Mg) alloy family. All the creep tests were performed at 300 °C. Compared to a conventional Al-Cu 206 alloy [14], the 224 cast alloys exihibted much low creep rates, indicating an excellent thermal stablity and creep resistance. The creep data of two high-Mg-containing Al-Cu-Mg alloys via powder metallurgical route are also included in Fig. 2.15. The Al-4.4Cu-1.47Mg alloy with higher Mg level [27] exhibited a higher creep rate than the Al-3.7Cu-1.3Mg alloy with lower Mg level [28], but both alloys had faster creep rates (lower creep resistance) than 224 alloys studied in the present work. In recent years, several studies have explored the addition of transistion elements (particlurary Zr, Mn, Sc, etc.) to improve the thermal stability of θ′ strengthening phase and hence enhance the elevated-temperature properties in Al-Cu alloys [2, 12-14, 34]. Because our 224 alloys also contained the transistion elements (Zr, V, Ti and Mn, see Table 2.1), the creep rates of the 0Mg alloy were almost the same as those of the newly developed ACMZ (Al-6.1Cu-0.42Mn-0.15Zr) alloy [29]; both alloys were at very levels of the creep rates, which were even lower than the Sc-

containing Al-2.5Cu alloy [12]. However, the present work domostrated that the creep resistance of 224 alloys could be further improved by Mg microalloying. The 0.36Mg alloy exhibted one of the lowest creep rates (namely best creep resistance) among all alloys compared. Only the RR350 (Al-4.8Cu-0.17Zr-1.2Ni-0.26Co) alloy [14] showed the comparable lowest creep rates owing to the high Ni and Co contents in the alloy.

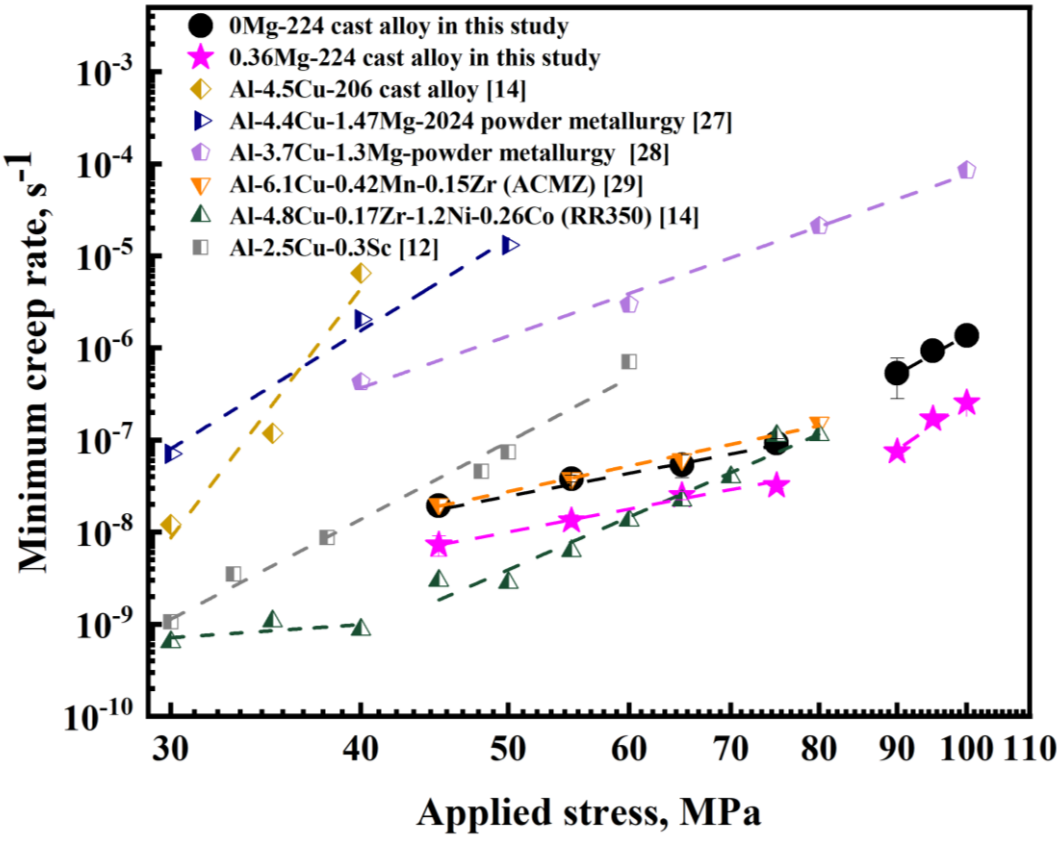

Fig. 2.15 Comparison of the minimum creep rates for various aluminum alloys; all tested at 300 °C.

2.5 Conclusions

1) Microalloying with Mg yielded finer and denser θ′ precipitates after T7A treatment relative to the Mg-free base alloy. The high coarsening resistance of the precipitates in the Mg-containing alloys improves the yield strength at both room temperature and 300 °C.

2) The addition of Mg improved creep resistance. With increasing Mg content, the total creep strain and minimum creep rates decreased, and the time to failure increased. Among the four alloys studied, the alloy with 0.36 wt.% Mg exhibited the best creep resistance.

3) During creep deformation, the θ′ precipitates continued to coarsen in all four alloys. However, Mg microalloying significantly stabilized the θ′ precipitates in the matrix by slowing down the coarsening process of the precipitates, which improved the creep resistance of the alloys.

4) Two regimes were observed in the creep rate curves for all four alloys (that is, the LSR and HSR), and they were separated by a break with different stress exponents. The pronounced breaks revealed different creep mechanisms below and above the breaks: dislocation climbing in the LSR and Orowan looping in the HSR.

References

[1] M. Javidani, D. Larouche, Application of cast Al–Si alloys in internal combustion engine components, Int. Mater. Rev. 59 (2014) 132-158. https://doi.org/10.1179/1743280413Y.0000000027

[2] J. Rakhmonov, K. Liu, L. Pan, F. Breton, X. G. Chen, Enhanced mechanical properties of high-temperature-resistant Al–Cu cast alloy by microalloying with Mg, J. Alloys Compd. 827 (2020) 154305. https://doi.org/10.1016/j.jallcom.2020.154305

[3] P. Ramakrishnan, Automotive applications of powder metallurgy, Adv. Powder. Metall. Woodhead Publishing, (2013) 493-519. https://doi.org/10.1533/9780857098900.4.493

[4] T. Nakajima, M. Takeda, T. Endo, Accelerated coarsening of precipitates in crept Al–Cu alloys, Mater. Sci. Eng. A 387 (2004) 670-673. https://doi.org/10.1016/j.msea.2004.01.131

[5] L. Jin, K. Liu, X. G. Chen, Evolution of dispersoids and their effects on elevated-temperature strength and creep resistance in Al-Si-Cu 319 cast alloys with Mn and Mo

additions, Mater. Sci. Eng. A 770 (2020) 138554. https://doi.org/10.1016/j.msea.2019.138554

[6] D. Yao, W. Zhao, H. Zhao, F. Qiu, Q. Jiang, High creep resistance behavior of the casting Al–Cu alloy modified by La, Scripta Mater. 61 (2009) 1153-1155. https://doi.org/10.1016/j.scriptamat.2009.09.007

[7] K. R. Athul, U. T. S. Pillai, A. Srinivasan, B.C. Pai, A review of different creep mechanisms in Mg alloys based on stress exponent and activation energy, Adv. Eng. Mater. 18 (2016) 770-794.

https://doi.org/10.1002/adem.201500393

[8] S. Mondol, S. Kashyap, S. Kumar, K. Chattopadhyay, Improvement of high temperature strength of 2219 alloy by Sc and Zr addition through a novel three-stage heat treatment route, Mater. Sci. Eng. A 732 (2018) 157-166. https://doi.org/10.1016/j.msea.2018.07.003

[9] B. Rouxel, M. Ramajayam, T. J. Langan, J. Lamb, P.G. Sanders, T. Dorin, Effect of dislocations, Al3 (Sc, Zr) distribution and ageing temperature on θ′ precipitation in Al-Cu-(Sc)-(Zr) alloys. Mater. 9 (2020) 100610. https://doi.org/10.1016/j.mtla.2020.100610

[10] D. N. Seidman, E. A. Marquis, D. C. Dunand, Precipitation strengthening at ambient and elevated temperatures of heat-treatable Al (Sc) alloys, Acta Mater. 50 (2002) 4021-4035. https://doi.org/10.1016/S1359-6454(02)00201-X

[11] C. B. Fuller, D. N. Seidman, D. C. Dunand, Mechanical properties of Al (Sc, Zr) alloys at ambient and elevated temperatures, Acta Mater. 51 (2003) 4803-4814. https://doi.org/10.1016/S1359-6454(03)00320-3

[12] Y. H. Gao, C. Yang, J. Y. Zhang, L. F. Cao, G. Liu, J. Sun & E. Ma, Stabilizing nanoprecipitates in Al-Cu alloys for creep resistance at 300° C. Materials Research Letters, 7 (2019) 18-25. https://doi.org/10.1080/21663831.2018.1546773

[13] A. Shyam, S. Roy, D. Shin, J. D. Poplawsky, L. F. Allard, Y. Yamamoto, J. R. Morris, B. Mazumder, J. C. Idrobo, A. Rodriguez, T. R. Watkins, J. A. Haynes, Elevated temperature microstructural stability in cast AlCuMnZr alloys through solute segregation, Mater. Sci. Eng. A 765 (2019) 138279. https://doi.org/10.1016/j.msea.2019.138279

[14] B. K. Milligan, S. Roy, C. S. Hawkins, L. F. Allard, A. Shyam, Impact of microstructural stability on the creep behavior of cast Al–Cu alloys, Mater. Sci. Eng. A 772 (2020) 138697. https://doi.org/10.1016/j.msea.2019.138697

[15] M. Pekguleryuz, M. Celikin, Creep resistance in magnesium alloys, Int. Mater. Rev. 55 (2010) 197-217. https://doi.org/10.1179/095066010X12646898728327

[16] M. E. Kassner, Fundamentals of creep in metals and alloys, Butterworth-Heinemann, 2015.

[17] Y. Xu, L. Zhan, L. Xu, M. Huang, Experimental research on creep aging behavior of Al-Cu-Mg alloy with tensile and compressive stresses, Mater. Sci. Eng. A 682 (2017) 54-62. https://doi.org/10.1016/j.msea.2016.11.043

[18] C. Yang, L. Cao, Y. Gao, P. Cheng, P. Zhang, J. Kuang, J. Zhang, J. Sun, Nanostructural Sc-based hierarchy to improve the creep resistance of Al–Cu alloys, Mater. Des. 186 (2020) 108309. https://doi.org/10.1016/j.matdes.2019.108309

[19] W. S. Tian, Q. L. Zhao, Q. Q. Zhang, F. Qiu, Q. C. Jiang, Superior creep resistance of 0.3 wt% nano-sized TiCp/Al-Cu composite, Mater. Sci. Eng. A 700 (2017) 42-48. https://doi.org/10.1016/j.msea.2017.05.101

[20] R. Lagneborg, B. Bergman, The stress/creep rate behaviour of precipitation-hardened alloys, Met. Sci. 10 (1976) 20-28. https://doi.org/10.1179/030634576790431462

[21] R. A. Stevens, P. E. J. Flewitt, The dependence of creep rate on microstructure in a γ′ strengthened superalloy, Acta Metall. 29 (1981) 867-882. https://doi.org/10.1016/0001-6160(81)90129-2

[22] J. Rösler, E. Arzt, A new model-based creep equation for dispersion strengthened materials. Acta Metall. Mater. 38 (1990) 671-683. https://doi.org/10.1016/0956-7151(90)90223-4

[23] Y. H. Yeh, H. Nakashima, H. Kurishita, S. Goto, H. Yoshinaga, High-temperature creep and threshold stress of precipitation-hardened Al-0.7 at% Mn alloy, Mater. Trans. JIM 32 (1991) 52-60. https://doi.org/10.2320/matertrans1989.32.52

[24] B. Bergman, Creep deformation of two-phase Cu-Co alloys, Scand. J. Metall. 4 (1975) 177-181.

[25] M. Kerr, N. Chawla, Creep deformation behavior of Sn–3.5 Ag solder/Cu couple at small length scales, Acta Mater. 52 (2004) 4527-4535. https://doi.org/10.1016/j.actamat.2004.06.010

[26] S. Mitra, Elevated temperature deformation behavior of a dispersion-strengthened Al-Fe, V, Si alloy, Metall. Mater. Trans. A 27 (1996) 3913-3923. http://doi.org/10.1007/BF02595640

[27] L. Kloc, S. Spigarelli, E. Cerri, E. Evangelista, T.G. Langdon, Creep behavior of an aluminum 2024 alloy produced by powder metallurgy, Acta Mater. 45 (1997): 529-540. https://doi.org/10.1016/S1359-6454(96)00190-5

[28] L. Wang, F. Qiu, Q. Zhao, M. Zhao & Q. Jiang, Superior high creep resistance of in situ nano-sized TiCx/Al-Cu-Mg composite, Sci. Rep. 7 (2017) 4540. https://doi.org/10.1038/s41598-017-04816-0

[29] S. Bahl, J. Rakhmonov, C. Kenel, D. C. Dunand, A. Shyam, Effect of grain-boundary θ-Al_2Cu precipitates on tensile and compressive creep properties of cast Al–Cu–Mn–Zr alloys, Mater. Sci. Eng. A 840 (2022) 142946. https://doi.org/10.1016/j.msea.2022.142946

[30] P. Hu, K. Liu, L. Pan, F. Breton, X. G. Chen, Evolution of precipitates and mechanical properties in Al-Cu 224 cast alloys with various Mg additions, COM 60th Conference of Metallurgists Proceedings, 00121 (2021) 105-114.

[31] P. M. Kelly, A. Jostsons, R. G. Blake, J. G. Napier, The determination of foil thickness by scanning transmission electron microscopy, Phys. Status. Solidi. A 31 (1975) 771-780. https://doi.org/10.1002/pssa.2210310251

[32] J. F. Nie, B. C. Muddle, Strengthening of an Al–Cu–Sn alloy by deformation-resistant precipitate plates, Acta Mater. 56 (2008) 3490-3501. https://doi.org/10.1016/j.actamat.2008.03.028

[33] S. Roy, L. F. Allard, A. Rodriguez, W. D. Porter, A. Shyam, Comparative evaluation of cast aluminum alloys for automotive cylinder heads: Part II: Mechanical and thermal properties, Metall. Mater. Trans. A Phys. Metall. Mater. Sci. 48 (2017) 2543-2562. http://doi.org/10.1007/s11661-017-3986-0

[34] D. Li, K. Liu, J. Rakhmonov, X. G. Chen, Enhanced thermal stability of precipitates and elevated-temperature properties via microalloying with transition metals (Zr, V and Sc) in Al–Cu 224 cast alloys, Mater. Sci. Eng. A 827 (2021) 142090. https://doi.org/10.1016/j.msea.2021.142090

[35] E. W. Andrews, J. S. Huang, L. J. Gibson, Creep behavior of a closed-cell aluminum foam Acta Mater. 47 (1999) 2927-2935. https://doi.org/10.1016/S1359-6454(99)00161-5

[36] H. J. Frost, M. F. Ashby, Deformation mechanism maps: the plasticity and creep of metals and ceramics, Pergamon press, 1982.

[37] J. Rösler, E. Arzt, The kinetics of dislocation climb over hard particles—I. Climb without attractive particle-dislocation interaction. Acta Metall. 36 (1988) 1043-1051. https://doi.org/10.1016/0001-6160(88)90158-7

[38] S. Mukherjee, M. Nuhi, A. Dasgupta, M. Modarres, Creep constitutive models suitable for solder alloys in electronic assemblies, J. Electron. Packag. 138 (2016) 030801. https://doi.org/10.1115/1.4033375

[39] W. Z. Han, A. Vinogradov, C. R. Hutchinson, On the reversibility of dislocation slip during cyclic deformation of Al alloys containing shear-resistant particles, Acta Mater. 59 (2011) 3720-3736. https://doi.org/10.1016/j.actamat.2011.03.007

[40] W. C. Oliver, W. D. Nix, High temperature deformation of oxide dispersion strengthened al and Al-Mg solid solutions, Acta Metall. 30 (1982) 1335-1347. https://doi.org/10.1016/0001-6160(82)90153-5

[41] J. da Costa Teixeira, L. Bourgeois, C. W. Sinclair, C. R. Hutchinson, The effect of shear-resistant, plate-shaped precipitates on the work hardening of Al alloys: towards a prediction of the strength–elongation correlation, Acta Mater. 57 (2009) 6075-6089. https://doi.org/10.1016/j.actamat.2009.08.034

Chapter 3

Effects of individual and combined additions of transition elements (Zr, Ti and V) on the microstructure stability and elevated-temperature properties of Al-Cu 224 cast alloys

(Published in the journal of Materials Science and Engineering: A

doi.org/10.1016/j.msea.2023.144718)

Abstract

The effects of individual and combined additions of transition elements (TEs) Zr, Ti, and V on the microstructure evolution and elevated-temperature mechanical and creep properties of Al-Cu 224 cast alloys were investigated. All alloys had a mixed precipitate microstructure of θ″- and θ′-Al_2Cu after T7 heat treatment. During the thermal exposure at 300 ℃, θ″ transferred into θ′ as the predominant strengthening phase. The coarsening resistance of θ′ during the thermal exposure and further creep deformation was greatly improved by the addition of TEs. Individually, Zr addition demonstrated the best efficiency in stabilizing θ′, while the combination of Zr + V and Ti + Zr + V achieved the highest efficiency. The addition of TEs generally improved the yield strength (YS) at 300 ℃, and the ZrV and TiZrV alloys achieved the highest YS. A close correlation between the YS and the distribution and thermal stability of θ′ was observed. The creep resistance at elevated temperatures was affected by the thermal stability of θ′ and grain size. Zr-containing alloys (ZrV, Zr, and TiZrV) exhibit superior creep resistance. In terms of comprehensive properties, the combined addition of TiZrV alloy exhibited the best elevated-temperature performance.

Keywords: Al-Cu cast alloys; transition elements; precipitate coarsening; elevated-temperature mechanical properties; creep resistance.

3.1 Introduction

Owing to the increasing scarcity of nonrenewable resources and the need for environmental protection, improving engine efficiency and reducing fuel consumption have attracted widespread attention. Increasing the working temperature and power of the engine components is an effective approach [1]. Al–Cu cast alloys have attracted considerable interest for internal combustion engine applications owing to their light weight and superior mechanical performance [2, 3]. The room-temperature mechanical properties of Al-Cu alloys have been extensively studied. The typical precipitation sequence in Al-Cu alloys is given as follows: supersaturated solid solution (SSS) → GP I zones → GP II zones (θ″) → θ′ → θ [4, 5], where θ′ is found to be the main strengthening phase [6]. However, when the service temperature of engine components is above 200 ℃, the strengthening precipitates undergo coarsening rapidly, resulting in a significant softening of the alloys and causing severe failure during service [7, 8]. The high-temperature resistance of the materials is a crucial factor to take into account in order to fulfill the increasing demands for elevated-temperature applications.

Recent studies have revealed that the high-temperature properties of Al-Cu alloys can be significantly improved by microalloying with slow-diffusing transition elements (TEs) such as Sc, Zr, Ti, V, and Mn [9-18]. It has been reported that the YS of the Al–Cu 206 alloy at 300 °C reached 105 MPa after thermal exposure at 300 °C with the addition of Mn, Zr, and Ni [9]. In our recent works [10, 11], the elevated-temperature mechanical and creep properties at 300 °C of Al–Cu 224 type alloys could be further improved after exposure at 300 °C for 100 h via microalloying with Mg, Zr, V, and Ti. The improved elevated-temperature properties of Al-Cu alloys are primarily

due to the enhancement of the thermal stability of the main strengthening phase of nanoscale θ′-Al_2Cu [9, 10, 12]. Several studies have demonstrated that the thermal stability of θ′ in Al-Cu alloys is promoted by the segregation of solute atoms of TEs at the Al/θ′ interface to inhibit the coarsening of θ′, such as Sc segregation [12-16], Ti segregation [17, 18], Zr segregation [3, 9, 18], V segregation [17], and Mn segregation [3, 9, 18]. Recently, the synergistic stabilizing role of TEs in Al-Cu alloys has drawn much attention. Jonathan et al. [17] reported that the separate addition of Zr/Ti and Mn can improve the stability of Al-Cu alloys at 200 ℃ and 300 ℃, respectively. Furthermore, Shyam et al. [18] demonstrated that the combined addition of Mn and Zr in Al-Cu alloys (termed ACMZ alloys) could further increase their thermal stability up to 350 ℃. They reported that Mn addition could segregate quickly to Al/θ′ interfaces and stabilize θ′ long enough to allow other slower diffusion TEs (e.g., Ti and Zr) to segregate to Al/θ′ interfaces, thereby providing further protection [9, 18, 19]. The enhanced coarsening resistance of θ′ in ACMZ alloy also increases its creep resistance at 300 ℃ [20, 21]. However, the addition of TEs could result in the formation of thermally stable Al_3M dispersoids (M = Sc, Zr, Ti, V, etc.) in the aluminum matrix [13, 14, 22, 23], providing complementary strengthening at elevated temperatures [19, 22, 24]. In addition, these Al_3M dispersoids can provide heterogeneous nucleation sites for θ′ and retard the coarsening of θ′ precipitates [25].

Despite several studies on the high-temperature properties of Al-Cu alloys, there is still a lack of systematic investigation of the impact of individual and combined additions of TEs in the literature. In the present work, we designed eight Al-Cu alloys and focused on the different combinations of the three commonly used TEs in

aluminum alloys (Zr, Ti, and V) to study their role in elevated-temperature mechanical and creep properties. The microstructural stability during current exposure and creep deformation were investigated using transmission electron microscopy. The compressive yield strength tests and creep tests at 300 °C were performed to compare the elevated-temperature properties with the different TEs additions.

3.2 Experimental procedures

Eight Al-Cu 224 alloys with a fixed amount of Mn (0.35 wt. %) but different combinations of Zr, Ti, and V additions were prepared, including the base alloy, three alloys with individual additions, three alloys with binary combinations, and one alloy with the ternary combination. The alloys were melted in a 300-kg electric resistance furnace. After reaching 750 °C, the melt was degassed with pure Ar for 10 min. All alloys were grain-refined with 0.05 wt. % Ti of the Al-5Ti-1B master alloy and cast in a permanent wedge mold preheated at 250 °C. The pouring temperature was 720 °C. The chemical compositions of the alloys analyzed using optical emission spectroscopy are listed in Table 3.1. All tested samples were cut from the same location as the wedge castings, as shown in the shaded part of Fig. 3.1a. All cast samples were initially subjected to the traditional T7 heat treatment (solution treatment at 495 °C/2 h + 528 °C/10 h; aging at 200 °C/4 h), after which an additional thermal exposure at 300 °C for 100 h was carried out to stabilize the microstructure, known as the T7A treatment. The details of the heat treatment procedure are shown in Fig. 3.1b.

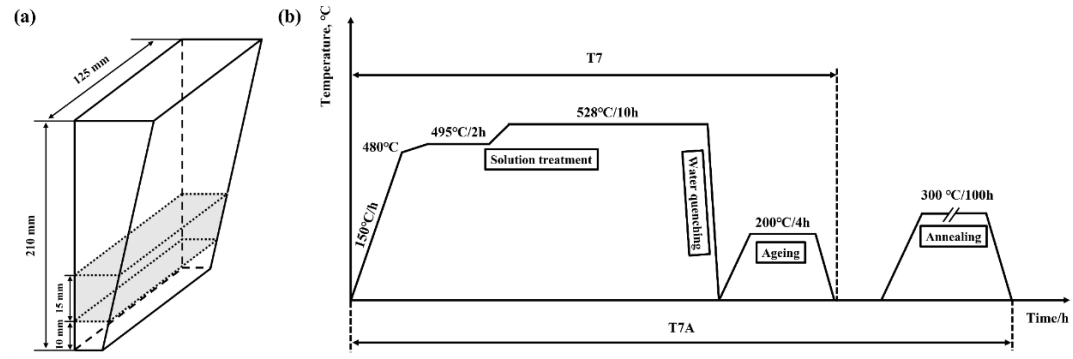

Fig. 3.1 The schematic graph of (a) the wedge casting and the location of sampling and (b) the heat treatment procedure applied in the present work.

Table 3.1 Chemical compositions of experimental alloys (wt. %).

Alloys	Si	Fe	Cu	Mn	Mg	Ti	V	Zr	Al
Base	0.06	0.12	4.70	0.35	0.14	0.05	0.01	0.01	Bal.
Zr	0.06	0.12	4.66	0.35	0.14	0.06	0.01	**0.15**	Bal.
Ti	0.09	0.10	4.62	0.34	0.12	**0.17**	0.01	0.01	Bal.
V	0.08	0.08	4.60	0.34	0.10	0.04	**0.23**	0.01	Bal.
ZrV	0.06	0.12	4.79	0.35	0.13	0.06	**0.17**	**0.15**	Bal.
TiZr	0.09	0.09	4.57	0.34	0.11	**0.18**	0.01	**0.16**	Bal.
TiV	0.08	0.08	4.65	0.34	0.16	**0.16**	**0.23**	0.01	Bal.
TiZrV	0.04	0.11	4.69	0.34	0.12	**0.17**	**0.21**	**0.15**	Bal.

The compressive tests at room temperature and 300 °C were conducted in a Gleeble 3800 thermomechanical simulator unit with a fixed strain rate of 10^{-3} s^{-1}. The 0.2% offset yield strengths were determined from the stress-strain curves. Cylindrical specimens with a diameter of 10 mm and a length of 15 mm were machined for compressive and creep tests. At least three samples were tested for each condition, and their average values were obtained. The compressive creep tests were performed on

the T7A-treated samples at a fixed temperature of 300 ℃ for 100 h. The applied stress varied from 45 to 60 MPa.

The microstructures of all the alloys were observed using optical microscopy (OM) and transmission electron microscopy (TEM). The as-cast grain structure was revealed using Keller's reagent and quantified using ImageJ software, and at least 500 grains were measured to obtain the average grain size. A TEM study was carried out to characterize the precipitates after the T7, T7A, and creep tests. The obtained TEM images were analyzed using the ImageJ software to quantify the parameters of the precipitates (thickness, length, and number density). At least 1000 precipitates were quantified for each alloy and condition. Details of the quantification method can be found in [8, 26, 27].

3.3 Results

3.3.1 As-cast and heat-treated microstructures

Fig. 3.2 shows the as-cast grain structures of the experimental alloys. Equiaxed grains were observed in all alloys, but the grain size varied with the addition of TEs. The measured grain sizes of all the alloys are summarized in Table 3.2. Based on the average grain size, the experimental alloys were divided into three groups: fine-grained (TiZr and TiZrV alloys), medium-grained (Ti, V, and TiV alloys), and coarse-grained (base, Zr, and ZrV alloys). The addition of Ti and V acted as grain growth restrictors and refined the grain structure [28]. As shown in Table 3.2, the grain sizes of all Ti/V-containing alloys were finer than those of the base alloy. For instance, the grain size decreased from 99 μm in the base alloy to approximately 60 μm in the Ti, V, and TiV

alloys. Compared to Ti/V-containing alloys, the addition of Zr, especially the combination of Zr and V, poisoned grain refining [29, 30], leading to a much coarser grain structure in the Zr alloy (124 μm) and ZrV alloy (194 μm). Further additions of Ti to Zr-containing alloys can compensate for the Zr poisoning effect and effectively refine the grain structure. The finest grain structures were observed in TiZr (30 μm) and TiZrV (39 μm) alloys.

Typical microstructures in the as-cast and T7-treated conditions, as an example of three alloys (the base, TiZr, and TiZrV alloys), are shown in Fig. 3.3. In the as-cast condition (Figs. 3.3a–c), all experimental alloys consisted of α-Al dendrite cells/grains, θ-Al_2Cu, and Al_7Cu_2(Fe, Mn) intermetallics distributed along the cell/grain boundaries. In addition, a very small amount of primary Al_3M particles (M = Zr, Ti, and V or their combination) was found in the TEs-containing alloys (Figs. 3.3b and c), and they were distributed randomly in the matrix. After T7 heat treatment, most of the θ-Al_2Cu phase dissolved into the matrix (Figs. 3.3d–f), while Al_7Cu_2(Fe, Mn) and Al_3M barely changed (Figs. 3.3e and f). The thermal exposure at 300 °C for 100 h (T7A) did not affect the intermetallic Al_7Cu_2(Fe, Mn) or Al_3M particles. No obvious difference in the optical microstructure was observed between the T7 and T7A conditions; hence, the microstructure images in the T7A condition are not shown here.

Table 3.2 The average grain sizes of the experimental alloys.

	Fine grain		Medium grain			Coarse grain		
Alloys	TiZr	TiZrV	Ti	TiV	V	Base	Zr	ZrV
Grain size, μm	30±3	39±4	54±9	54±8	66±11	99±22	124±22	194±46

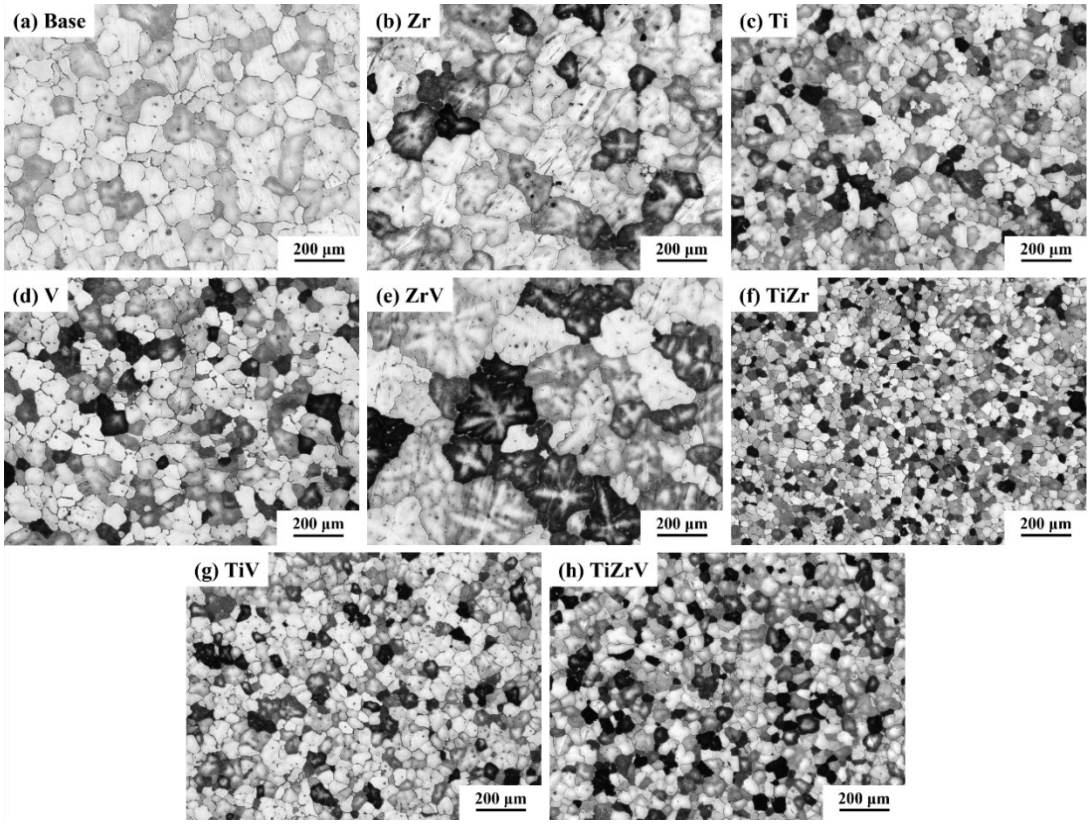

Fig. 3.2 The as-cast grain structures of the experimental alloys.

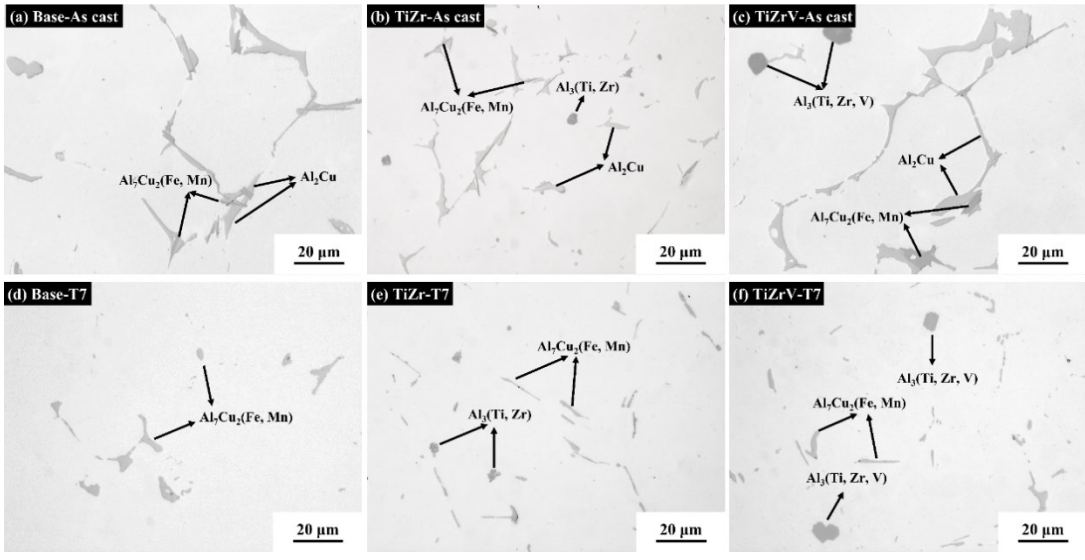

Fig. 3.3 The OM microstructure images of three alloys at as-cast and T7 conditions.

The bright-field TEM images viewed along the $<001>_{\alpha\text{-Al}}$ direction of all the experimental alloys after T7 treatment are shown in Fig. 3.4. Two types of disk-shaped θ″ and θ′ were observed, as confirmed by the selected area diffraction patterns (SADP)

shown in Fig. 3.4(i). The size of θ″ precipitates was much smaller than that of θ′. A mixture of θ″ and θ′ in the aluminum matrix was found in the base alloy and in most Zr-containing alloys, including Zr, ZrV, and TiZrV alloys (Figs. 3.4a, b, e, and h). However, the microstructure was dominated by θ′ precipitates in the Ti/V-containing alloys, namely the V, Ti, TiZr, and TiV alloys (Figs. 3.4c, d, f, and g). A few θ″ precipitates are observed as minor phases. This may be due to the different solute-vacancy binding energies of TEs, which can affect the diffusion of Cu atoms [31-33]. The mechanism needs further exploration. A non-uniform distribution of precipitates is often observed in the second group of alloys. For instance, most θ″ precipitates were found near the grain boundaries, probably owing to the segregation of the TEs and Cu [33, 34], whereas the predominant precipitates turned into θ′ as the distance from the grain boundaries increased (Fig. 3.5).

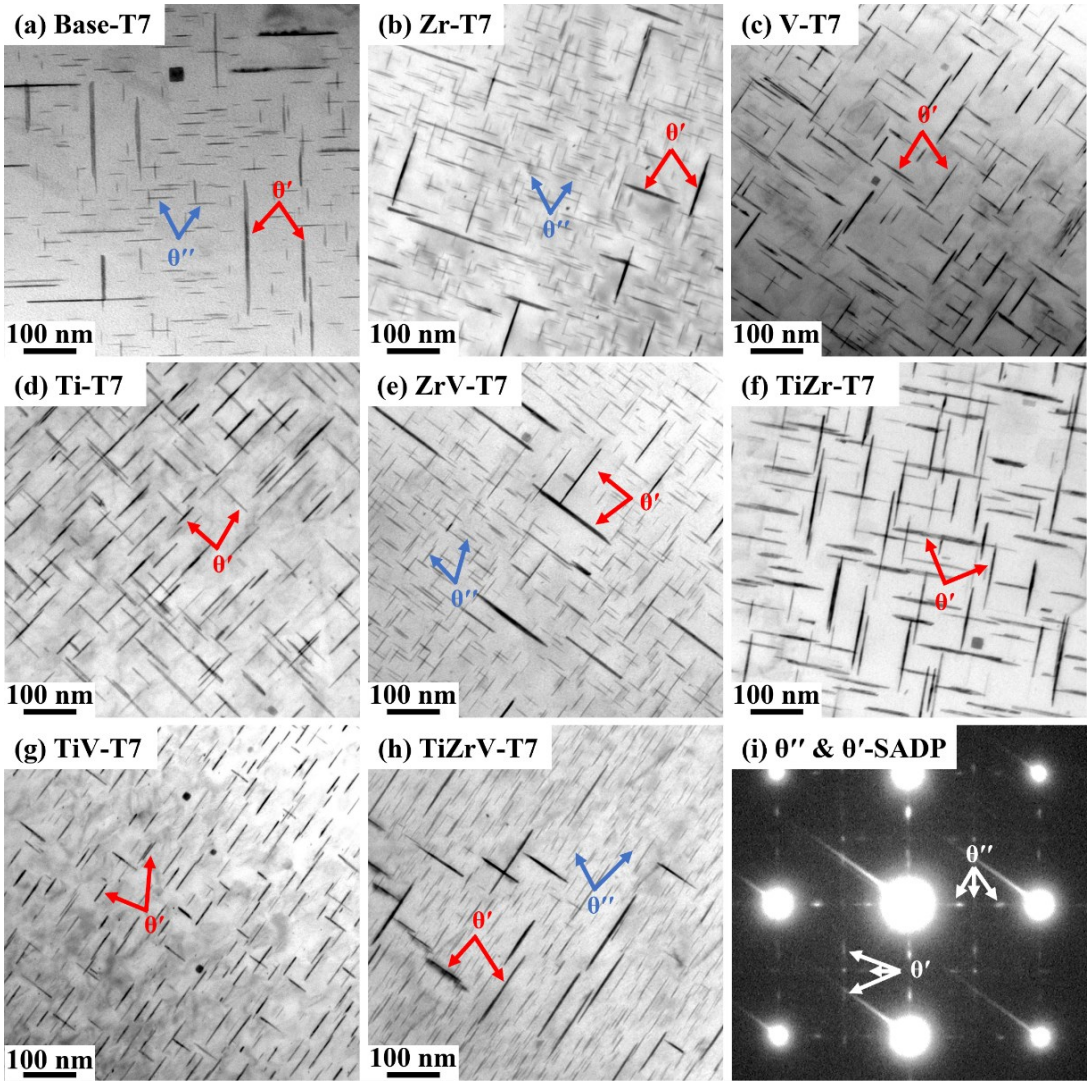

Fig. 3.4 Bright-field TEM images viewed along <001>$_{\alpha\text{-Al}}$ showing the precipitate microstructures of the experimental alloys after T7 treatment (a-h) and (i) typical SADP.

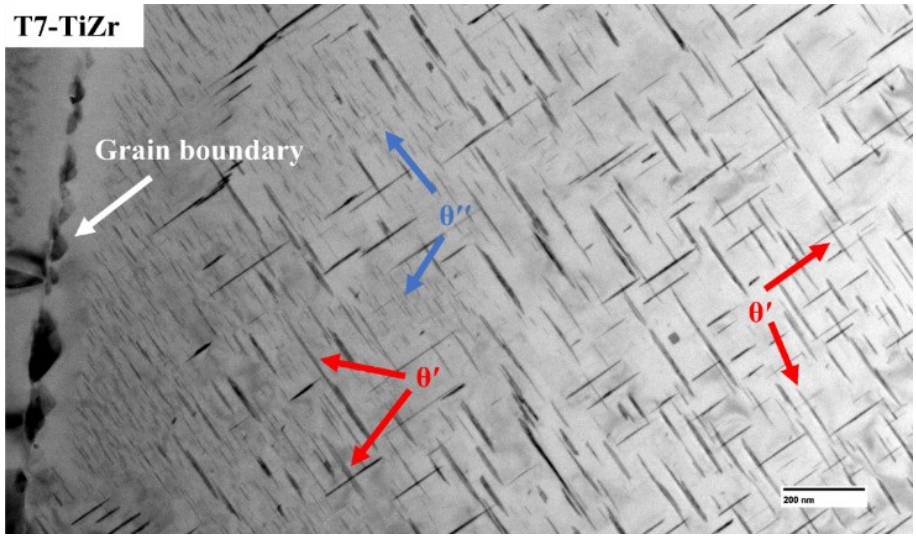

Fig. 3.5 Bright-field TEM images viewed along <001>$_{\alpha\text{-Al}}$ showing a non-uniform distribution of θ″ and θ′ precipitates in the TiZr alloy after T7.

After thermal exposure at 300 ℃ for 100 h to stabilize the microstructure (T7A), θ′ precipitates became the predominant strengthening phase in all the experimental alloys, as shown in the TEM images in Fig. 3.6. During thermal holding at 300 ℃, the θ″ phase was not stable at 300 ℃ and either dissolved into the matrix or transferred into θ′ [10, 35], and then θ′ underwent a coarsening process with increased holding time. The finer the size and the higher the number density of θ′ after thermal exposure, the more thermally stable is the microstructure. The θ′ characteristics after T7A were quantified, and the results are presented in Table 3.3. In general, TEs-containing alloys refined θ′, exhibiting a smaller size (in terms of both length and thickness) and a higher number density than those of the base alloy. When the TEs were added individually, the length of θ′ in the Ti, Zr, and V alloys (150-160 nm) was ~10% shorter than that of the base alloy (171 nm), while the number density was 1.5 to 2 times higher. Among the three individually added alloys, the Zr alloy exhibited the finest distribution of θ′, and thus it was the most effective at stabilizing the θ′ precipitates. In the case of the combination of TEs, the distribution of θ′ was further

improved in the ZrV and TiZrV alloys. For instance, the number density of θ′ was increased from 2.5×10^{-7} (Zr alloy) to 2.7×10^{-7} (TiZrV alloy) and further to 3.2×10^{-7} (ZrV alloy), while the length and thickness of θ′ were in the same range in all three alloys. Based on the quantitative results (Table 3.3), the thermal stabilities of the θ′ precipitates in the eight experimental alloys were distinct in the following sequence:

ZrV alloy > TiZrV alloy > Zr alloy ≈ TiZr alloy > TiV alloy ≈ Ti alloy ≈ V alloy > base alloy.

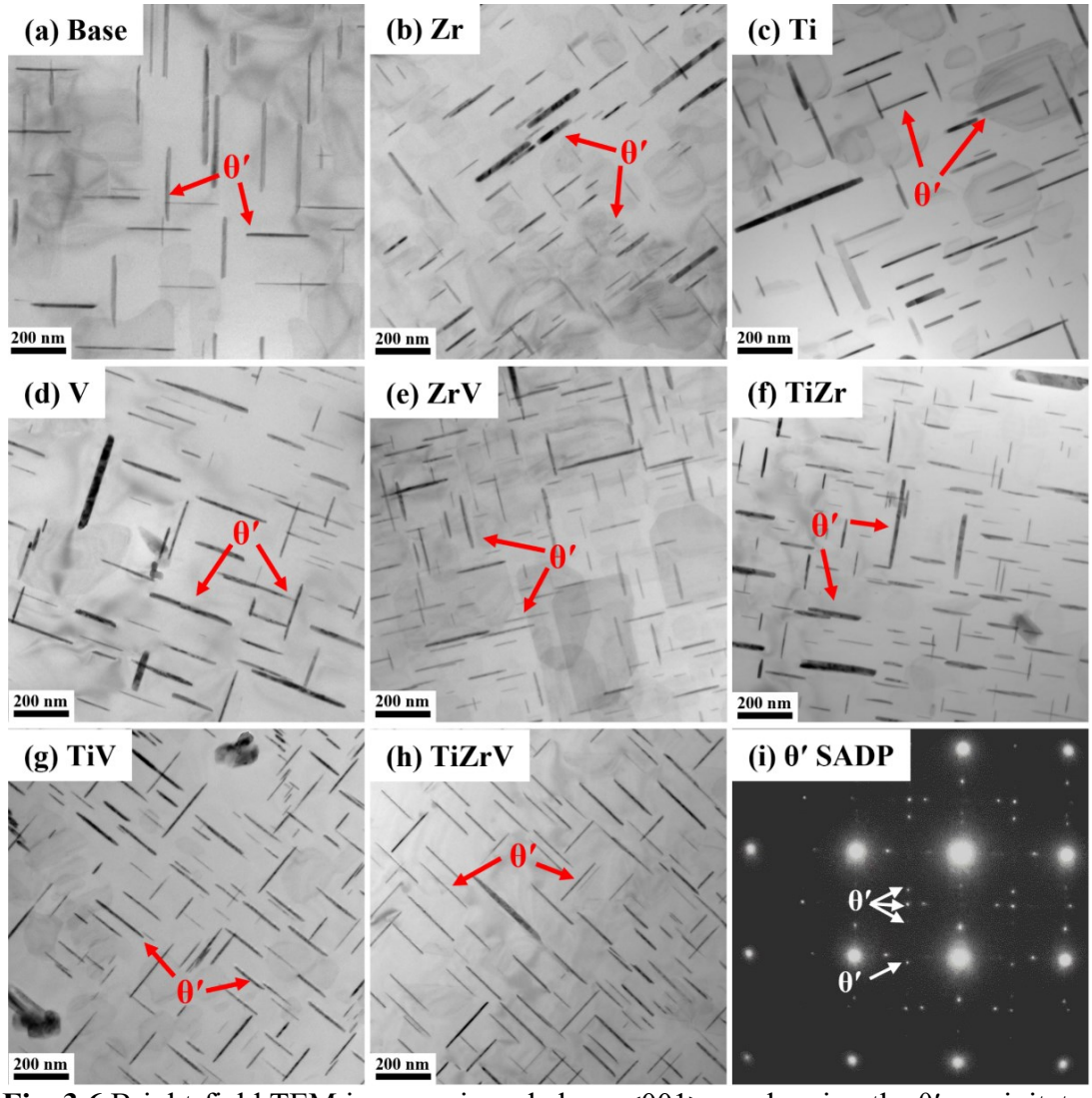

Fig. 3.6 Bright-field TEM images viewed along <001>$_{\alpha\text{-Al}}$ showing the θ′ precipitates of the experimental alloys after T7A treatment (a-h) and (i) typical SADP of θ′.

3.3.2 Mechanical properties

The compressive YS of all the experimental alloys after T7A at room temperature and 300 ℃ are shown in Fig. 3.7. The results revealed that all the TEs-containing alloys exhibited higher YS at both room temperature and 300 ℃ relative to the base alloy, but the enhancement of YS varied from one alloy to another. Zr addition was more effective than Ti or V addition when added individually. As shown in Fig. 3.4, the YS at 300 ℃ of the Zr alloy reached 113 MPa, an increase of 17.7% compared to the base alloy. However, the enhancements provided by Ti and V alloys were 7.3%. The performance of the combination of TEs also changed significantly. For example, the YS at 300 ℃ was significantly improved by the combination of Zr + V and Ti + Zr + V, and it was higher than 130 MPa, with an increase of >35% compared to the base alloy. On the other hand, the elevated temperature YS of the TiV alloy was the same as that of the Ti and V alloys, whereas the TiZr alloy had a moderate increase in YS (14.5%) relative to the base alloy. The change in the YS at room temperature followed the same trend as at 300 ℃. In brief, the impact of the individual and combined additions of TEs on the elevated-temperature YS of the experimental alloys is as follows:

ZrV alloy ≈ TiZrV alloy > Zr alloy ≈ TiZr alloy > TiV alloy ≈ Ti alloy ≈ V alloy > base alloy.

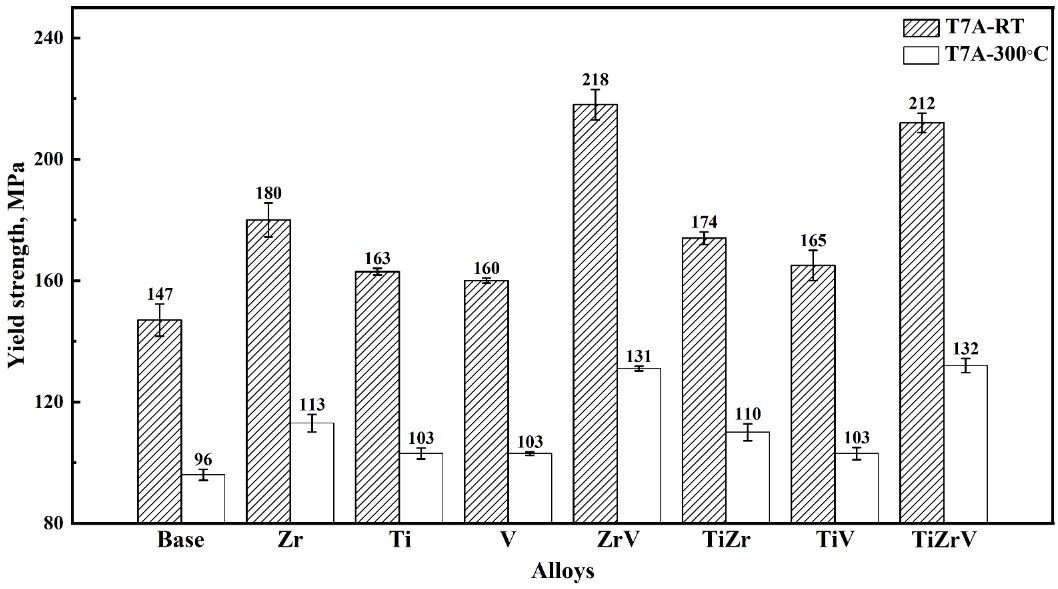

Fig. 3.7 The compressive YS of different TEs-containing alloys at room temperature and 300 ℃ in the T7A state.

3.3.3 Creep behavior

Fig. 3.8 shows the typical compressive creep curves and corresponding creep rate curves tested at 300 ℃ for 100 h on the T7A samples at 50 MPa and 60 MPa. At low applied stresses (45-50 MPa), all alloys displayed two creep stages: the primary stage and the secondary (quasi-steady) stage. At the beginning of creep (primary stage), the creep strain increased sharply owing to work hardening, but the creep rate decreased with time. With further creep deformation, the strain increased constantly, and the creep rate reached its lowest value and remained almost stable at the quasi-steady stage because of the balance between work-hardening and dynamic softening. The quasi-steady stage took the most creep range, and the minimum creep rates were the average values measured from the quasi-steady stage. When the applied stress increased to a high level (55-60 MPa), most alloys still showed two typical creep stages, while the base and Ti alloys displayed a tertiary creep stage after the quasi-steady stage

(Fig. 3.5b and d), in which the creep strain increased sharply and the creep rate was no longer constant. The occurrence of the tertiary creep stage indicates that such alloys lost their microstructural stability and started to fail during creep.

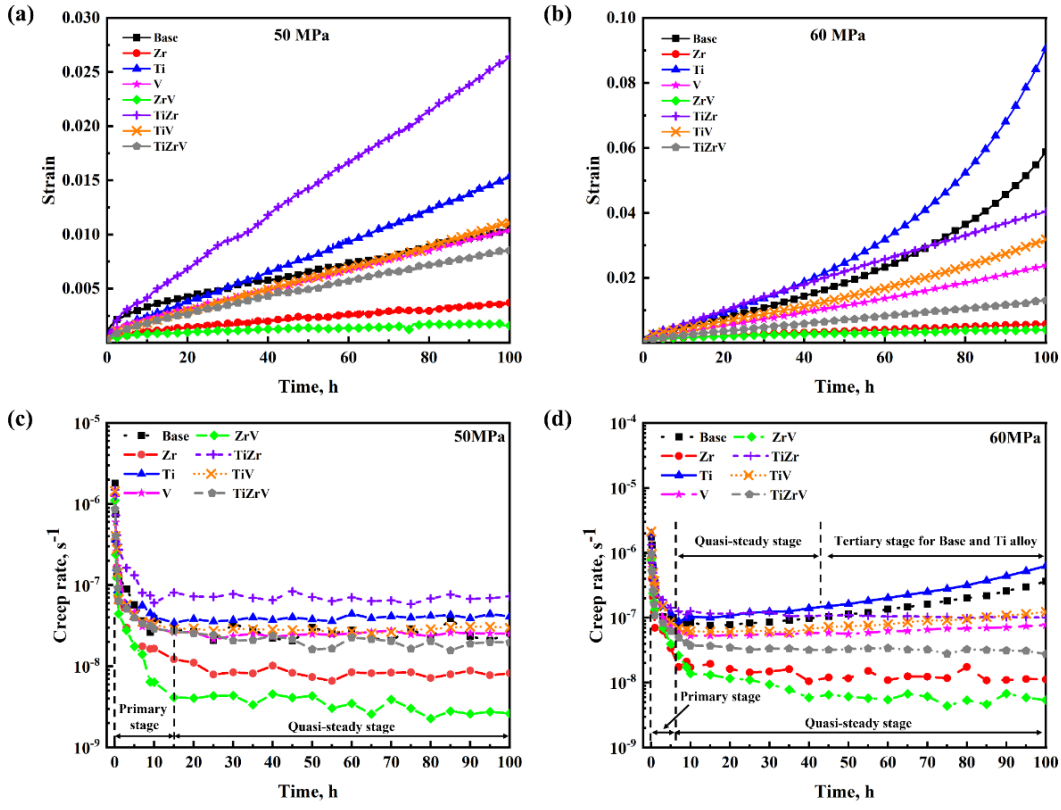

Fig. 3.8 Typical creep curves of the experimental alloys at (a) 50 MPa and (b) 60 MPa, and the creep rate curves at (c) 50 MPa and (d) 60 MPa.

The minimum creep rates and total strains as functions of applied stress are shown in Fig. 3.9. As shown in Fig. 3.9a, a linear fit was applied to obtain the stress exponents for each alloy. The minimum creep rate, which is usually used to indicate the creep resistance, shows a large difference among the TE-containing alloys (Fig. 3.9a). Most Zr-containing alloys, such as Zr, ZrV, and TiZrV alloys, showed lower minimum creep rates compared to the base alloy, indicating enhanced creep resistance. The lowest minimum creep rate was observed for the ZrV alloy. In contrast, the minimum creep rate was higher in the Ti, TiV, V, and TiZr alloys than that in the base

alloys. These alloys had a negative effect on the creep resistance. The total strain exhibited the same tendency as the minimum creep rate when the applied stress was less than 50 MPa (Fig. 3.9b). With a further increase in the applied stress, the base and Ti alloys underwent the tertiary creep stage, which led to a much higher total strain than that of the other alloys, indicating the poorest creep resistance. Based on the different creep behaviors shown in Figs. 3.8 and 3.9, the alloys can be divided into three groups: those with high creep resistance (ZrV, Zr, and TiZrV alloys), those with weak creep resistance (TiV, V, and TiZr alloys), and those with poor creep resistance (Ti and base alloys).

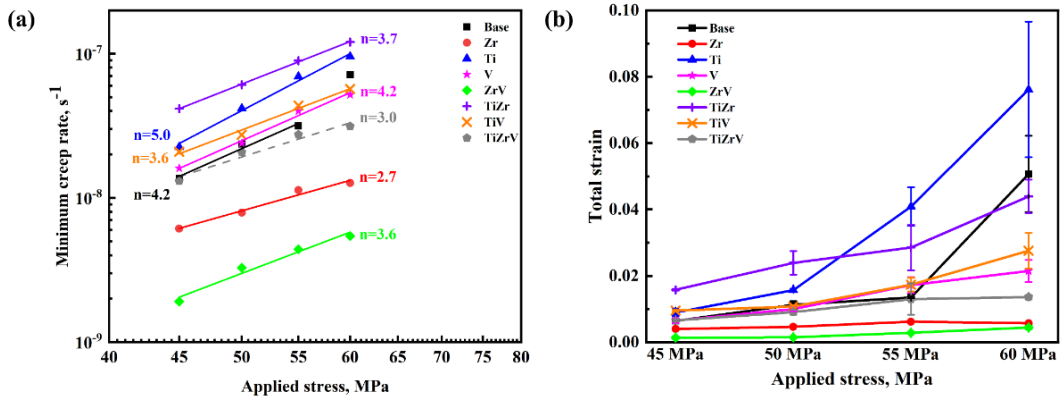

Fig. 3.9 (a) The minimum creep rate (logarithmic scale) and (b) the total strain as a function of applied stress after the creep tests at 300 °C for 100 h.

The relationship between the minimum creep rate and the applied stress can be described by the power-law equation as follows [36-38]:

$$\varepsilon = A\sigma^{n} \exp\left(\frac{-Q}{RT}\right) \tag{3.1}$$

where ε is the minimum creep rate, A is the material constant, σ is the applied stress, n is the stress exponent, Q is the apparent activation energy, T is the absolute temperature, and R is an ideal gas constant.

The values of n correspond to the well-developed creep mechanisms reported in references [26, 39-41]. If n=1, the creep deformation is believed to be dominated by diffusion creep; the value of n=2 is related to grain boundary sliding; and when n=3-6, the creep is mainly controlled by dislocation creep. The value of n in the present work varied from 3 to 5, as shown in Fig. 3.6(a); therefore, the creep process of 224 alloys under applied stresses (45-60 MPa) was believed to be dominated by dislocation creep.

3.3.4 Microstructure evolution during creep

During the creep tests, the T7A samples experienced not only further thermal exposure at 300 ℃ but also external stress. Typical TEM images after the 50 MPa creep tests are shown in Fig. 3.10. The selected diffraction patterns (not shown here) confirmed that the precipitates after the creep test were still θ′ in all experimental alloys. The θ′ characteristics of the creep samples are summarized in Table 3.3. Compared to θ′ before creep (Fig. 3.6 and Table 3.3), the θ′ precipitates after the creep test in all the alloys experienced further coarsening, became longer and thicker, and their number density decreased. In the base alloy, the length and thickness of θ′ increased by 10% and 12.5%, respectively, while the number density decreased by 37%. However, the TEs-containing alloys exhibited a much lower coarsening trend and an increase in the length and thickness of θ′, as well as a minor decrease in the number density. Among the TEs-containing alloys, the Zr-containing alloys (Zr, ZrV, and TiZrV alloys) still displayed higher coarsening resistance, as their number densities of θ′ were 45-70% higher than those of the Ti, V, and TiV alloys.

The interactions between θ′ precipitates and dislocations during creep were observed using TEM. Fig. 3.11 shows typical weak-beam dark-field TEM images for some TE-containing alloys under an applied stress of 50 MPa. Several dislocation segments climbed above the θ′ precipitates. This evidence confirms that the creep mechanism was dominated by dislocation creep in the present work, where the stress exponents of all the experimental alloys ranged between 3 and 5 (Fig. 3.6a).

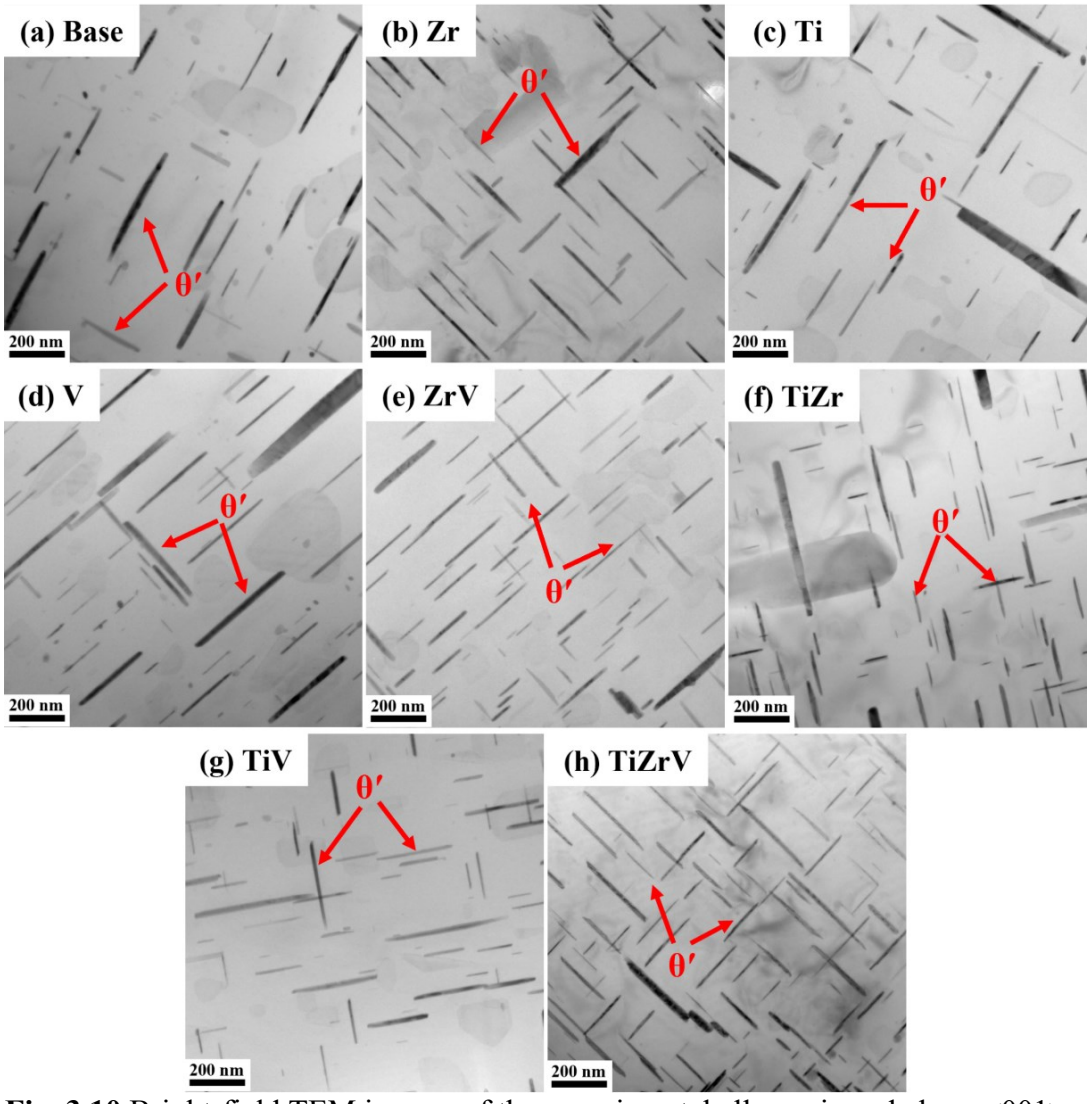

Fig. 3.10 Bright-field TEM images of the experimental alloys viewed along <001>$_{\alpha\text{-Al}}$ after 50 MPa creep tests.

Table 3.3 The quantitative TEM results of the θ′ in the experimental alloys after T7A and 50 MPa creep tests.

Alloys	State	Average length (nm)	Average thickness (nm)	Number density (nm^{-3})
Base	T7A	170.8	14.3	1.2×10^{-7}
	50 MPa Crept	187.9	16.1	7.6×10^{-8}
Zr	T7A	153.5	12.5	2.5×10^{-7}
	50 MPa Crept	166.4	13.9	1.6×10^{-7}
Ti	T7A	156.8	13.2	1.9×10^{-7}
	50 MPa Crept	174.7	14.1	1.1×10^{-7}
V	T7A	162.3	13.7	1.7×10^{-7}
	50 MPa Crept	175.3	14.6	1.1×10^{-7}
ZrV	T7A	146.8	11.7	3.2×10^{-7}
	50 MPa Crept	163.4	13.4	2.0×10^{-7}
TiZr	T7A	153.4	13.0	2.4×10^{-7}
	50 MPa Crept	164.8	13.7	1.5×10^{-7}
TiV	T7A	160.2	13.2	2.0×10^{-7}
	50 MPa Crept	168.6	14.3	1.2×10^{-7}
TiZrV	T7A	159.6	12.4	2.7×10^{-7}
	50 MPa Crept	164.7	13.5	1.8×10^{-7}

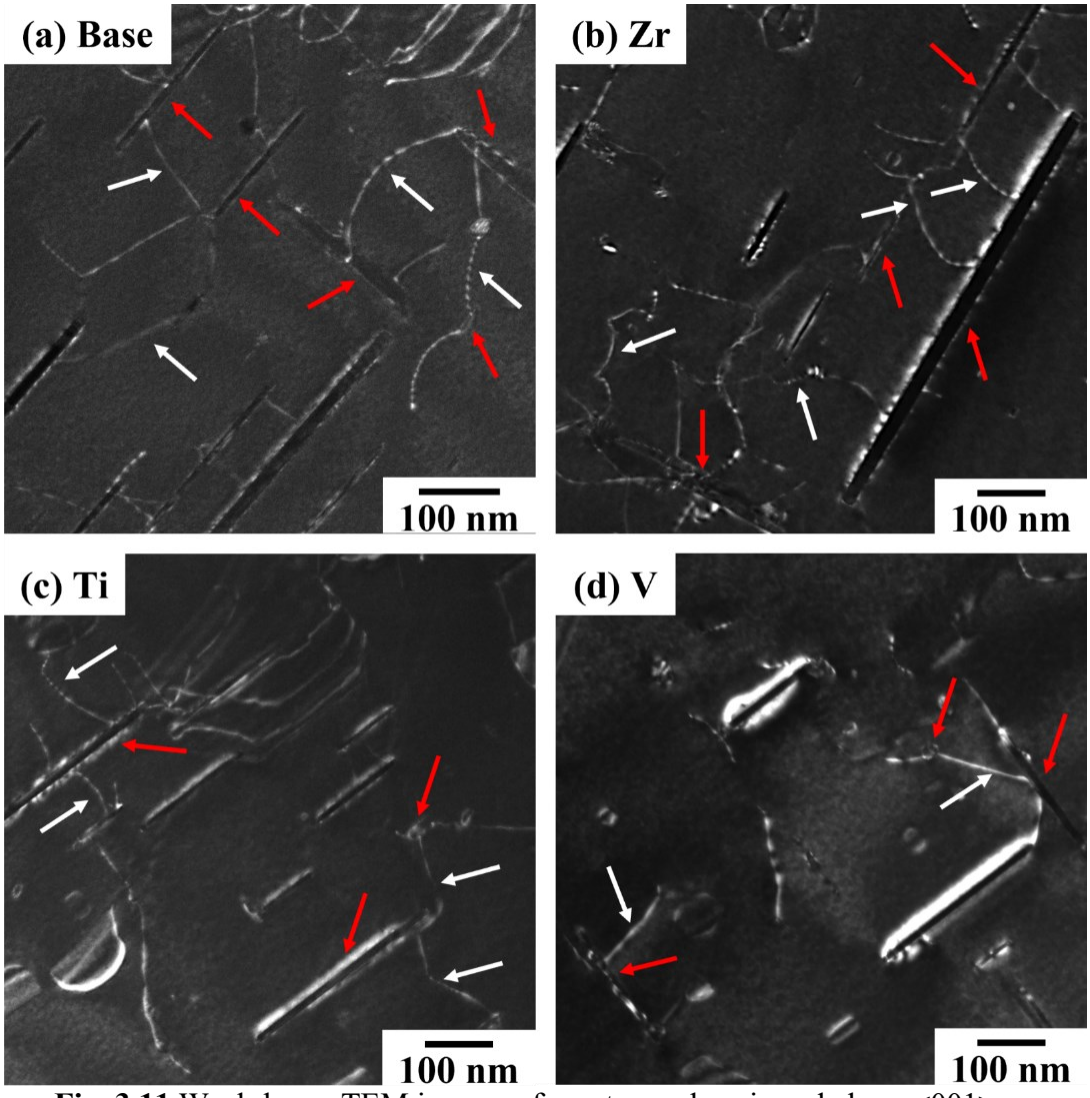

Fig. 3.11 Weak-beam TEM images of crept samples viewed along $<001>_{\alpha\text{-Al}}$ demonstrating the interaction between θ′ precipitates and dislocations. The dislocations and θ′ are marked by the white and red arrows, respectively.

3.4 Discussion

3.4.1 Effect of TEs on the thermal stability of precipitates and the YS

After the T7A treatment and creep test, only θ′ precipitates remained in the aluminum matrix as the strengthening phase (Figs. 3.6 and 3.10). To simplify the characteristics of θ′ and to better describe the θ′ stability, a widely used microstructural

parameter λ, the effective planar interprecipitate spacing, was introduced, which is expressed in the following equation [8, 27, 33].

$$\lambda = 1.23\frac{1.030}{\sqrt{N_v d_t}} - \frac{\pi d_t}{8} - 1.061 t_t \quad (3.2)$$

where N_v, d_t and t_t are the number density, true length, and thickness of the precipitate, respectively.

The effective planar inter-precipitate spacing λ combines the number density, length, and thickness of precipitates to provide a simple and clear description of the distribution of θ′ and the coarsening resistance (thermal stability). The lower the value of λ, the finer the distribution, and the higher the thermal stability of the precipitates during thermal exposure and creep. The λ values of both the T7A-treated and 50 MPa-crept samples were calculated, and the results are shown in Fig. 3.12a. After 100 h of thermal exposure at 300 °C (T7A), the base alloy exhibited a very high value of λ, indicating the poor thermal stability of θ′. In general, a much lower λ value was found in the TEs-containing alloys, indicating the improved thermal stability of θ′. The sequence of the λ values from low to high in all the experimental alloys is as follows: ZrV, TiZrV, Zr, TiZr, TiV, Ti, V, and the base alloys. The results are consistent with the order of the thermal stability of the θ′ precipitates in the alloys as observed by TEM images and quantitative analysis (Fig. 3.6 and Table 3.3). Because of the further thermal exposure to external stress during the creep test, the θ′ in all the samples continued to coarsen. The λ values in the 50 MPa-crept samples were higher than those in the T7A samples (Fig. 3.12a). However, the tendency of the λ value change is nearly

identical to that of the T7A state, and thus the thermal stability of θ′ in different alloys after creep tests is also identical to that in the T7A state.

Al-Cu 224 alloys are typical precipitation-strengthened alloys, and the difference in θ′ distribution (λ) yields different mechanical strengths. The sequence of the λ values is almost the same as the order of the YS in the T7A state (section 3.2, Fig. 3.10). The lower the interprecipitate spacing λ, the higher the elevated-temperature YS of the experimental alloy. As mentioned previously, the base alloy had a coarse precipitate distribution with the highest λ, resulting in the lowest YS at 300 °C. The Zr-containing alloys generally exhibited a finer precipitate distribution with lower λ values, and hence had a higher YS than the Ti/V-containing alloys. Among all the experimental alloys, the ZrV and TiZrV alloys exhibited the lowest λ with the highest YS. With the simplified parameter λ, a close relationship between the YS and thermal stability of the precipitates was established with polynomial fitting and became easily recognizable (Fig. 3.12b), in which the elevated temperature YS depended on the distribution and thermal stability of the main strengthening phase of θ′.

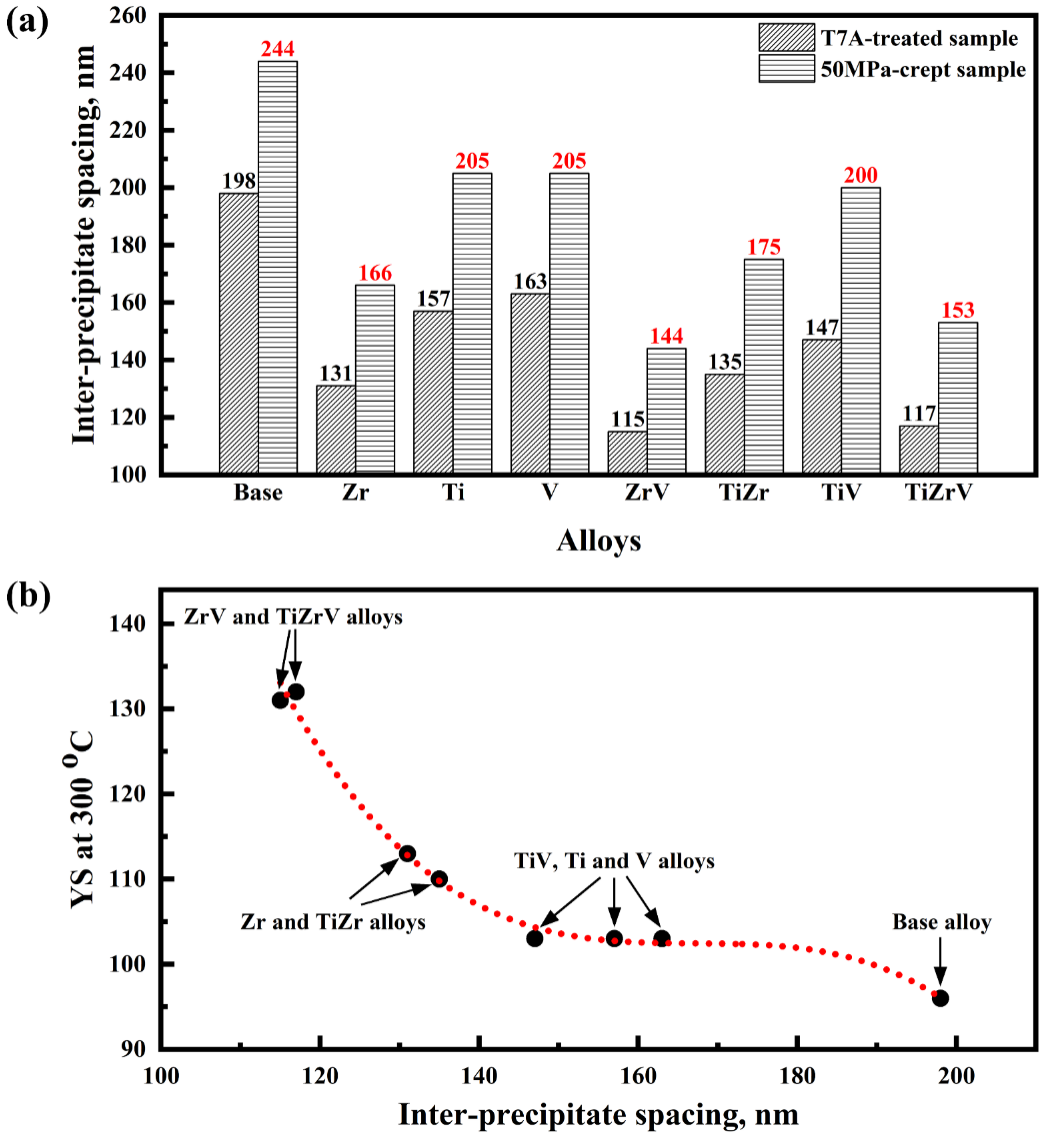

Fig. 3.12 (a) The inter-precipitate spacing of T7A-treated and 50MPa-crept samples and (b) the relationship between the λ and the YS at 300 ℃.

As reported in previous studies [9, 18, 25], there are two possible mechanisms by which the TEs can stabilize θ′. First, the solutes of the TEs diffuse and segregate to the Al/θ′ interfaces, inhibiting coarsening [9, 18]. Second, θ′ heterogeneously nucleated on the Al_3M dispersoids to form compact precipitates, which reduced the elastic strain energy and resulted in significantly delayed coarsening [25].

Because all alloys in this study contained a reasonable amount of Mn (0.35 wt. %), the discussion of the solute segregation includes the Mn and other TEs. During the thermal exposure at 300 ℃ (T7A), Mn diffused much faster and first segregated to the Al/θ′ interfaces because of its higher diffusion rate relative to the other Zr, Ti, and V. This builds the first barrier to retard the growth of θ′. However, this protection is quite weak, as shown for the base alloy. The further stabilization of θ′ during thermal exposure mainly depends on the diffusion rates of Zr, Ti, and V in the aluminum matrix. It is reported that Zr diffuses more than 10 times faster than Ti and more than 1000 times faster than V in the Al matrix at 400 ℃ [19]. Hence, the efficiency of Zr in stabilizing θ′ was higher than that of Ti and V. A schematic illustration of how the TEs (Mn, Zr, Ti, and V) stabilize θ′ is shown in Fig. 3.13. In the base alloy, only Mn solutes segregated to the Al/θ′ interfaces (Fig. 3.13a), and the θ′ precipitates were not fully protected. In the presence of Zr solutes in the Zr alloy (Fig. 3.13b), Mn first segregates to Al/θ′ interfaces to build a first protective layer to allow the Zr solutes to diffuse and segregate to the Al/θ′ interfaces for further protection. The combination of Mn and Zr provides higher protection than the base alloy, resulting in a finer and denser distribution of θ′. For the Ti or V alloys, both solutes would spend a much longer time segregating to Al/θ′ interfaces owing to their lower diffusion rates. As a result, with the same time of thermal exposure, there would be less Ti and V solutes on the Al/θ′ interfaces (Fig. 3.13c), resulting in a coarser θ′ and a weaker thermal stability than the Zr alloy.

It is apparent that for combined additions, Zr-containing alloys would be superior to Ti- or V-containing alloys for building a protective layer in Al/θ′ interfaces.

The λ values of the ZrV and TiZrV alloys were much lower than those of the TiV alloys. Within the Zr-containing alloys, the λ values of the combined additions (ZrV and TiZrV alloys) are also lower than that of the Zr addition alone (the Zr alloy), because more solute atoms of TEs are available in the Al/θ′ interfaces, inhibiting θ′ coarsening. This mechanism (Fig. 3.13) can provide a satisfactory explanation for the different coarsening resistances of the experimental alloys, as shown in Fig. 3.12a.

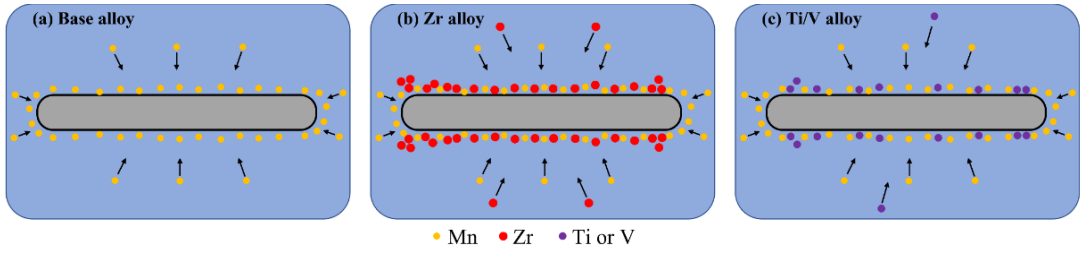

Fig. 3.13 Schematic illustration of the solute segregation in Al/θ′ interfaces to stabilize the θ′ (a) the base alloy only contained Mn, (b) Zr alloy with both Mn and Zr, and (c) the Ti or V alloy with the combination of Mn and Ti or Mn and V.

In the Zr-containing alloys, a reasonable number of Ll_2-Al_3Zr dispersoids were formed during the solution treatment (Fig. 3.14). During aging (T7), the pre-existing Al_3Zr dispersoids provided heterogeneous nucleation sites for θ′, resulting in the formation of compact θ′ precipitates to reduce the interfacial and strain energy [25], as shown in Fig. 3.14a. After further thermal exposure (T7A), the size of the compact θ′ with Al_3Zr was found to be smaller than that of the precipitates without Al_3Zr, as shown in Fig. 3.14b. A recent study [18] found that the microstructure with co-existence of θ′ and Ll_2-Al_3M was highly stable to inhibit the precipitate coarsening beyond 300 °C in Al-Cu alloys. This could be a complementary mechanism to explain the excellent thermal stability of the θ′ precipitates in Zr-containing alloys.

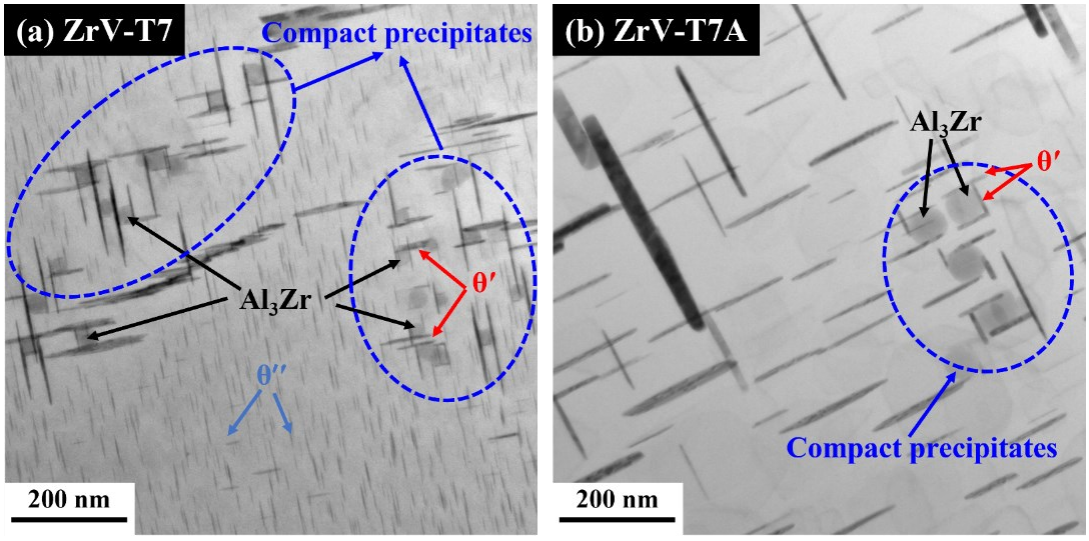

Fig. 3.14 (a) The nucleation and growth of θ′ on Al_3Zr to form compact precipitates during ageing (T7) and (b) the compact θ′ showing a smaller size after thermal exposure (T7A).

3.4.2 Effect of TEs on the creep resistance

The different TEs and their various combined additions exhibited different impacts on the creep resistance, as described in section 3.3 (Figs. 3.8 and 3.9). As the creep deformation was dominated by dislocation creep in all the alloys, the creep resistance was first influenced by the distribution and thermal stability of the θ′ precipitates (λ), which is closely related to the interaction with dislocations and their movement during creep deformation. Prior to the creep test, the base alloy possessed the highest λ, and dislocations moved easily in the Al matrix. In addition, θ′ in the crept sample of the base alloy was severely coarsened, with the highest λ after creep (Figs. 3.10a and 3.12a). The alloy displayed the diminished hindering effect on dislocation movement, causing a short secondary stage and the occurrence of the unstable "ternary stage" and leading to the poorest creep resistance. The Zr-containing alloys (ZrV, Zr, and TiZrV) displayed very low λ values before and after creep, provided a stronger hindering effect on dislocation motion, and resulted in higher creep

resistance compared to the base alloy and Ti/V-containing alloys, which is generally in agreement with the results of creep tests (Section 3.3).

However, the Ti/V-containing alloys (V, TiV, Ti, and TiZr) exhibited a higher minimum creep rate than the base alloy (Fig. 3.9a). This phenomenon is another factor that influences the creep resistance, that is, the grain size. The grain boundaries at high temperatures are weak points, as they provide express channels for dislocation movement. In addition, grain boundary sliding often occurs when the grain size is smaller than a certain value, for example, <50 μm [42, 43]. The smaller the grain size, the larger the grain boundary area, and the weaker the inhibition of dislocation motion and grain rotation during creep. The grain sizes of the V, TiV, Ti, and TiZr alloys were much smaller than those of the base alloy (Fig. 3.2 and Table 3.2). Although these alloys exhibited lower λ than the base alloy, their small grain size resulted in higher minimum creep rates than that of the base alloy before the base alloy was in the ternary stage (Fig. 3.9a). Among the four Ti/V-containing alloys, the TiZr alloy had the lowest λ and the highest minimum creep rate owing to its smallest grain size. The same is true for the Zr-containing alloys (ZrV, Zr, and TiZrV). The TiZrV alloy showed a similar λ to the ZrV alloy and a lower λ than the Zr alloy (Fig. 3.12a); however, its grain size was 3-5 times smaller than that of the Zr and ZrV alloys (Table 3.2). The results of the creep tests showed that the minimum creep rate of the TiZrV alloy was higher and the corresponding creep resistance was lower than those of the two alloys (Fig. 3.9a).

3.4.3 Comparison of the overall performance at elevated temperature for different alloys

It is apparent that the Zr-containing alloys exhibited excellent elevated-temperature YS and superior creep resistance. However, the poisonous effect of Zr addition in both Zr and ZrV alloys on grain refinement caused a very coarse grain structure. The grain sizes of the ZrV and Zr alloys reached 124 and 194 μm, respectively, which were several times higher than those of the other TE-containing alloys (Table 3.2). In general, Al-Cu cast alloys are highly susceptible to hot tearing during solidification and casting [44]. The coarse grain structure causes severe hot tearing and reduces castability, which limits the application of Al-Cu cast alloys [45]. Numerous studies have shown that a fine equiaxed grain structure in cast aluminum alloys can significantly reduce the susceptibility to hot tearing [45-47]. In the present work, the further addition of Ti as a grain growth restrictor in Zr-containing alloys could compensate for the Zr poisoning effect and effectively refine the grain structure. Instead of a relatively low Ti (0.05 wt.%) in Zr and ZrV alloys, the TiZrV alloy contained 0.17 wt.% Ti, resulting in a much finer grain size of 39 μm, which is expected to have a low susceptibility to hot tearing.

To compare the overall performance at elevated temperatures for all the experimental alloys, a schematic chart is illustrated in Fig. 3.15 based on the three factors (YS, creep resistance, and grain structure) and their ranking discussed above. It can be seen that both ZrV and TiZrV alloys achieved excellent YS and creep resistance, but the ZrV alloy had the worst coarse grain structure. In terms of the comprehensive properties — excellent elevated-temperature YS, superior creep

resistance, and fine grain structure — the TiZrV alloy outperformed the eight experimental alloys studied and could be considered the first choice from an industrial and engineering standpoint.

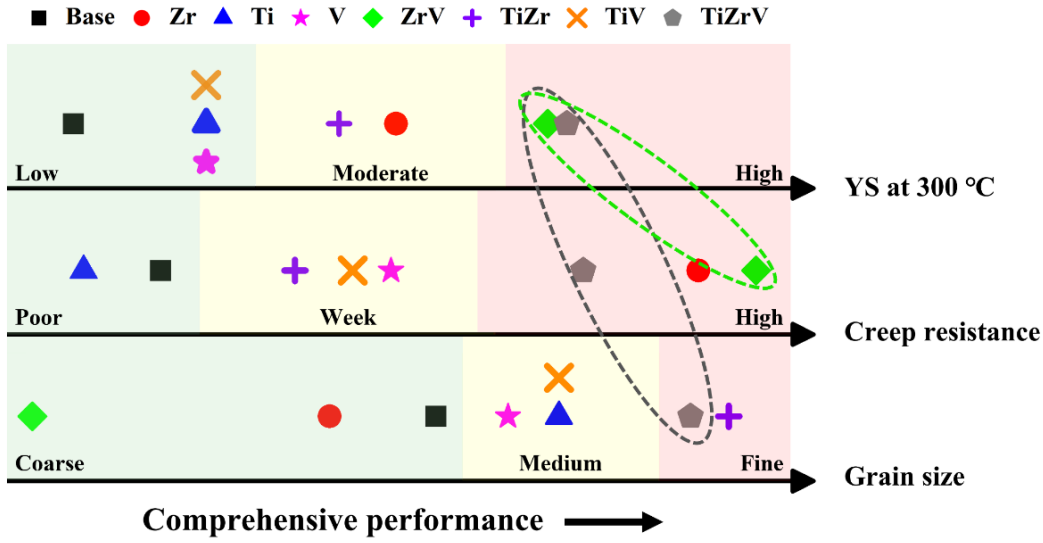

Fig. 3.15 The comprehensive elevated-temperature performance of all the experimental alloys.

3.5 Conclusions

1) The addition of three transition elements (Zr, Ti, and V) significantly increased the coarsening resistance of θ′ precipitates during thermal exposure at 300 ℃ (T7A state) and further creep deformation, resulting in finer and more densely distributed θ′ relative to the base alloy. When the TEs were individually added, Zr addition showed the best efficiency for stabilizing θ′. The efficiency was enhanced by the combined addition of TEs, and the combination of Zr + V and Zr + Ti + V yielded the highest efficiency.

2) The addition of TEs considerably improves the yield strength at both room temperature and 300 ℃. When added individually, Zr addition was more effective

than Ti or V addition. With combined additions, both ZrV and TiZrV alloys achieved the highest YS at 300 ℃ after T7A. A close relationship between YS and the distribution and thermal stability of the θ′ precipitates was observed.

3) The creep resistance at elevated temperatures was affected by the thermal stability of θ′ and grain size of the Al-Cu 224 alloys. The Zr-containing alloys (ZrV, Zr, and TiZrV) exhibited superior creep resistance owing to the excellent thermal stability of θ′, whereas the Ti/V-containing alloys (Ti, V, TiV, and TiZr) had a negative effect on the creep resistance due to their small grain size.

4) To avoid the coarse grain structure and reduce the susceptibility to hot tearing, the combined addition of the TiZrV alloy exhibited the optimum elevated-temperature performance and would be the best choice among the eight experimental alloys studied.

References

[1] M. Javidani, D. Larouche, Application of cast Al–Si alloys in internal combustion engine components, Int. Mater. Rev. 59.3 (2014) 132-158. https://doi.org/10.1179/1743280413Y.0000000027

[2] M. Garat, J.F. Major, D. Jean, Copper aluminum alloy molded part having high mechanical strength and hot creep resistance, 2012, U.S. Patent App. No. 13/516,799.

[3] A. Shyam, Y. Yamamoto, D. Shin, S. Roy, J.A. Haynes, P.J. Maziasz, A. Sabau, A.F. Rodriguez-Jasso, J.A. Gonzalez-Villarreal, J. Talamantes-Silva, L. Zhang, C.R. Glaspie, S. Mirmiran, Aluminum alloy compositions and methods of making and using the same. 2017, US Patent App. 15/160,926.

[4] A. Guinier, Heterogeneities in solid solutions, Solid State Phys., Academic Press 9 (1959) 293-398. https://doi.org/10.1016/S0081-1947(08)60568-8

[5] V.A. Phillips, High resolution electron microscope observations on precipitation in Al-3.0% Cu alloy, Acta Metall. 23.6 (1975) 751-767. https://doi.org/10.1016/0001-6160(75)90058-9

[6] A.W. Zhu, E.A. Starke, Stress aging of Al–xCu alloys: experiments, Acta mater. 49.12 (2001) 2285-2295. https://doi.org/10.1016/S1359-6454(01)00119-7

[7] T. Nakajima, M. Takeda, T. Endo, Accelerated coarsening of precipitates in crept Al–Cu alloys, Mater. Sci. Eng. A 387 (2004) 670-673. https://doi.org/10.1016/j.msea.2004.01.131

[8] S. Roy, L.F. Allard, A. Rodriguez, W.D. Porter, A. Shyam, Comparative evaluation of cast aluminum alloys for automotive cylinder heads: Part II—mechanical and thermal properties, Metall. Mater. Trans. A 48.5 (2017) 2543-2562. https://doi.org/10.1007/s11661-017-3986-0

[9] A. Shyam, S. Roy, D. Shin, J.D. Poplawsky, L.F. Allard, Y. Yamamoto, J.R. Morris, B. Mazumder, J.C. Idrobo, A. Rodriguez, T.R. Watkins, J.A. Haynes, Elevated temperature microstructural stability in cast AlCuMnZr alloys through solute segregation, Mater. Sci. Eng. A 765 (2019): 138279. https://doi.org/10.1016/j.msea.2019.138279

[10] J. Rakhmonov, K. Liu, L. Pan, F. Breton, X.G. Chen, Enhanced mechanical properties of high-temperature-resistant Al–Cu cast alloy by microalloying with Mg, J. Alloys Compd. 827 (2020): 154305. https://doi.org/10.1016/j.jallcom.2020.154305

[11] D. Li, K. Liu, J. Rakhmonov, X.G. Chen, Enhanced thermal stability of precipitates and elevated-temperature properties via microalloying with transition metals (Zr, V and Sc) in Al–Cu 224 cast alloys, Mater. Sci. Eng. A 827 (2021): 142090. https://doi.org/10.1016/j.msea.2021.142090

[12] Y. H. Gao, L.F. Cao, C. Yang, J.Y. Zhang, G. Liu, J. Sun, Co-stabilization of θ′-Al_2Cu and Al3Sc precipitates in Sc-microalloyed Al–Cu alloy with enhanced creep resistance, Mater. Today Nano 6 (2019): 100035. https://doi.org/10.1016/j.mtnano.2019.100035

[13] B. Rouxel, M. Ramajayam, T.J. Langan, J. Lamb, P. G. Sanders, T. Dorin, Effect of dislocations, Al3 (Sc, Zr) distribution and ageing temperature on θ′ precipitation in Al-Cu-(Sc)-(Zr) alloys, Mater. 9 (2020): 100610. https://doi.org/10.1016/j.mtla.2020.100610

[14] Y.H. Gao, L.F. Cao, J. Kuang, J.Y. Zhang, G. Liu, J. Sun, Assembling dual precipitates to improve high-temperature resistance of multi-microalloyed Al–Cu alloys, J. Alloys Compd. 822 (2020): 153629. https://doi.org/10.1016/j.jallcom.2019.153629

[15] B.A. Chen, G. Liu, R.H. Wang, J.Y. Zhang, L. Jiang, J.J. Song, J. Sun, Effect of interfacial solute segregation on ductile fracture of Al–Cu–Sc alloys, Acta mater. 61.5 (2013) 1676-1690. https://doi.org/10.1016/j.actamat.2012.11.043

[16] C. Yang, P. Zhang, D. Shao, R.H. Wang, L.F. Cao, J.Y. Zhang, G. Liu, B.A. Chen, J. Sun, The influence of Sc solute partitioning on the microalloying effect and

mechanical properties of Al-Cu alloys with minor Sc addition, Acta Mater. 119 (2016) 68-79. https://doi.org/10.1016/j.actamat.2016.08.013

[17] D. Shin, A. Shyam, S. Lee, Y. Yamamoto, J.A. Haynes, Solute segregation at the Al/θ′-Al_2Cu interface in Al-Cu alloys, Acta Mater. 141 (2017) 327-340. https://doi.org/10.1016/j.actamat.2017.09.020

[18] J. D. Poplawsky, B.K. Milligan, L.F. Allard, D. Shin, P. Shower, M.F. Chisholm, A. Shyam, The synergistic role of Mn and Zr/Ti in producing θ′/L12 co-precipitates in Al-Cu alloys, Acta Mater. 194 (2020) 577-586. https://doi.org/10.1016/j.actamat.2020.05.043

[19] K.E. Knipling, D.C. Dunand, D.N. Seidman, Criteria for developing castable, creep-resistant aluminum-based alloys–A review, Int. J. Mater. Res. 97.3 (2006) 246-265. https://doi.org/10.3139/ijmr-2006-0042

[20] B.K. Milligan, S. Roy, C.S. Hawkins, L.F. Allard, A. Shyam, Impact of microstructural stability on the creep behavior of cast Al–Cu alloys, Mater. Sci. Eng. A 772 (2020): 138697. https://doi.org/10.1016/j.msea.2019.138697

[21] J.U. Rakhmonov, S. Bahl, A. Shyam, D.C. Dunanda, Cavitation-resistant intergranular precipitates enhance creep performance of θ′-strengthened Al-Cu based alloys, Acta Mater. (2022): 117788. https://doi.org/10.1016/j.actamat.2022.117788

[22] S. Mondol, S. Kashyap, S. Kumar, K. Chattopadhyay, Improvement of high temperature strength of 2219 alloy by Sc and Zr addition through a novel three-stage heat treatment route, Mater. Sci. Eng. A 732 (2018) 157-166. https://doi.org/10.1016/j.msea.2018.07.003

[23] Y.H. Gao, C. Yang, J.Y. Zhang, L.F. Cao, G. Liu, J. Sun, Stabilizing nanoprecipitates in Al-Cu alloys for creep resistance at 300 °C, Mater. Res. Lett. 7.1 (2019) 18-25. https://doi.org/10.1080/21663831.2018.1546773

[24] Z.C. Sims, O.R. Rios, D. Weiss, P.E.A. Turchi, A. Perron, J.R.I. Lee, T.T. Li, J.A. Hammons, M. Bagge-Hansen, T.M. Willey, K. An, Y. Chen, A.H. King, S.K. McCall, High performance aluminum–cerium alloys for high-temperature applications, Mater. Horiz. 4.6 (2017) 1070-1078. https://doi.org/10.1039/C7MH00391A

[25] S.K. Makineni, S. Sugathan, S. Meher, R. Banerjee, S. Bhattacharya, S. Kumar, K. Chattopadhyay, Enhancing elevated temperature strength of copper containing aluminium alloys by forming L12 Al3Zr precipitates and nucleating θ″ precipitates on them, Sci. Rep. 7.1 (2017) 1-9. https://doi.org/10.1038/s41598-017-11540-2

[26] P. Hu, K. Liu, L. Pan, X.G. Chen, Effect of Mg microalloying on elevated-temperature creep resistance of Al–Cu 224 cast alloys, Mater. Sci. Eng. A 851 (2022): 143649. https://doi.org/10.1016/j.msea.2022.143649

[27] J.F. Nie, B.C. Muddle, Strengthening of an Al–Cu–Sn alloy by deformation-resistant precipitate plates, Acta Mater. 56 (2008) 3490-3501. https://doi.org/10.1016/j.actamat.2008.03.028

[28] J. Li, F.S. Hage, Q.M. Ramasse, P. Schumacher, The nucleation sequence of α-Al on TiB2 particles in Al-Cu alloys, Acta Mater. 206 (2021): 116652. https://doi.org/10.1016/j.actamat.2021.116652

[29] B.S. Murty, S.A. Kori, M. Chakraborty, Grain refinement of aluminium and its alloys by heterogeneous nucleation and alloying, Int. Mater. Rev. 47.1 (2002) 3-29. https://doi.org/10.1179/095066001225001049

[30] D. Qiu, J.A. Taylor, M.-X. Zhang, Understanding the co-poisoning effect of Zr and Ti on the grain refinement of cast aluminum alloys, Metall. Mater. Trans. A 41.13 (2010) 3412-3421. https://doi.org/10.1007/s11661-010-0404-2

[31] C. Wolverton, Solute–vacancy binding in aluminum, Acta Mater. 55.17 (2007) 5867-5872. https://doi.org/10.1016/j.actamat.2007.06.039

[32] J. Peng, S. Bahl, A. Shyam, J.A. Haynes, D. Shin, Solute-vacancy clustering in aluminum, Acta Mater. 196 (2020) 747-758. https://doi.org/10.1016/j.actamat.2020.06.062

[33] S. Mondol, S.K. Makineni, S. Kumar, K. Chattopadhyay, Enhancement of high temperature strength of 2219 alloys through small additions of Nb and Zr and a novel heat treatment, Metall. Mater. Trans. A 49.7 (2018) 3047-3057. https://doi.org/10.1007/s11661-018-4614-3

[34] K.E. Knipling, D.C. Dunand, D.N. Seidman, Precipitation evolution in Al–Zr and Al–Zr–Ti alloys during isothermal aging at 375–425 ℃, Acta Mater. 56.1 (2008) 114-127. https://doi.org/10.1016/j.actamat.2007.09.004

[35] Z. Shen, Q. Ding, C. Liu, J. Wang, H. Tian, J. Li, Z. Zhang, Atomic-scale mechanism of the θ″→ θ′ phase transformation in Al-Cu alloys, J. Mater. Sci. Technol. 33.10 (2017) 1159-1164. https://doi.org/10.1016/j.jmst.2016.08.031

[36] L. Jin, K. Liu, X.G. Chen, Evolution of dispersoids and their effects on elevated-temperature strength and creep resistance in Al-Si-Cu 319 cast alloys with Mn and Mo additions, Mater. Sci. Eng. A 770 (2020): 138554. https://doi.org/10.1016/j.msea.2019.138554

[37] D. Yao, W. Zhao, H. Zhao, F. Qiu, Q. Jiang, High creep resistance behavior of the casting Al–Cu alloy modified by La, Scripta Mater. 61 (2009) 1153-1155. https://doi.org/10.1016/j.scriptamat.2009.09.007

[38] M.E. Kassner, Fundamentals of creep in metals and alloys, Butterworth-Heinemann, 2015.

[39] Y. Xu, L. Zhan, L. Xu, M. Huang, Experimental research on creep aging behavior of Al-Cu-Mg alloy with tensile and compressive stresses, Mater. Sci. Eng. A 682 (2017) 54-62. https://doi.org/10.1016/j.msea.2016.11.043

[40] C. Yang, L. Cao, Y. Gao, P. Cheng, P. Zhang, J. Kuang, J. Zhang, J. Sun, Nanostructural Sc-based hierarchy to improve the creep resistance of Al–Cu alloys, Mater. Des. 186 (2020): 108309. https://doi.org/10.1016/j.matdes.2019.108309

[41] W.S. Tian, Q.L. Zhao, Q.Q. Zhang, F. Qiu, Q.C. Jiang, Superior creep resistance of 0.3 wt% nano-sized TiCp/Al-Cu composite, Mater. Sci. Eng. A 700 (2017) 42-48. https://doi.org/10.1016/j.msea.2017.05.101

[42] O.D. Sherby, E.M. Taleff, Influence of grain size, solute atoms and second-phase particles on creep behavior of polycrystalline solids, Mater. Sci. Eng. A 322.1-2 (2002) 89-99. https://doi.org/10.1016/S0921-5093(01)01121-2

[43] K.R. Athul, U.T.S. Pillai, A. Srinivasan, B.C. Pai, A review of different creep mechanisms in Mg alloys based on stress exponent and activation energy, Adv. Eng. Mater. 18.5 (2016) 770-794. https://doi.org/10.1002/adem.201500393

[44] H.K. Kamga, D. Larouche, M. Bournane, A. Rahem, Hot tearing of aluminum–copper B206 alloys with iron and silicon additions, Mater. Sci. Eng. A 527.27-28 (2010) 7413-7423. https://doi.org/10.1016/j.msea.2010.08.025

[45] S. Li, K. Sadayappan, D. Apelian, Role of grain refinement in the hot tearing of cast Al-Cu alloy, Metall. Mater. Trans. B 44.3 (2013) 614-623. https://doi.org/10.1007/s11663-013-9801-4

[46] M. Easton, H. Wang, J. Grandfield, D. StJohn, E. Sweet, An analysis of the effect of grain refinement on the hot tearing of aluminium alloys, Mater. forum. 28 (2004) 224-229

[47] M. Easton, J.F. Grandfield, D.H. StJohn, B. Rinderer, The effect of grain refinement and cooling rate on the hot tearing of wrought aluminium alloys, Mater. Sci. forum. Trans Tech Publications Ltd, 519 (2006) 1675-1680. https://doi.org/10.4028/www.scientific.net/MSF.519-521.1675

Chapter 4

Effect of Mg on elevated-temperature low cycle fatigue and thermo-mechanical fatigue behaviors of Al-Cu cast alloys

(Published in the journal of Materials Science and Engineering: A

doi.org/10.1016/j.msea.2023.145588)

Abstract

The effects of Mg addition on the cyclic deformation and fatigue life behaviors of Al-Cu 224 cast alloys were investigated under isothermal low cycle fatigue (LCF) at 300 ℃ and out-of-phase thermo-mechanical fatigue (OP-TMF) in the temperature range 60–300 ℃. The results show that all tested alloys experienced cyclic softening during both LCF and OP-TMF, whereas the softening ratio of Mg-containing alloys was lower than that of the base alloy free of Mg because of the lower coarsening rate of θ'-Al_2Cu precipitates. Under both LCF and TMF, near-surface porosity and brittle intermetallic particles were considered sources of crack initiation. TMF lives were inferior to LCF lives under the same strain amplitude because of the combined damage effect of the cyclic mechanical and thermal loadings. Under LCF, the addition of Mg enhanced the fatigue performance because of the co-existing θ″ and θ′ precipitates and the higher thermal resistance of θ′; under TMF, it led to a slight reduction in fatigue performance. The hysteresis energy model was successfully applied to predict the LCF and TMF lifetimes. The predicted results agree well with the experimentally measured LCF and TMF lifetimes.

Keywords: Al-Cu 224 cast alloys, Mg addition, low cycle fatigue, thermo-mechanical fatigue, fatigue life prediction, hysteresis energy model.

4.1 Introduction

Over the past decades, aluminum cast alloys have been increasingly used in the transportation industry as replacements for gray cast iron in the manufacture of combustion engine components such as engine blocks and cylinder heads. Aluminum-cast alloys have several advantages such as light weight, high castability, and high thermal conductivity. The most commonly used cast aluminum alloys for engine components include the Al-Si (e.g., 356/A356) and Al-Si-Cu (e.g., 319/A319) alloy series [1, 2]. However, current engine developments require a high operating temperature (~300 ℃) and an enhanced combustion pressure (~200 bar) [3]. The relatively poor high-temperature properties of Al-Si and Al-Si-Cu cast alloys (e.g. 356/319 types) cannot meet the requirements of the future engine, and therefore, their application temperature is limited to < 250 ℃. Compared with these alloy series, Al-Cu alloys display better mechanical properties at both room and elevated temperatures as well as better thermal resistance. Our previous works revealed that Al-Cu cast alloys exhibited excellent thermal stability at 300 ℃ with the microalloying of Mg, Mn, and other transition elements [4-7]. Thus, Al-Cu cast alloys with superior elevated-temperature properties are promising alternatives for structural engine component applications [3, 8].

During service, except for the assembly load and combustion pressure, thermal gradients caused by the transient regime of the startup and shutdown operations can produce complex mechanical and thermal fatigue loading, which can limit the service life of the engine components. Engine blocks and cylinder heads are normally

subjected to low-cycle fatigue (LCF) and out-of-phase thermomechanical fatigue (OP-TMF) damage [2, 9, 10]. Several studies have been conducted on Al-Si and Al-Si-Cu alloys to investigate the different factors influencing the behavior of LCF and TMF and to improve fatigue behavior. Further, many approaches have been proposed, such as controlling the size of the casting defects (e.g., porosity and oxide films) [11-13] and the secondary dendrite arm spacing [14, 15], modifying the brittle phases [2, 16-18] and eutectic microstructure [19, 20], and optimizing the heat treatments [21-23]. Few studies have also compared the LCF and TMF behaviors for these two-alloy series; these studies reported that TMF resulted in a shorter lifetime than isothermal LCF [22, 24]. Further, this phenomenon was observed in Ni-based superalloys [25]. However, little work has been conducted on the LCF and TMF behaviors of Al-Cu alloys, particularly at elevated temperatures.

In addition to improving the fatigue performance of structural materials, it is important to establish a reliable model for predicting fatigue life for material design. Classical models for fatigue life prediction can be divided into two types: stress amplitude-based and strain-amplitude-based models. The typical stress-amplitude-based Basquin relation is used for the life prediction of high-cycle fatigue (HCF) because the operating stress is below the elastic limit [26, 27]. This relationship can be expressed as [28]:

$$\frac{\Delta\sigma}{2} = \sigma_f'\left(2N_f\right)^b \tag{4.1}$$

where N_f, $\Delta\sigma/2$, σ_f', and b represent the fatigue life of materials, stress amplitude, fatigue strength coefficient, and fatigue strength exponent, respectively. Strain-

amplitude-based models are more suitable for LCF life prediction [26, 27], resulting from relatively high strain and stress observed during LCF process. The plastic strain based on the Coffin–Manson model is widely used [29, 30].

$$\frac{\Delta\varepsilon_P}{2} = \varepsilon_f'\left(2N_f\right)^c \tag{4.2}$$

where $\Delta\varepsilon_p/2$, ε_f', and c represents the plastic strain amplitude, fatigue ductility coefficient, and fatigue ductility exponent, respectively. However, both classical stress- and strain-based approaches have been considered for uniaxial fatigue tests and can be used under constant conditions such as a constant test temperature [31, 32].

TMF life prediction is more complex than that of HCF and LCF because the temperature and stress/strain change simultaneously during fatigue loading. Thus far, several attempts have been made to employ various approaches; for example, the damage mechanism-based models proposed by Halford et al. [33], Neu and Sehitoglu [34], and Lemaitre and Chaboche [35, 36]; fracture mechanic-based models developed through cyclic J-integrals [37]; and energy-based approaches based on the dissipated energy per cycle [38, 39]. Among these, the energy-based models are more suitable for thermomechanical loadings because of their high accuracy and low number of material constants [32].

In our previous works [4–6], we demonstrated that the high-temperature properties (e.g., strength and creep resistance) and thermal stability of Al-Cu 224 cast alloys could be improved by adding Mg. In this study, the effects of Mg on the high-temperature LCF and TMF behaviors are investigated. The cyclic deformation and

fatigue life behaviors of different Mg-containing alloys during isothermal LCF at 300 ℃ and OP-TMF in the temperature range 60–300 ℃ at different strain amplitude (0.2%–0.6%) were compared. The microstructural evolution, damage mechanism, and fracture surfaces of both LCF and TMF were also analyzed. Further, a hysteresis energy model was applied to predict both the LCF and TMF fatigue lives.

4.2 Experimental procedures

Three Al-Cu 224 cast alloys with different Mg levels (0.01–0.24 wt.%) were prepared and melted in an electric resistance furnace under ambient atmosphere. After reaching 750 °C, the liquid metal was degassed with pure argon for 10 min and then grain refined using an AlTi5B1 master alloy. The liquid metal was cast at 720 ℃ into a permanent wedge mold preheated to 250 °C. The chemical compositions of alloys analyzed by optical emission spectroscopy are listed in Table 4.1. After casting, the experimental alloys were subjected to a two-step solution treatment (495 ℃/2 h + 528 ℃/10 h) followed by a water quench at room temperature and artificial aging at 200 ℃ for 4 h. This heat treatment was referred to as T7. To study the thermal stability of alloys, a 100-h thermal exposure at 300 ℃ under ambient air environment was applied to T7-treated samples; this is designated as the T7A treatment.

Table 4.1 Chemical compositions of experimental 224 alloys (wt.%).

ID	Si	Fe	Cu	Mn	Mg	Ti	V	Zr	Al
0Mg	0.04	0.11	4.68	0.34	**0.01**	0.17	0.21	0.14	Bal.
0.12Mg	0.04	0.11	4.69	0.34	**0.12**	0.17	0.21	0.15	Bal.
0.24Mg	0.04	0.08	4.71	0.36	**0.24**	0.15	0.18	0.14	Bal.

Fatigue samples were cut from wedge-mold castings (Fig. 4.1a). Cylindrical fatigue samples (length = 75 mm; diameter = 10 mm) were designed and then machined in accordance with ASTM E606 and E2368 standards (Fig. 4.1b). For TMF fatigue samples, a central hole of 5 mm diameter was drawn for air circulation to achieve the desired cooling rate, whereas cylindrical samples without hole were used for the LCF fatigue samples. Both LCF and TMF tests were conducted on a Gleeble 3800 thermal–mechanical physical simulation system using the T7-treated samples. The temperature was monitored and controlled using a thermocouple spot-welded at the center of the gauge length. All samples were heated using a Joule heating system. For the LCF tests, tension–compression loading tests with strain-controlled symmetric triangular waveform were performed at total strain amplitudes ($\Delta\varepsilon_t/2$) of 0.2%, 0.3%, 0.4%, and 0.6% and at 300 °C. The strain ratio was set to $R_\varepsilon = -1$ with a strain rate of 1×10^{-3} s^{-1}.

OP-TMF is the main damage mechanism in engine components [2], wherein the maximum mechanical strain is reached at the minimum temperature; therefore, all TMF tests in this study were strain-controlled OP-TMF. During testing, the temperature was varied between 60 °C and 300 °C for one cycle at heating and cooling rates of 5 °C/s. The TMF samples were cooled by passing compressed air through an air hole in the sample. The tests were conducted under mechanical strain amplitudes of 0.2%, 0.3%, 0.4%, 0.5%, and 0.6%. Fatigue tests were stopped automatically when the stress decreased to 70% of the initial maximum value. Further details on the reliable TMF test procedure for aluminum alloys in the Gleeble 3800 system have been reported in a previous study [40].

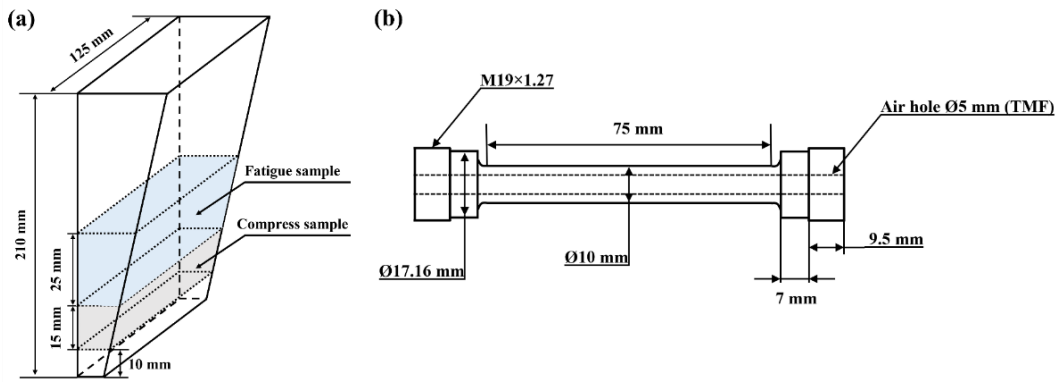

Fig. 4.1 The schematic graphs of (a) the wedge mold casting and the location of compression and fatigue samples and (b) the geometry and dimension of the LCF and TMF fatigue samples. A central hole was machined only for the TMF sample.

The samples for compression tests were also taken from wedge-mold castings (Fig. 4.1a), and tests were conducted on the Gleeble 3800 thermomechanical simulator system using the T7- and T7A-treated samples (cylindrical with a diameter of 10 mm and height of 15 mm) under room temperature and 300 ℃ with a strain rate of 10^{-3} s^{-1}. The 0.2% offset yield strength (YS) was determined from the stress–strain curves. At least three samples were tested for each condition.

Microstructures of all experimental alloys under different states were observed using optical microscopy. A scanning electron microscope (SEM, JSM6480LV) equipped with an energy-dispersive X-ray spectroscopy (EDS) operated at 20 KV was used to identify the intermetallic phases and observe the fracture morphology after fatigue tests. The precipitates were characterized after different heat treatments and fatigue tests were conducted with a transmission electron microscope (TEM, JEM2100) operated at 200 KV. The TEM foils were initially punched to a diameter of 3 mm, followed by grinding to achieve a thickness ranging from 40 to 60 μm. Subsequently, a twin-jet electrochemical process was applied to the foils at a temperature of -20 ℃ and a voltage of 20 V. This process was conducted in a solution containing 200 mL of

methanol and 75 mL of nitric acid. The parameters of the precipitates (e.g., thickness, length, and number density) were quantified using ImageJ based on the TEM images. A minimum of 1000 precipitates were quantified for each alloy and condition, and the average value was obtained. Further details regarding the quantification method can be found in Refs. [6, 41].

4.3 Results

4.3.1 Microstructure and mechanical properties

The microstructures of the experimental alloys in the as-cast, T7, and T7A states were observed; all alloys displayed similar microstructures despite the different Mg contents. The typical microstructures of the 0.12Mg alloy are shown in Fig. 4.2. The as-cast structure comprised fine equiaxed grains with an average grain size of approximately 40 μm [6]; the microstructure comprises Al dendrite cells/grains, primary intermetallic Al_2Cu, $Al_7Cu_2(Fe,Mn)$, and $Al_3(Ti,Zr,V)$, as shown in Fig. 4.2(a). The primary Al_2Cu and $Al_7Cu_2(Fe, Mn)$ intermetallic phases were distributed at dendrite boundaries, whereas $Al_3(Ti,Zr,V)$ intermetallic particles were distributed randomly in the Al matrix. After the T7 heat treatment, most primary Al_2Cu was dissolved in the matrix, whereas the intermetallic $Al_7Cu_2(Fe,Mn)$ and $Al_3(Ti,Zr,V)$ barely changed (Fig. 4.2b). After further thermal exposure at 300 °C for 100 h (T7A), the intermetallic $Al_7Cu_2(Fe,Mn)$ and $Al_3(Ti,Zr,V)$ stays almost the same, as shown in Fig. 4.2(c). All intermetallic phases were identified based on the SEM-EDS results and from existing literature [4-7].

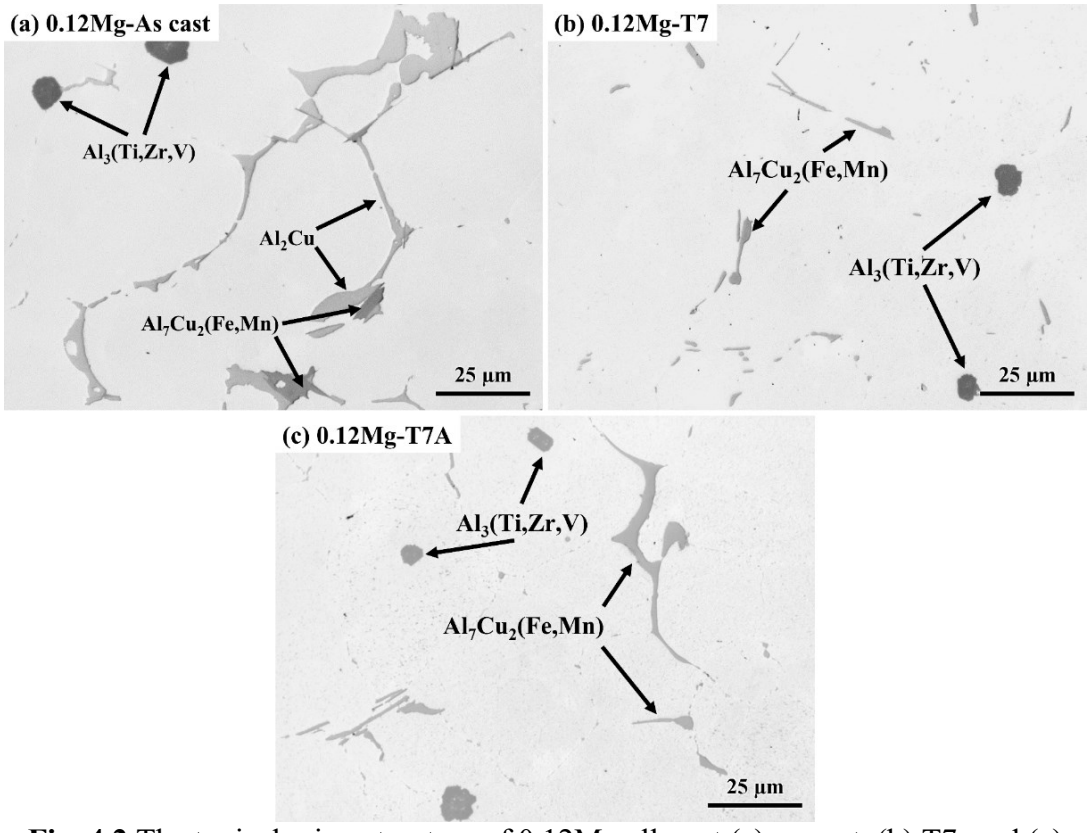

Fig. 4.2 The typical microstructure of 0.12Mg alloy at (a) as-cast, (b) T7, and (c) T7A states.

The evolution of precipitates during heat treatment was observed using TEM. The typical bright-field TEM images viewed along $<001>_{\alpha\text{-Al}}$ are shown in Fig. 4.3. After the T7 treatment, the dominant strengthening precipitates in the 0Mg alloy are θ″ (Fig. 4.3a), which is confirmed by the selected area diffraction pattern (SADP) shown in the inset of Fig. 4.3a. With the addition of Mg, mixed θ″ and θ′ are observed in the 0.12Mg and 0.24Mg alloys, as shown in Fig. 4.3b and c. The addition of Mg promoted the precipitation of θ′, which led to a higher number density in the Mg-containing alloys. After T7A treatment, the dominant precipitates in all experimental alloys transferred into θ′, as shown in Fig. 4.3d-f. Finer and denser distributions of θ′ were found in the Mg-containing alloys. Adding Mg can enhance the coarsening resistance of θ′ and promote the thermal stability of Al-Cu alloys during thermal

exposure at 300 °C. The mechanisms have been discussed in our previous works [4, 6].

It is to mention that the addition of Mg did induce a trace amount of cubic σ-Al5Cu6Mg2 precipitates after T7 treatment. Its influence in Mg-containing alloys was found to be negligible due to its limited quantity, and therefore, this particular precipitate was not discussed in the following sections. Further elaboration on this precipitate can be found in references [42, 43].

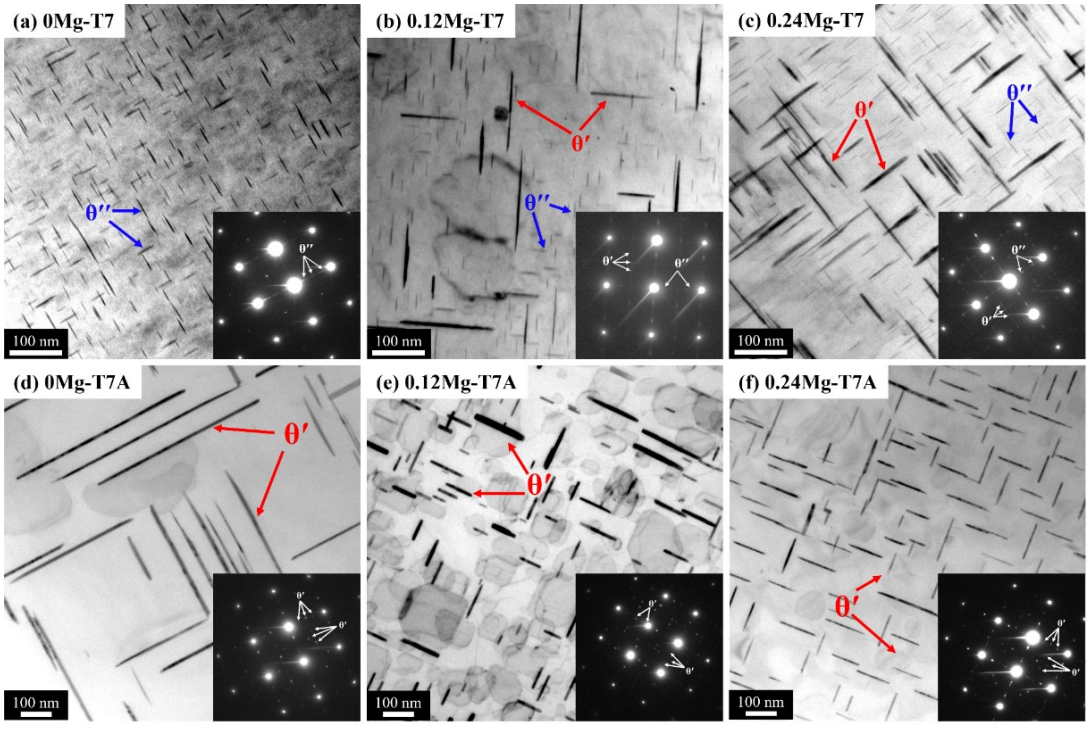

Fig. 4.3 Bright-field TEM images of all the experimental alloys (a-c) at T7 state and (d-f) at T7A state viewed along <001>$_{\alpha\text{-Al}}$. The corresponding SADP is shown in the inset of each image.

For the mechanical properties of the experimental alloys after T7 and T7A treatments, compression tests were performed at both room temperature and 300 °C, and the results of the yield strengths (YS) are shown in Fig. 4.4. Under the T7 state, YSs at both room temperature and 300 °C increased with an increase in Mg content.

The YSs of the 0.24Mg alloy reached the highest ones, and they increased by 23% at room temperature and by 25% at 300 ℃, respectively, compared with those of the 0Mg alloy. After T7A thermal exposure, all alloys experienced softening, and the YSs were remarkably reduced relative to the T7 state. However, Mg-containing alloys still exhibited higher YS at both room temperature and 300 ℃. The YS improved from 197 MPa in the 0Mg alloy to 212 MPa in the 0.12Mg alloy and to 256 MPa in the 0.24Mg alloy at room temperature. YS increased from 122 MPa in the 0Mg alloy to 132 MPa in the 0.12Mg alloy and to 142 MPa in the 0.24Mg alloy at 300 ℃, representing an improvement of 30% at room temperature and 16% at 300 ℃, respectively. The addition of Mg can affect the size and distribution of θ′ strengthening phase and improve their thermal stability during elevated-temperature exposure (Fig. 4.3d-f). Therefore, a finer and denser θ′ in Mg-containing alloys contributes to higher mechanical properties at both room and elevated temperatures. However, the enhanced YS provided by the addition of Mg decreased alloy ductility. A previous study [4] found that the elongation of the Al-Cu 224 alloy at room temperature decreased from ~15% in the 0Mg alloy to ~2% in the 0.24Mg alloy. At high temperature (300 ℃), all experimental alloys showed relatively high ductility (elongation > 12%); further, at this temperature, they were not affected by Mg addition [4].

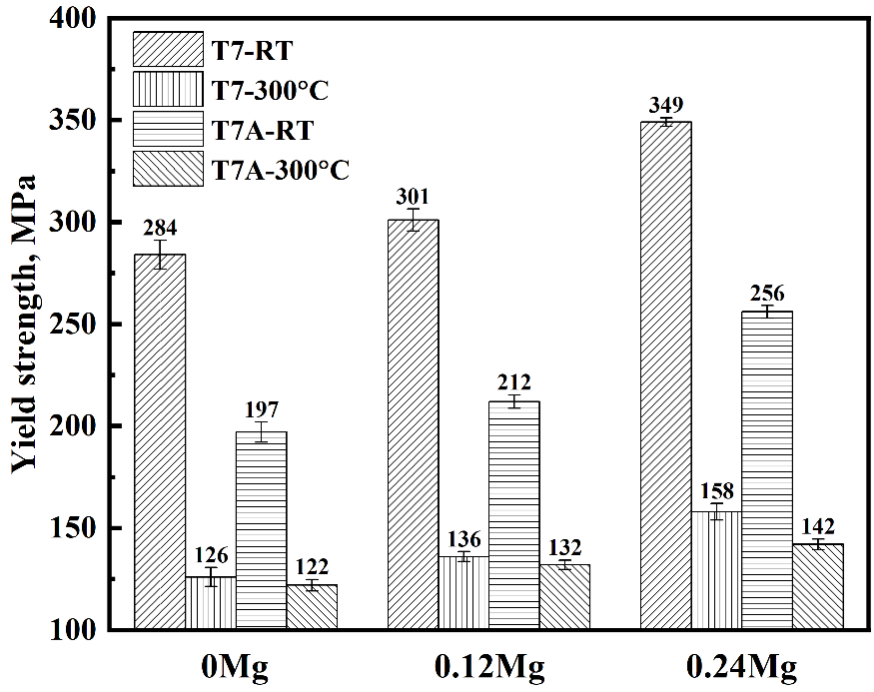

Fig. 4.4 The yield strengths of the alloys tested at room temperature and 300 ℃ at different states.

4.3.2 Cyclic stress–strain response under LCF and TMF

Fig. 4.5 shows the typical cyclic stress–strain responses of all tested alloys under LCF loading at strain amplitudes from 0.2% to 0.6% and at 300 ℃. Under the LCF regime, the shape of the mid-life hysteresis loops in all alloys was close to a parallelogram. As revealed by the hysteresis loops, tensile and compressive stresses were nearly symmetrical at different strain amplitudes in the experimental alloys. The maximum stress and plastic strain (the value of the plastic strain was equal to the width at the center of the loop) obtained from the midlife hysteresis loops are summarized in Table 4.2. The maximum stress, plastic strain, and hysteresis loop areas increased significantly with an increasing strain amplitude for all tested alloys. Using the 0Mg alloy as an example, the midlife maximum tensile stress and plastic strain increased from 84 MPa and 0.07% at a strain amplitude of 0.2 % to 98 MPa and 0.44% at a strain

amplitude of 0.6%, respectively. Under the same strain amplitude, the maximum tensile stress increased, whereas the plastic strain decreased with an increase in the Mg content (Figs. 4.5 (a–c) and Table 4.2). For example, at 0.6% strain amplitude, the maximum tensile stress increased from 98 MPa in the 0Mg alloy to 127 MPa in the 0.24Mg alloy, whereas the plastic strain decreased from 0.44% to 0.39%. Fig. 4.5(d-f) shows the maximum and minimum stress response curves, respectively. For a given alloy, the maximum and minimum stresses increased with increasing strain amplitude. The maximum and minimum stresses increased with increasing Mg content at the same strain amplitude. During cyclic loading, significant cyclic softening occurred in the initial stage, and the cyclic stress remained almost stable for a majority of the fatigue life at a low strain amplitude (~0.2%). However, the softening was continuous at higher strain amplitudes (0.4% and 0.6%).

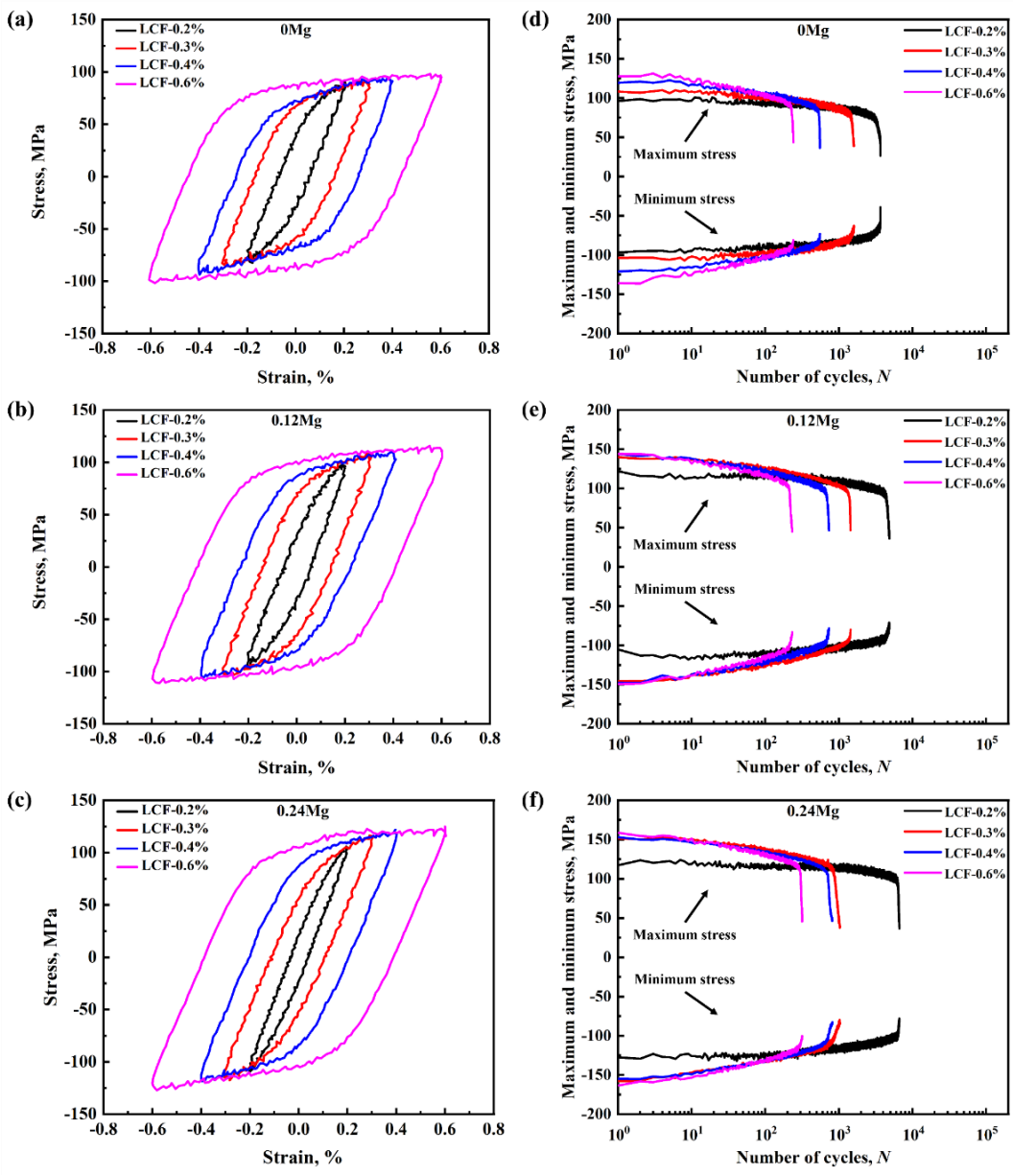

Fig. 4.5 Mid-life hysteresis loops (a-c) and the maximum and minimum stress response curves (d-f) at different strain amplitudes under LCF loading.

Fig. 4.6 shows the typical cyclic stress–strain responses in TMF tests at strain amplitudes of 0.2–0.6%. Under TMF loading, mid-life hysteresis loops were asymmetrical at all strain amplitudes where tensile portions were larger than the compression portions. Further, tensile stress was significantly higher than the compression stress, which is a common phenomenon of out-of-phase TMF reported in the literature [44, 45]. During TMF cycling, the maximum tensile stress at the lowest

temperature (60 ℃) was always higher than the maximum compressive stress at the highest temperature (300 ℃) because the alloy strength was higher at low temperatures than that at high temperatures. As shown in Fig. 4.6(a-c) and Table 4.2, the maximum stress and plastic strain increased with increasing strain amplitude for all tested alloys. The Mg-containing alloys exhibited a higher peak tensile stress and lower plastic strain than the 0Mg alloy under the same strain amplitude. The maximum tensile stress increased with increasing Mg content, whereas the plastic strain decreased. Fig. 4.6(d)–(f) show the maximum tensile and compressive stresses of experimental alloys as functions of fatigue cycles under various strain amplitudes. All tested alloys experienced cyclic softening during TMF.

Compared with that for LCF, the maximum tensile stress was considerably higher in the TMF of the experimental alloys. For example, the maximum tensile stress of the 0Mg alloy at a 0.3% strain amplitude under LCF loading was 90 MPa, which is considerably lower than the 166 MPa under TMF loading. In contrast, the plastic strain in TMF was slightly lower than that in LCF (Table 4.2).

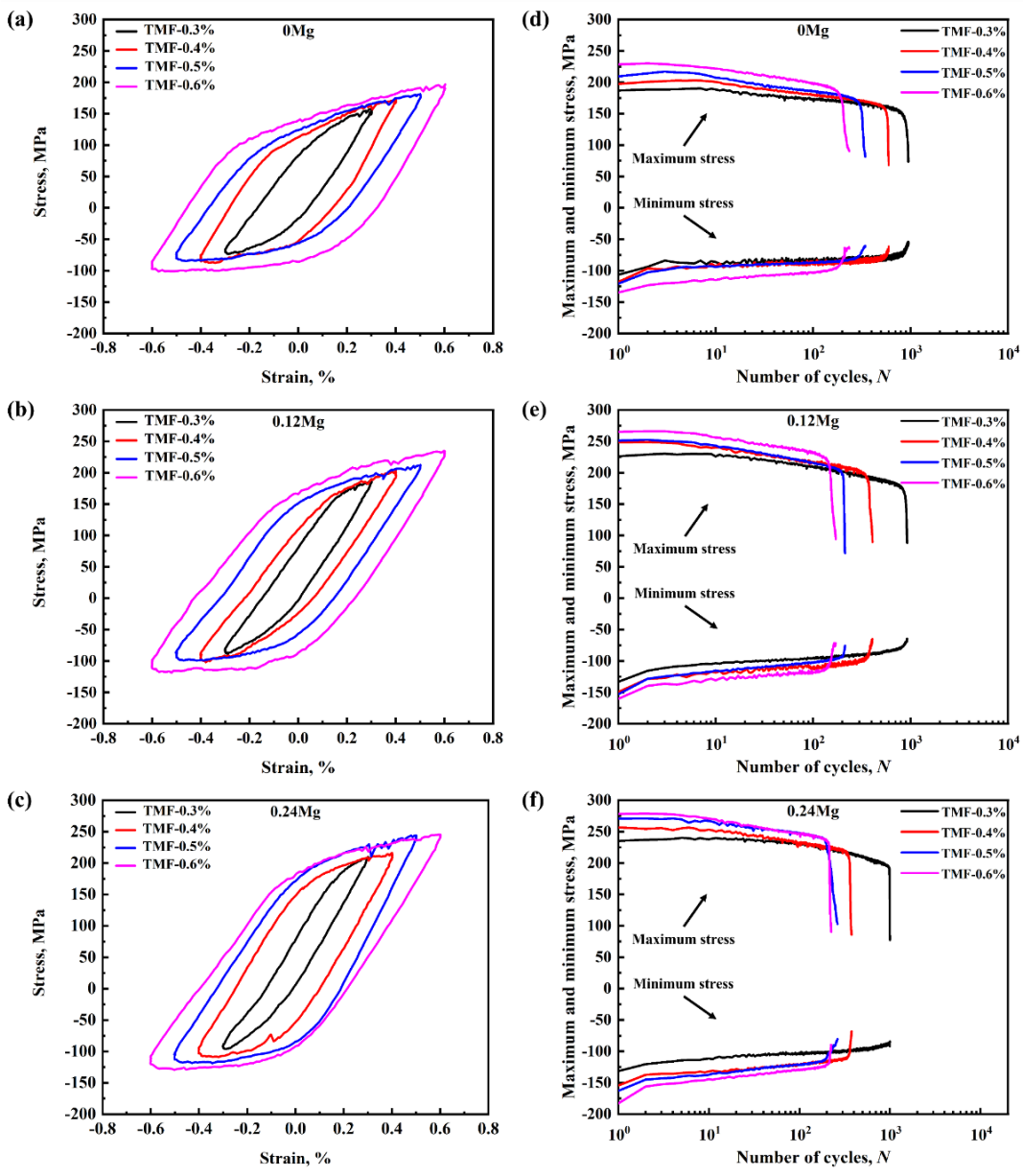

Fig. 4.6 Mid-life hysteresis loops (a-c) and the maximum and minimum stresses response curves (d-f) at different strain amplitudes under TMF loading.

Table 4.2 The parameters obtained from stress-strain curves at mid-life cycle under both LCF and TMF regimes.

Parameter	Regime	Alloy	Strain amplitude, %				
			0.2	0.3	0.4	0.5	0.6
Maximum tensile stress, MPa	LCF	0Mg	84±1.4	90±1.5	96±1.6	-	98±0.7
		0.12Mg	100±1.7	109±0.5	110±0.5	-	115±1.6
		0.24Mg	107±2.0	119±4.2	123±4.6	-	127±2.7
	TMF	0Mg	-	166±2.2	172±7.5	177±5.4	192±7.5
		0.12Mg	-	197±10.1	207±3.9	214±2.0	235±2.6
		0.24Mg	-	210±0.6	221±7.2	244±0.4	246±3.2
Plastic strain, %	LCF	0Mg	0.07 ±0.013	0.17 ±0.006	0.25 ±0.005	-	0.44 ±0.004
		0.12Mg	0.05 ±0.013	0.13 ±0.012	0.23 ±0.002	-	0.41 ±0.005
		0.24Mg	0.03 ±0.005	0.11 ±0.039	0.21 ±0.001	-	0.39 ±0.001
	TMF	0Mg	-	0.14 ±0.007	0.20 ±0.05	0.31 ±0.016	0.40 ±0.008
		0.12Mg	-	0.11 ±0.002	0.18 ±0.007	0.25 ±0.013	0.36 ±0.006
		0.24Mg	-	0.08 ±0.007	0.16 ±0.022	0.24 ±0.003	0.32 ±0.001

A softening ratio was introduced to evaluate the softening during the fatigue process under different conditions. This ratio is expressed as [46, 47]:

$$SR = \frac{\Delta\sigma_{max} - \Delta\sigma_{half}}{\Delta\sigma_{max}} \quad (4.3)$$

where $\Delta\sigma_{max}$ and $\Delta\sigma_{half}$ represent the maximum stress amplitude and the stress amplitude at the half lifetime, respectively.

The results are presented in Fig. 4.7. For the LCF, the softening ratio increased to the maximum value at a strain amplitude of 0.3% and then gradually decreased with increasing strain amplitude with an increase in strain amplitude. The 0.24Mg alloy exhibited a lower softening ratio, indicating better thermal stability. Further, the difference in the softening ratios among all experimental alloys decreased with an increase in the strain amplitude. For the TMF, the softening ratios of all alloys showed a decreasing trend with an increase in the strain amplitude. However, the Mg-containing alloys (particularly the 0.24 Mg alloy) showed a lower softening ratio than the Mg-free alloy at a given strain amplitude. Considering the 0.4% strain amplitude as an example, the softening ratio in the 0.24Mg alloy reached the lowest value of 0.10, which is considerably lower than 0.16 for the 0.12Mg alloy and 0.18 for the 0Mg alloy. Therefore, Mg-containing alloys exhibited higher thermal stability in the TMF regime than the Mg-free alloy. The softening ratio during TMF was lower than that during LCF (Fig. 4.7).

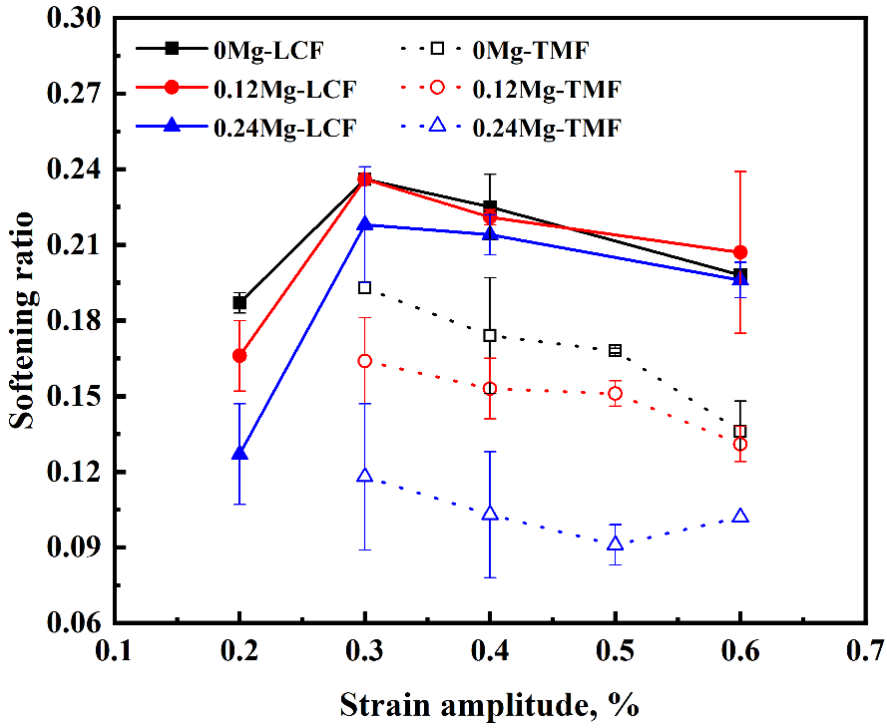

Fig. 4.7 The softening ratio vs. different strain amplitudes under LCF and TMF loadings.

4.3.3 LCF and TMF fatigue lifetimes

The fatigue lifetimes of all alloys under both LCF and TMF loadings are shown in Fig. 4.8. As shown in Fig. 4.8a and b, the fatigue lives of all alloys under LCF and TMF loadings decreased with increasing strain amplitude. Fatigue lives under LCF loading were longer than those under TMF loading at all strain amplitudes and for all alloys (Fig. 4.8c and d). For example, for the 0Mg alloy, the average number of cycles under LCF loading was 1387 at a 0.3% strain amplitude and 544 at a 0.4% strain amplitude, where the average number of cycles under TMF loading were 594 and 369 at 0.3% and 0.4% strain amplitudes. The TMF life of the 0Mg alloy ranged from 43% to 68% of the LCF life at 0.3% and 0.4% strain amplitudes. For the 0.24Mg alloy, the TMF lives were only 28% to 32% of the LCF lives at 0.3% and 0.4% strain amplitudes.

This difference in fatigue life decreased with an increase in the strain amplitude to 0.6%.

Under LCF loading, the fatigue lifetimes of the experimental alloys were improved by adding Mg. For example, at a strain amplitude of 0.2%, the average life increased from 4112 cycles for the 0Mg alloy to 4602 cycles for the 0.12Mg alloy and 6001 cycles for the 0.24Mg alloy (see Fig. 4.8c). With an increasing strain amplitude, the fatigue lifetimes of the 0Mg and 0.12Mg alloys were approximately the same; however, the 0.24Mg alloy always showed a longer fatigue life than the 0Mg alloy. Among the experimental alloys, the 0.24Mg alloy exhibited the longest elevated temperature LCF lifetimes.

In contrast, under TMF loading, the addition of Mg caused a slight reduction in the fatigue lifetime (Fig. 4.8d). The 0Mg alloy exhibited the longest TMF lifetime. At a strain amplitude of 0.3%, Mg showed a negligible effect on the number of TMF cycles. At higher strain amplitudes (0.4–0.6%), the addition of Mg slightly decreased the number of cycles. Compared with LCF loading, the difference in the TMF lifetime was smaller among the experimental alloys.

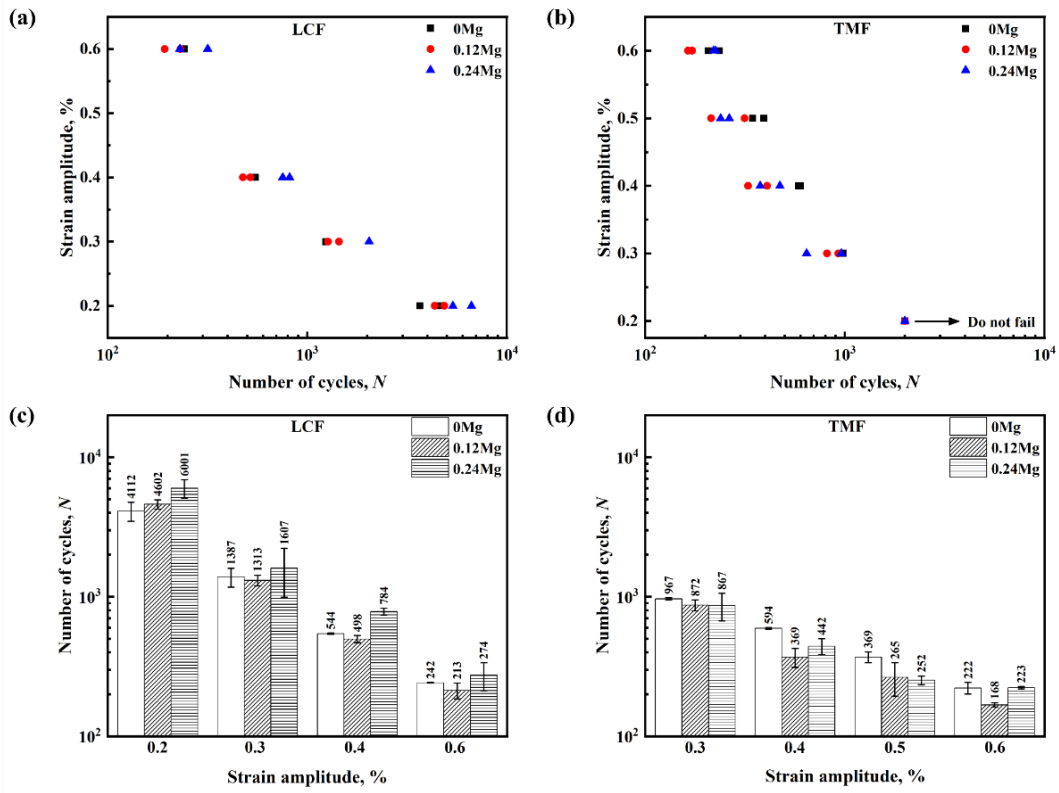

Fig. 4.8 Fatigue lifetimes of three alloys at various strain amplitudes under (a) LCF and (b) TMF loading, and the average number of cycles under (c) LCF and (d) TMF loadings.

4.3.4 Fracture analysis

Fracture surfaces were analyzed after the LCF and TMF tests. The results showed that all experimental alloys displayed similar fracture characteristics. The addition of Mg barely affected the fracture characteristics. An overview of the fracture morphology of the 0Mg alloy after LCF and TMF tests at strain amplitudes of 0.4% and 0.6% is shown in Fig. 4.9(a-d). The detailed characteristics of the fracture after LCF testing at a strain amplitude of 0.4% are shown in Fig. 4.9 (e–h). The crack initiation and propagation zones, as well as the instantaneous fracture zone, are marked in both the LCF- and TMF-tested samples (Figs. 4.9(a-d)). For both LCF and TMF, the fracture surfaces displayed mixed-rupture characteristics: quasi-cleavage in the

crack initiation and propagation zones, and dimples in the instantaneous fracture zone, as shown in Figs. 4.9(e-f). Under both LCF and TMF loadings, the cracks tended to initiate at multiple points. Near-surface pores were found to be the main crack-initiation sites, as shown in Fig. 4.9g. Further, brittle intermetallic particles Al_3(Ti,Zr,V) and Al_7Cu_2(Fe,Mn) ruptured during fatigue and acted as potential crack-initiation sites (Fig. 4.9h). During the fatigue process, cracks first appeared at multiple points near the sample surface and propagated through the matrix. After the maximum crack-tip stress intensity factor reached the fracture toughness of the alloy, overloading occurred at the critical crack length, which caused instantaneous rupture. Further, some cracks formed at pores and brittle intermetallic particles inside the sample. When the main crack propagates in the vicinity of the internal cracks, the main crack tip deflects and merges with these internal cracks, leading to the formation of steps, as shown in Fig. 4.9g.

Fracture surfaces showed that the area of the propagation zone decreased with increasing strain amplitudes; see the example of the 0Mg alloy at 0.4% and 0.6% strain amplitudes under both LCF and TMF (Fig. 4.9(a-d)). A higher fatigue life indicates a larger propagation zone. Compared to LCF samples, the area fraction of the propagation zone after the TMF test was smaller, particularly at a low strain amplitude. Considering the 0.4% strain amplitude as an example, the area fraction of the propagation zone under LCF loading was greater than 50%, whereas it was less than 40% under TMF loading (see Fig. 4.9a and c). The smaller area fraction in the TMF samples was attributed to higher tensile stress and lower ductility when cyclic temperature was switched to lower temperature during the fatigue cycle. Further, the

force-bearing area was smaller in the TMF sample than in the LCF sample because of the air holes in the TMF sample. Some crack-propagation zones penetrate the surface of the air holes. Furthermore, it was observed that cracks could start from the surface defects of the air hole, as shown in Fig. 4.9c.

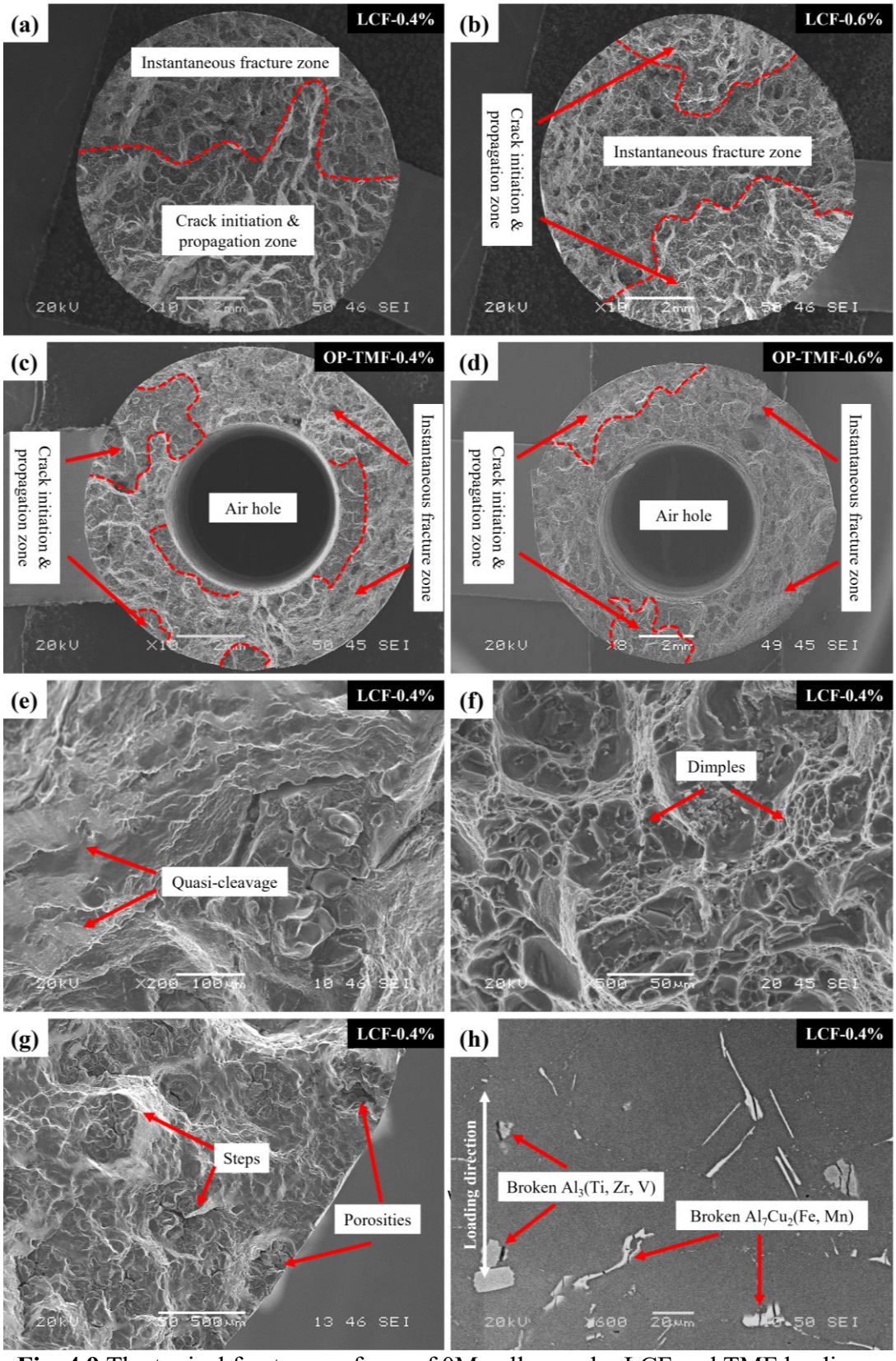

Fig. 4.9 The typical fracture surfaces of 0Mg alloy under LCF and TMF loadings.

4.4 Discussion

4.4.1 Effect of Mg addition on fatigue behavior

Adding Mg to the Al-Cu 224 alloy under high-temperature LCF loading enhances the LCF fatigue performance, as shown in Fig. 4.8(a) and (c). The crack initiation sites for all tested samples with different Mg contents were similar, consisting of pores and broken intermetallic particles, Al_3(Ti,Zr,V) and Al_7Cu_2(Fe,Mn). In addition, the ductility values of all experimental alloys at 300 ℃ were relatively high and unaffected by the Mg additions [4]. Therefore, interactions between the precipitates and dislocations and the thermal stability of the strengthening precipitates are considered the main factors influencing the high-temperature LCF behavior. Previous studies reported that a combination of shearable and nonshearable strengthening precipitates was beneficial for improving fatigue behavior [23, 48-50]. After T7 heat treatment, the dominant precipitates in 0Mg alloy were coherent θ″ (shearable) showing a low strength (Fig. 4.3a), while a mixture of coherent θ″ and semi-coherent θ′ (non-shearable) was found in Mg-containing alloys with high strength (Fig. 4.3b and c). The combination of the θ″ and θ′ in Mg-containing alloys enhances their LCF behavior.

Under LCF cyclic loading at 300 °C, all shearable θ″ precipitates transformed into θ′ phase and underwent substantial coarsening, characterized by an increase in size and a decrease in number density. As the consequence, the material exhibited significant softening behavior. After crack initiation, plastic deformation occurs around the crack tip due to stress concentration. Precipitates in the matrix enhance the material's strength by obstructing dislocation movement, as well as acting as barriers against

crack propagation. Fig. 4.10 depicts a representative weak-beam TEM image of 0.12Mg alloy subjected to a 0.4%-LCF test. This image demonstrates a complex interaction between precipitates and dislocations. Notably, a substantial number of dislocations (marked by white arrows) were observed to be blocked owing to their interaction with θ′ precipitates (marked by red arrows). However, as the precipitates coarsen, their effectiveness in hindering dislocation motion and crack propagation diminishes, making crack propagation easier. Ultimately, failure occurs when the softened materials caused by precipitate coarsening cannot adequately support the plastic zone at the crack tips. Hence, the thermal stability of the θ′ precipitates is considered another main factor determining fatigue behavior during the isothermal LCF at an elevated temperature. The TEM images and compressive test (Figs. 4.3 and 4.4) results indicate that Mg-containing alloys display a finer and denser distribution of θ′ precipitates and a higher yield strength after thermal exposure at 300 °C (T7A) relative to the base 0Mg alloy. In this study, the 0.6% strain-tested samples were selected for comparing the thermal stability of θ′ precipitates during both LCF and TMF because of their similar number of cycles. Fig. 4.11 shows the bright-field TEM images of the three alloys after LCF and TMF; the quantitative results of the precipitates are summarized in Table 4.3. After high-temperature LCF, dominant precipitates were θ′ in all experimental alloys, as confirmed by SADP (not shown here). As revealed in our prior investigation [4], the Mg addition accelerated and promoted the precipitation of θ′ during the ageing process. This led to a transformation in the dominant precipitates, shifting from θ″ in the Mg-free alloy to θ′ in the Mg-containing alloys. The θ″ phases with low thermal resistance in Mg-free alloys undergo rapid dissolution at elevated temperatures, thereby providing sufficient solutes for the

subsequent lateral and ledge growth of θ′ precipitates. In contrast, Mg-containing alloys exhibit limited lateral and ledge growth of θ′ due to their lower quantity of θ″ phases and relatively higher thermal stability of θ′. Consequently, finer and denser θ′ precipitates were observed in Mg-containing alloys after high-temperature LCF. For example, the length of θ′ in the 0.24Mg alloy was only half of that in the 0Mg alloy, whereas the number density of θ′ in the 0.24Mg alloy was five times higher than that in the 0Mg alloy. The higher thermal resistance of θ′ precipitates enhanced by Mg addition improved the LCF behavior at elevated temperatures. In brief, the co-existence of θ′ (dominant) and θ″ in the initial microstructure and the high thermal stability of θ′ precipitates during LCF in Mg-containing alloys result in improved LCF performance.

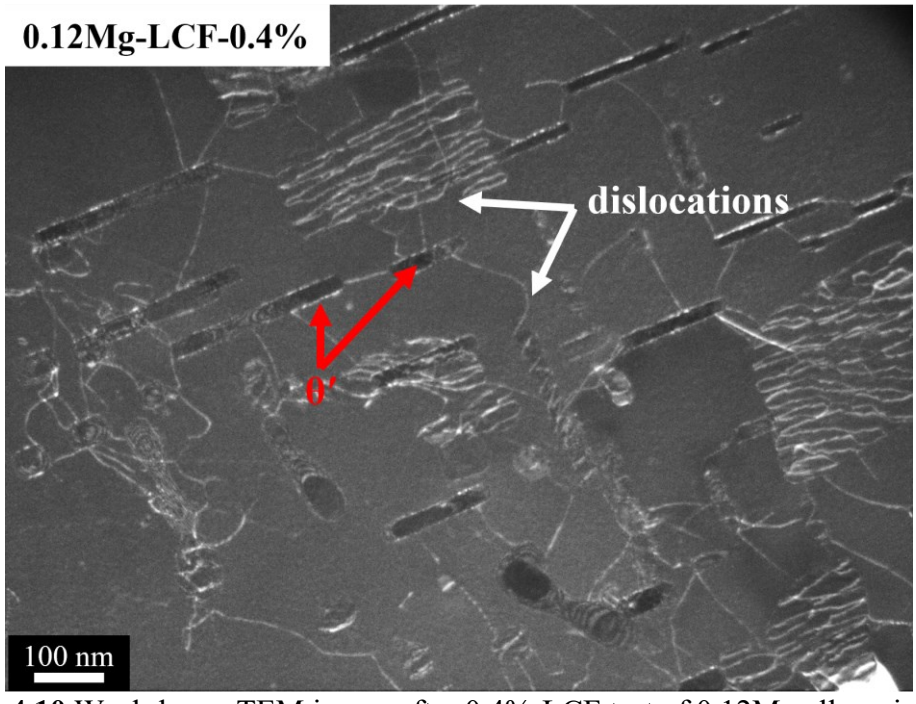

Fig. 4.10 Weak-beam TEM image after 0.4%-LCF test of 0.12Mg alloy viewed along <001>$_{\alpha\text{-Al}}$ demonstrating a complex interaction between dislocations and θ′ precipitates. The dislocations and θ′ are marked by the white and red arrows, respectively.

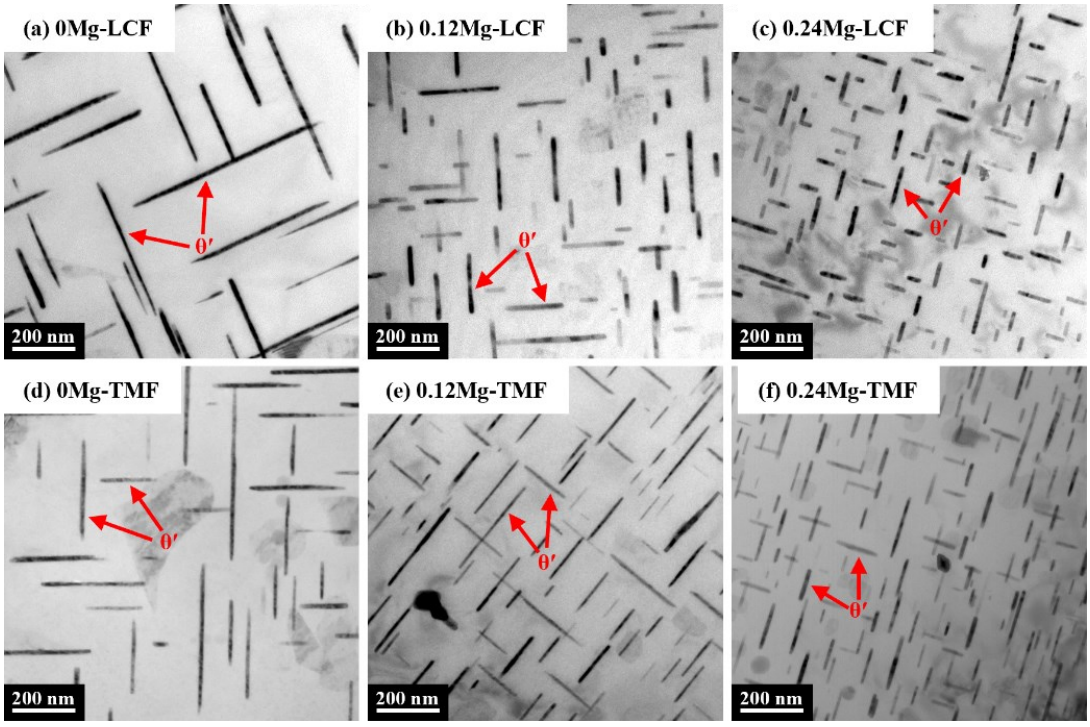

Fig. 4.11 Bright-field TEM images viewed along <001>$_{\alpha\text{-Al}}$ of all experimental alloys after LCF and OP-TMF tests at the 0.6% strain amplitude.

In the TMF regime, the addition of Mg slightly weakens the fatigue performance, as shown in Fig. 4.8b and d. During the TMF process, plastic deformation occurring at the maximum temperature does not cause fatigue cracking because of the compression state; however, the maximum mechanical strain obtained at the minimum temperature favors crack initiation and propagation because of the tensile state. Therefore, in strain-controlled TMF tests, the high ductility of the material can delay crack propagation and prolong fatigue life [51, 52]. As reported in a previous study [4], the addition of Mg caused a significant reduction in the ductility of the Al-Cu 224 alloy at room temperature, and this directly affected the TMF performance of Mg-containing alloys. The main strengthening phase θ′ in all experimental alloys experienced coarsening during TMF; however, the extent is less than that of the isothermal LCF because of the lower lifetime. As shown in Fig. 4.11(d-f) and Table 4.3, the Mg-containing alloys had a finer and denser distribution of θ′ precipitates than

the base 0Mg alloy after TMF. Consequently, the poor thermal stability of the 0Mg alloy resulted in higher strength degradation, facilitating plastic deformation and deteriorating the crack propagation resistance. In contrast, the higher thermal stability of θ′ in Mg-containing alloys enhanced crack propagation resistance and compensated for the poor TMF performance caused by low ductility. The TMF behavior in Al-Cu 224 alloys was determined by the alloy ductility and thermal stability of θ′ precipitates. Under the combination of these two counter factors, the effect of Mg addition on TMF performance was not strong.

Table 4.3 Quantitative results of θ″ and θ′ of experimental alloys at different states.

Alloy	State	Precipitates	Length, nm	Thickness, nm	Number density, nm^{-3}
0Mg	T7	θ″	31.0±10.8	3.3±0.8	1.3×10^{-5}
	LCF-0.6%	θ′	213.0±115.3	20.7±5.2	6.4×10^{-8}
	TMF-0.6%	θ′	170.1±89.9	16.7±4.0	8.2×10^{-8}
0.12Mg	T7	θ′	102.7±43.3	5.3±1.8	2.9×10^{-7}
		θ″	32.2±13.0	2.9±0.8	7.6×10^{-6}
	LCF-0.6%	θ′	120.7±63.8	18.9±3.9	2.1×10^{-7}
	TMF-0.6%	θ′	132.3±58.6	11.4±3.2	2.3×10^{-7}
0.24Mg	T7	θ′	87.6±35.0	5.4±1.6	1.1×10^{-6}
		θ″	32.1±12.8	3.1±0.8	3.4×10^{-6}
	LCF-0.6%	θ′	101.5±49.4	16.5±3.1	3.3×10^{-7}
	TMF-0.6%	θ′	79.5±34.1	11.2±2.8	9.5×10^{-7}

Fig. 4.8 reveals that the lifetime under TMF loading is shorter than the LCF lifetime at a given strain amplitude, particularly at low strain amplitudes. There are several possible explanations for this observation. First, OP-TMF has a phase angle (phasing between the applied strain and temperature) of –180° compared with that of isothermal LCF, and this leads to a considerably higher maximum tensile stress during TMF, as shown in Figs. 4.5−4.6 and Table 4.2. The higher tensile stress and lower ductility at low temperatures facilitated plastic deformation and crack initiation in the TMF regime, accelerating crack propagation and leading to a shorter fatigue lifetime relative to isothermal LCF. In addition, TMF loading is far more damaging than isothermal LCF loading because of the combined damage effect of the cyclic mechanical and thermal loadings [24, 53]. Hence, TMF loading has a shorter fatigue lifetime than that for isothermal LCF loading.

4.4.2 Fatigue life prediction

As mentioned in the Introduction, the classical plastic strain-based Coffin–Manson model is used for uniaxial isothermal LCF tests [26, 27]. However, there are several disadvantages to using this model for LCF life prediction at elevated temperatures. (1) The precipitation-strengthened Al-Cu alloy displayed cyclic softening during high-temperature LCF because of the gradual coarsening of the θ′ strengthening phase. (2) the Coffin–Manson model does not consider the influence of the changing stress caused by cyclic softening on fatigue behavior [28, 54]. (3) In terms of the TMF, the introduced cyclic temperature makes the Coffin–Manson model unsuitable for estimating the fatigue life [31, 32]. To predict fatigue life, an energy model based on hysteresis energy was used in this study, which has been successfully

applied to both the LCF [28, 54] and TMF [32, 55] regimes of aluminum alloys. The hysteresis energy model shares an accumulating damage form given by [46, 56, 57]:

$$D_i = \left(\frac{w_i}{w_o}\right)^{\beta} \tag{4.4}$$

$$D = \sum_{i=1}^{N_f} D_i = \sum_{i=1}^{N_f} \left(\frac{w_i}{w_o}\right)^{\beta} = 1 \tag{4.5}$$

where D_i and W_i represent the damage parameter and hysteresis energy of the ith cycle, respectively. W_o represents the intrinsic fatigue damage capacity, N_f represents the number of the fatigue cycle, and β represents the fatigue damage exponent; N_f and β are the material constants. W_o represents the fatigue damage capacity of the tested alloy; a higher value indicates a higher resistance to fatigue damage of the materials. Further, β represents the ability to transform mechanical work into effective damage to the materials; an increase in β indicates the improved ability for damage diminishment.

For practical uses of the model, hysteresis energy W_i can be substituted by a constant value of the saturation hysteresis energy W_s because it is usually stabilized just after the initial few cycles and is saturated during most of the fatigue cycle [28, 45]. Therefore, W_s is easily obtained from the fatigue data after several initial cycles or at half-lifetime (Figs. 4.5 and 4.6) at all applied strain amplitudes; its value equals the area of the hysteresis loop. Then, Eq. 4.5 can be simplified as:

$$D = N_f \cdot \left(\frac{w_s}{w_o}\right)^{\beta} = 1 \tag{4.6}$$

Equation 4.6 can be transformed into a form similar to the Basquin and Coffion–Manson laws, with $D = 1$.

$$w_s = w_o \cdot N_f^{-\frac{1}{\beta}} \tag{4.7}$$

Based on the fatigue hysteresis data and experimental fatigue lives in LCF and TMF, W_s as a function of N_f is shown in Fig. 4.12a and b on a log-log scale. The material constants W_o and β can be calculated from the logW_s–logN_f relationship, and the results for both the LCF and TMF are listed in Table 4.4. Under the LCF regime, the value of β (the slopes of the fitting curves, Fig. 4.12a) is similar for all tested alloys, whereas the value of W_o (fatigue damage capacity) increases from 89 to 171 MJ/m^3 with an increase in the Mg content from 0 to 0.24 wt.%. A larger value of W_o in Mg-containing alloys indicates a higher LCF resistance. In the TMF regime, β displayed no significant difference among the tested alloys, whereas the 0Mg alloy showed a larger value of W_o than the Mg-containing alloys, indicating better TMF resistance. For Mg-containing alloys, a relatively lower value of W_o in the 0.12Mg alloy compared to that in the 0.24Mg alloy was attributed to the countereffect between ductility and thermal resistance.

Table 4.4 Materials parameters calculated with the energy model for fatigue life prediction.

	LCF		TMF	
	W_o (MJ/m^3)	β	W_o (MJ/m^3)	β
0Mg	89	1.35	457	0.99
0.12Mg	100	1.31	275	1.03
0.24Mg	171	1.22	347	1.00

The predicted fatigue lifetimes were calculated using Eq. 4.7. The material constants are listed in Table 4.4. Comparisons of the predicted and experimental TMF lifetimes of all tested alloys under both LCF and TMF are shown in Fig. 4.12c and d. The life prediction factor (LPF), which is defined as the ratio of the predicted life to the experimental life, is used to assess the accuracy of fatigue life prediction; the LPF is often used to evaluate the deviation in fatigue lifetime between the predicted and experimental values [55]. The values of LPF under LCF and TMF (dashed lines in Figs. 4.12c and d) were considerably low at 1.2, indicating that the predicted fatigue lifetimes agreed well with the experimentally measured values for all three alloys tested under both LCF and TMF. The results demonstrate that the hysteresis energy model is applicable for predicting the LCF and TMF lifetimes of Al-Cu alloys.

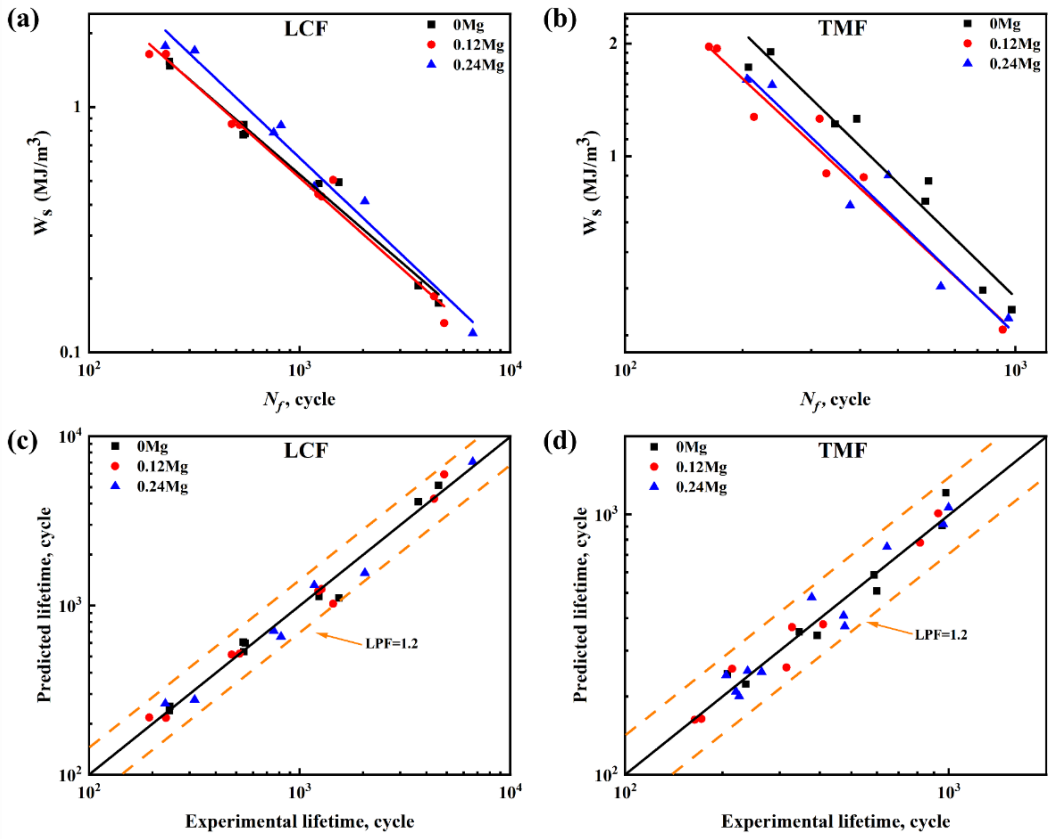

Fig. 4.12 Hysteresis energy W_s as a function of the fatigue cycle N_f in three alloys: (a) for LCF and (b) for TMF; and comparisons of the predicted and experimental fatigue lifetimes of all tested alloys, (c) for LCF and d) for TMF.

From the viewpoint of mechanical testing, conducting a TMF test is more time consuming than performing an LCF test. In addition, more attention is required to control the thermal strain precisely during the TMF process. A previous study [55] found that it is possible to use W_o and β determined by the LCF tests to predict the TMF lifetime. During TMF testing, the hysteresis energy can reach the saturation stage after only a few cycles [45, 55]; therefore, W_s can be determined after several initial cycles (e.g., 10 cycles) without conducting the TMF test until the end [45]. In this study, an approach was explored in which TMF lives at various strain amplitudes were predicted using W_o and β obtained from the LCF results. The predicted values were compared with the experimental TMF lives, as shown in Fig. 4.13. The results show

that this prediction has an LPF of 2.3, which is larger than the prediction using its own TMF material parameters, but it still exhibits reasonable accuracy. The predicted TMF lifetimes were overestimated to a certain extent because most data in Fig. 4.13 were above the diagonal baseline. The results shown in Fig. 4.13 confirm that it is still feasible to use material parameters obtained from LCF tests for predicting the TMF lifetime with less accuracy.

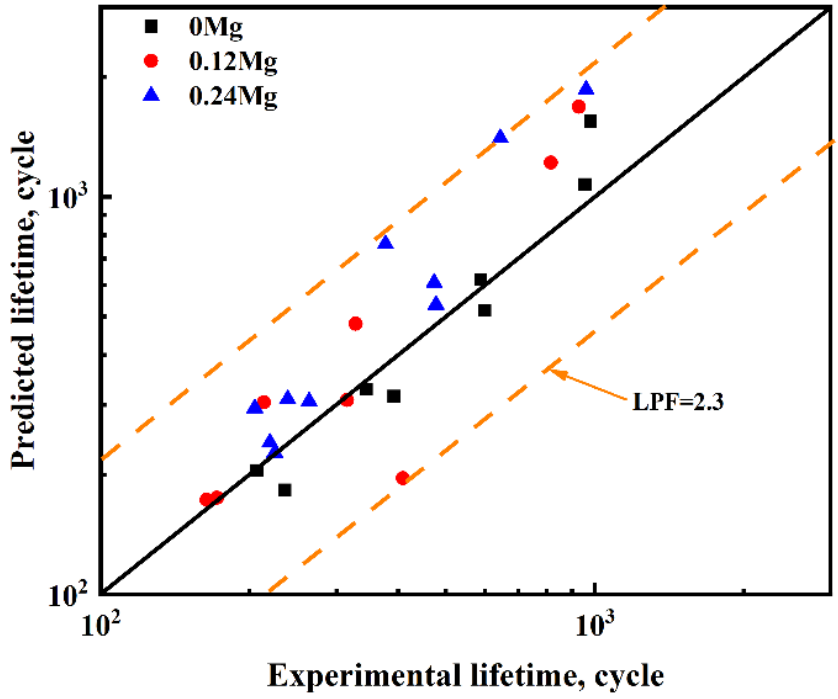

Fig. 4.13 Comparison of the fatigue lives predicted using the material parameters from LCF tests with the experimental TMF lives.

4.5 Conclusions

The cyclic deformation and fatigue life behaviors of Al-Cu 224 cast alloys were investigated under isothermal LCF at 300 °C and OP-TMF in the temperature range of 60–300 °C. The effects of Mg addition on the fatigue performances of both LCF and

TMF was studied, and a hysteresis energy model was applied to predict fatigue life. According to the results, main conclusions can be drawn as follows:

1) Under both LCF and TMF loadings, all tested Al-Cu alloys experienced cyclic softening; however, the softening ratio of Mg-containing alloys was lower than that of the base alloy free of Mg because of the lower coarsening rate and higher thermal stability of θ'-Al_2Cu precipitates in Mg-containing alloys.

2) The fatigue lives of Al-Cu alloys for both LCF and TMF decreased with an increase in the strain amplitude. The TMF lifetimes were inferior to LCF lifetimes under the same strain amplitude, especially at low strain amplitudes. However, the fatigue life difference between LCF and OP-TMF decreases with an increasing strain amplitude.

3) Under the LCF regime, the addition of Mg enhanced the fatigue performance of Al-Cu alloys because of the co-existing θ″ and θ′ precipitates and the higher thermal stability in Mg-containing alloys. The alloy with 0.24 wt.% Mg exhibited the highest fatigue resistance and longest LCF life.

4) In the TMF regime, Mg addition resulted in a slight reduction in the fatigue performance because of the lower ductility and high tensile stress of Mg-containing alloys at low temperatures.

5) The hysteresis energy model was applicable for predicting the LCF and TMF lifetimes of Al-Cu alloys with relatively high accuracy.

References

[1] S. Roy, L. F. Allard, A. Rodriguez, T. R. Watkins & A. Shyam, Comparative evaluation of cast aluminum alloys for automotive cylinder heads: part I—microstructure evolution, Metall. Mater. Trans. A 48.5 (2017): 2529-2542. https://doi.org/10.1007/s11661-017-3985-1

[2] M. Javidani & D. Larouche, Application of cast Al–Si alloys in internal combustion engine components, Int. Mater. Rev. 59.3 (2014): 132-158. https://doi.org/10.1179/1743280413Y.0000000027

[3] European Aluminium Association, The aluminium automotive manual, Join. Dissim. Mater. (2015): 1-31.

[4] J. Rakhmonov, K. Liu, L. Pan, F. Breton & X. G. Chen, Enhanced mechanical properties of high-temperature-resistant Al–Cu cast alloy by microalloying with Mg, J. Alloys Compd. 827 (2020): 154305. https://doi.org/10.1016/j.jallcom.2020.154305

[5] D. Li, K. Liu, J. Rakhmonov & X. G. Chen, Enhanced thermal stability of precipitates and elevated-temperature properties via microalloying with transition metals (Zr, V and Sc) in Al–Cu 224 cast alloys, Mater. Sci. Eng. A 827 (2021): 142090. https://doi.org/10.1016/j.msea.2021.142090

[6] P. Hu, K. Liu, L. Pan & X. G. Chen, Effect of Mg microalloying on elevated-temperature creep resistance of Al–Cu 224 cast alloys, Mater. Sci. Eng. A 851 (2022): 143649. https://doi.org/10.1016/j.msea.2022.143649

[7] P. Hu, K. Liu, L. Pan & X. G. Chen, Effects of individual and combined additions of transition elements (Zr, Ti and V) on the microstructure stability and elevated-temperature properties of Al–Cu 224 cast alloys, Mater. Sci. Eng. A 867 (2023): 144718. https://doi.org/10.1016/j.msea.2023.144718

[8] L. Cui, Z. Zhang & X. G. Chen, Development of lightweight Al-based entropy alloys for elevated temperature applications, J. Alloys Compd. 938 (2023): 168619. https://doi.org/10.1016/j.jallcom.2022.168619

[9] Q. Zhang, Z. Zuo & J. Liu, Failure analysis of a diesel engine cylinder head based on finite element method, Eng. Fail. Anal. 34 (2013): 51-58. https://doi.org/10.1016/j.engfailanal.2013.07.023

[10] M. X. Zhang, J. C. Pang, Y. Qiu, S. X. Li, M. Wang & Z. F. Zhang, Thermo-mechanical fatigue property and life prediction of vermicular graphite iron, Mater. Sci. Eng. A 698 (2017): 63-72. https://doi.org/10.1016/j.msea.2017.05.035

[11] M. J. Couper, A. E. Neeson & J. R. Griffiths, Casting defects and the fatigue behaviour of an aluminium casting alloy, Fatigue Fract. Eng. Mater. Struct. 13.3 (1990): 213-227. https://doi.org/10.1111/j.1460-2695.1990.tb00594.x

[12] A. Humbertjean & T. Beck, Effect of the casting process on microstructure and lifetime of the Al-piston-alloy AlSi12Cu4Ni3 under thermo-mechanical fatigue with superimposed high-cycle fatigue loading, Int. J. Fatigue 53 (2013): 67-74. https://doi.org/10.1016/j.ijfatigue.2011.09.017

[13] Q. G. Wang, D. Apelian & D. A. Lados, Fatigue behavior of A356-T6 aluminum cast alloys. Part I. Effect of casting defects, J. Light Met. 1.1 (2001): 73-84. https://doi.org/10.1016/S1471-5317(00)00008-0

[14] Q. G. Wang, D. Apelian & D. A. Lados, Fatigue behavior of A356/357 aluminum cast alloys. Part II–Effect of microstructural constituents, J. Light Met.1.1 (2001): 85-97. https://doi.org/10.1016/S1471-5317(00)00009-2

[15] J. F. Major, Porosity control and fatigue behavior in A356-T61 aluminum alloy, Trans. Am. Foundrym. Soc. (1998): 901-906.

[16] H. Y. Kim, S. W. Han & H. M. Lee, The influence of Mn and Cr on the tensile properties of A356–0.20 Fe alloy, Mater. Lett. 60.15 (2006): 1880-1883. https://doi.org/10.1016/j.matlet.2005.12.042

[17] H. Y. Kim, T. Y. Park, S. W. Han & H. M. Lee, Effects of Mn on the crystal structure of α-Al (Mn, Fe) Si particles in A356 alloys, J. Cryst. Growth 291.1 (2006): 207-211. https://doi.org/10.1016/j.jcrysgro.2006.02.006

[18] P. Huter, S. Oberfrank, F. Grün & B. Stauder, Thermo-mechanical fatigue influence of copper and silicon on hypo-eutectic Al–Si–Cu and Al–Si–Mg cast alloys used in cylinder heads, Int. J. Fatigue 88 (2016): 142-155. https://doi.org/10.1016/j.ijfatigue.2016.02.017

[19] S. Hegde & K. N. Prabhu, Modification of eutectic silicon in Al–Si alloys, J. Mater. Sci. 43 (2008): 3009-3027. https://doi.org/10.1007/s10853-008-2505-5

[20] S. Kumai, J. Q. Hu, Y. Higo & S. Nunomura, Effects of solidification structure on fatigue crack growth in AC4CH cast aluminum alloys, Keikinzoku 45.4 (1995): 198-203. https:// doi.org/10.2464/jilm.45.198

[21] K. Sasaki, Low cycle thermal fatigue of aluminum alloy cylinder head in consideration of changing metrology microstructure, Procedia Eng. 2.1 (2010): 767-776. https://doi.org/10.1016/j.proeng.2010.03.083

[22] M. Azadi & M. M. Shirazabad, Heat treatment effect on thermo-mechanical fatigue and low cycle fatigue behaviors of A356. 0 aluminum alloy, Mater. Des. 45 (2013): 279-285. https://doi.org/10.1016/j.matdes.2012.08.066

[23] P. Li, H. Li, X. Liang, L. Huang, K. Zhang & Z. Chen, Enhanced low-cycle fatigue and crack propagation resistance of an Al-Cu-Mg-Si forging alloy by non-isothermal aging, Mater. Sci. Eng. A 732 (2018): 341-349. https://doi.org/10.1016/j.msea.2018.07.002

[24] M. Azadi, G. Winter, G. H. Farrahi & W. Eichlseder, Comparison between isothermal and non-isothermal fatigue behavior in a cast aluminum-silicon-magnesium alloy, Strength Mater. 47 (2015): 840-848. https://doi.org/10.1007/s11223-015-9721-4

[25] H. U. Hong, J. G. Kang, B. G. Choi, I. S. Kim, Y. S. Yoo & C. Y. Jo, A comparative study on thermomechanical and low cycle fatigue failures of a single crystal nickel-based superalloy, Int. J. Fatigue 33.12 (2011): 1592-1599. https://doi.org/10.1016/j.ijfatigue.2011.07.009

[26] W. Cui, A state-of-the-art review on fatigue life prediction methods for metal structures, J. Mar. Sci. Technol. 7 (2002): 43-56. https://doi.org/10.1007/s007730200012

[27] M. Wang, J. C. Pang, S. X. Li & Z. F. Zhang, Low-cycle fatigue properties and life prediction of Al-Si piston alloy at elevated temperature, Mater. Sci. Eng. A 704 (2017): 480-492. https://doi.org/10.1016/j.msea.2017.08.014

[28] O. H. Basquin, The exponential law of endurance tests, Proc. Am. Soc. Test. Mater. Vol. 10. 1910.

[29] L.F. Coffin, Trans. ASME 76 (1954) 931.

[30] S.S. Manson, Cleveland, Lewis Flight Propulsion Laboratory, NACA, 1954, Report 1170.

[31] T. Gocmez, A. Awarke & S. Pischinger, A new low cycle fatigue criterion for isothermal and out-of-phase thermomechanical loading, Int. J. Fatigue 32.4 (2010): 769-779. https://doi.org/10.1016/j.ijfatigue.2009.11.003

[32] G. H. Farrahi, M. Azadi, G. Winter & W. Eichlseder, A new energy-based isothermal and thermo-mechanical fatigue lifetime prediction model for aluminium–silicon–magnesium alloy, Fatigue Fract. Eng. Mater. Struct. 36.12 (2013): 1323-1335. https://doi.org/10.1111/ffe.12078

[33] G. R. Halford & S. S. Manson, Life prediction of thermal-mechanical fatigue using strainrange partitioning. J. ASTM Int., 1976.

[34] R. W. Neu & H. Sehitoglu, Thermomechanical fatigue, oxidation, and creep: Part II. Life prediction, Metall. trans. A 20 (1989): 1769-1783. https://doi.org/10.1007/BF02663208

[35] J. Lemaitre and J. L. Chaboche, Mechanics of solid materials. Cambridge university press, 1994.

[36] J. L. Chaboche & P. A. Lesne, A non-linear continuous fatigue damage model, Fatigue Fract. Eng. Mater. Struct. 11.1 (1988): 1-17. https://doi.org/10.1111/j.1460-2695.1988.tb01216.x

[37] R. Minichmayr, M. Riedler, G. Winter, H. Leitner & W. Eichlseder, Thermo-mechanical fatigue life assessment of aluminium components using the damage rate model of Sehitoglu, Int. J. Fatigue 30.2 (2008): 298-304. https://doi.org/10.1016/j.ijfatigue.2007.01.054

[38] R. P. Skelton, Energy criterion for high temperature low cycle fatigue failure, Mater. Sci. Technol. 7.5 (1991): 427-440. https://doi.org/10.1179/mst.1991.7.5.427

[39] E. Charkaluk, A. Bignonnet, A. Constantinescu & K. Dang Van, Fatigue design of structures under thermomechanical loadings, Fatigue Fract. Eng. Mater. Struct. 25.12 (2002): 1199-1206. https://doi.org/10.1046/j.1460-2695.2002.00612.x

[40] J. Qin, D. Racine, K. Liu & X. G. Chen, Strain-controlled thermo-mechanical fatigue testing of aluminum alloys using the Gleeble® 3800 system, Proceedings of the 16th International Aluminum Alloys Conference (ICAA 16), CIM, Montreal, QC, Canada. 2018.

[41] J.F. Nie, B.C. Muddle, Strengthening of an Al–Cu–Sn alloy by deformation-resistant precipitate plates, Acta Mater. 56 (2008) 3490-3501. https://doi.org/10.1016/j.actamat.2008.03.028

[42] H. Li, Y. Tang, Z. Zeng, Z. Zheng, and F. Zheng, Effect of ageing time on strength and microstructures of an Al–Cu–Li–Zn–Mg–Mn–Zr alloy, Mater. Sci. Eng. A 498 (2008): 314-320. https://doi.org/10.1016/j.msea.2008.08.001

[43] J. Rakhmonov, K. Liu, and X.G. Chen, Effects of compositional variation on the thermal stability of θ′-Al_2Cu precipitates and elevated-temperature strengths in Al-Cu 206 alloys, Journal of Materials Engineering and Performance 29 (2020): 7221-7230. https://doi.org/10.1007/s11665-020-05227-5

[44] M. Wang, J. C. Pang, H. Q. Liu, S. X. Li, M. X. Zhang & Z. F. Zhang, Effect of constraint factor on the thermo-mechanical fatigue behavior of an Al-Si eutectic alloy, Mater. Sci. Eng. A 783 (2020): 139279. https://doi.org/10.1016/j.msea.2020.139279

[45] K. Liu, S. Wang, L. Pan & X. G. Chen, Thermo-Mechanical Fatigue Behavior and Resultant Microstructure Evolution in Al-Si 319 and 356 Cast Alloys, Mater. 16.2 (2023): 829. https://doi.org/10.3390/ma16020829

[46] C.W. Shao, P. Zhang, R. Liu, Z.J. Zhang, J.C. Pang, Z.F. Zhang, Low-cycle and extremely-low-cycle fatigue behaviors of high-Mn austenitic TRIP/TWIP alloys: Property evaluation, damage mechanisms and life prediction, Acta Mater. 103 (2016): 781-795. https://doi.org/10.1016/j.actamat.2015.11.015

[47] P. Guo, L. Qian, J. Meng, F. Zhang & L. Li, Low-cycle fatigue behavior of a high manganese austenitic twin-induced plasticity steel, Mater. Sci. Eng. A 584 (2013): 133-142. https://doi.org/10.1016/j.msea.2013.07.020

[48] N. Kamp, N. Gao, M.J. Starink, I. Sinclair, Influence of grain structure and slip planarity on fatigue crack growth in low alloying artificially aged 2xxx aluminium alloys, Int. J. Fatigue 29.5 (2007): 869-878. https://doi.org/10.1016/j.ijfatigue.2006.08.005

[49] K. Hockauf, M.F.-X. Wagner, T. Halle, T. Niendorf, M. Hockauf, T. Lampke,

Influence of precipitates on low-cycle fatigue and crack growth behavior in an ultrafine-grained aluminum alloy, Acta mater. 80 (2014): 250-263. https://doi.org/10.1016/j.actamat.2014.07.061

[50] H.S. Ho, M. Risbet, X. Feaugas, On the unified view of the contribution of plastic strain to cyclic crack initiation: Impact of the progressive transformation of shear bands to persistent slip bands, Acta Mater. 85 (2015): 155-167. https://doi.org/10.1016/j.actamat.2014.11.020

[51] W. W. Bose-Filho, E. R. de Freitas, V. F. da Silva, M. T. Milan & D. Spinelli, Al–si cast alloys under isothermal and thermomechanical fatigue conditions, Int. J. Fatigue 29.9-11 (2007): 1846-1854. https://doi.org/10.1016/j.ijfatigue.2007.01.006

[52] M. S. Song, Y. Y. Kong, M. W. Ran & Y. C. She, Cyclic stress–strain behavior and low cycle fatigue life of cast A356 alloys, Int. J. Fatigue 33.12 (2011): 1600-1607. https://doi.org/10.1016/j.ijfatigue.2011.07.004

[53] Z. W. Huang, Z. G. Wang, S. J. Zhu, F. H. Yuan & F. G. Wang, Thermomechanical fatigue behavior and life prediction of a cast nickel-based superalloy, Mater. Sci. Eng. A 432.1-2 (2006): 308-316. https://doi.org/10.1016/j.msea.2006.06.061

[54] M. Wang, J. C. Pang, H. Q. Liu, C. L. Zou, S. X. Li, & Z. F. Zhang, Deformation mechanism and fatigue life of an Al-12Si alloy at different temperatures and strain rates, Int. J. Fatigue 127 (2019): 268-274. https://doi.org/10.1016/j.ijfatigue.2019.06.023

[55] M. Wang, J. C. Pang, M. X. Zhang, H. Q. Liu, S. X. Li & Z. F. Zhang, Thermo-mechanical fatigue behavior and life prediction of the Al-Si piston alloy, Mater. Sci. Eng. A 715 (2018): 62-72. https://doi.org/10.1016/j.msea.2017.12.099

[56] R. Liu, Z.J. Zhang, P. Zhang, Z.F. Zhang, Extremely-low-cycle fatigue behaviors of Cu and Cu–Al alloys: Damage mechanisms and life prediction, Acta Mater. 83 (2015): 341-356. https://doi.org/10.1016/j.actamat.2014.10.002

[57] W. Deng, J. Xu, Y. Hu, Z. Huang, & L. Jiang, Isothermal and thermomechanical fatigue behavior of Inconel 718 superalloy, Mater. Sci. Eng. A 742 (2019): 813-819. https://doi.org/10.1016/j.msea.2018.11.052

Chapter 5

General conclusions and recommendations

5.1 General conclusions

This study conducted a comprehensive investigation into the influence of microalloying with Mg and TEs on the mechanical, creep, and fatigue behavior of Al-Cu alloys at elevated temperatures. The following critical conclusions can be drawn from the experimental results and analysis:

1. Microalloying with Mg enhanced the precipitation of θ′ precipitates after T7 treatment and stabilized these precipitates in the matrix by slowing down the coarsening process. This led to a finer and denser distribution of θ′ precipitates after T7A treatment. Thus, the Mg-containing alloys displayed higher thermal resistance. The improved thermal resistance of Mg-containing alloys showed higher yield strength, creep resistance and LCF performance at 300 ℃ relative to Mg-free alloy.
2. Under a wide range of applied stress in creep tests, two regimes, LSR and HSR, were observed in the creep curves for different Mg-containing alloys. These two regimes were separated by a break with different stress exponents indicating the different creep mechanisms: dislocation climbing in the LSR and Orowan looping in the HSR.
3. In fatigue tests, all the Mg-containing alloys experienced cyclic softening, with reduced fatigue lifetime at higher strain amplitudes. Interestingly, the TMF lives were inferior to the LCF lives under the same strain amplitude.

Furthermore, the addition of Mg enhanced the LCF performance of Al-Cu alloys owing to co-existing θ″ and θ′ precipitates and higher thermal stability in Mg-containing alloys; conversely, the Mg addition resulted in a small reduction in OP-TMF performance owing to the lower ductility and high tensile stress at low temperatures of Mg-containing alloys. Both the lifetimes of LCF and TMF can be accurately predicted by the hysteresis energy model.

4. Considering elevated-temperature mechanical, creep, and fatigue behaviors, the 0.24Mg alloy emerged as the optimal choice for industrial and engineering applications.
5. The addition of transition elements (Zr, Ti, and V) significantly enhanced the coarsening resistance of θ′ precipitates during 300 ℃ thermal exposure, attributed to their segregation at Al/θ′ interfaces. Among individual additions of TEs, Zr showed the best efficiency in stabilizing θ′. The efficiency was further improved by the combined addition of TEs, and the combination of Zr + V and Zr + Ti + V demonstrated the highest efficiency. Additionally, a close relationship between YS and the distribution and thermal stability of the θ′ precipitates observed in different TEs-containing alloys.
6. Creep resistance at elevated temperatures for different TEs-containing alloys was affected by the thermal stability of θ′ and grain size. Zr-containing alloys (ZrV, Zr, and TiZrV) excelled in creep resistance owing to the excellent thermal stability of θ′, whereas the Ti/V-containing alloys (Ti, V, TiV, and TiZr) showed decreased creep resistance due to their small grain size.
7. For comprehensive properties encompassing elevated-temperature YS, superior creep resistance, and fine grain structure, the 0.24Mg-TiZrV alloy

stands out as the prime choice from both industrial and engineering perspectives.

5.2 Recommendations

Based on the recent findings of this study, the following suggestions and recommendations for future work can be drawn:

1. Explore potential approaches for improving properties of Al-Cu cast alloys at elevated temperatures, specifically within the range of 350-400 ℃. For example, the addition of Sc and Zr into Al-Cu alloys has demonstrated an increased capacity to enhance the thermal resistance of θ′ at elevated temperatures. In addition, the formation of nano-sized Al_3(Sc, Zr) dispersoids, known for their stability at 300–350 ℃, provides an additional contribution to enhance the elevated-temperature properties. Hence, investigation on the influence of further addition of Sc on the elevated-temperature properties of 0.24Mg(Ti,Zr,V) alloy would be valuable.
2. Al-Cu alloys, as one newly developed cylinder head alloy, their fatigue behavior should be compared against conventional alloys such as 356 and 319 alloys. This comparative dataset can offer valuable insights for industrial and engineering applications.
3. Mechanical testing considerations suggest that performing a TMF test consumes more time than a LCF test. Consequently, the establishment of a predictive model capable of accurately estimating TMF life using parameters derived from LCF is essential.

4. In this study, the hysteresis energy was proved to have a high accuracy to predict both the LCF and TMF fatigue lifetime. However, it is important to note that the value of hysteresis energy needs to be obtained through a specific testing condition, and it is not possible to predict the fatigue lifetime at other conditions without performing tests. Hence, it is necessary to explore potential correlations between hysteresis energy and other given parameters such as strain amplitude, which will enable the prediction of fatigue lifetimes under untested conditions.

List of publications

Journal articles

1) **P. Hu**, K. Liu, L. Pan and X. G. Chen, Effect of Mg microalloying on elevated-temperature creep resistance of Al–Cu 224 cast alloys, ***Materials Science and Engineering: A*** 851 (2022): 143649. https://doi.org/10.1016/j.msea.2022.143649
2) **P. Hu**, K. Liu, L. Pan and X. G. Chen, Effects of individual and combined additions of transition elements (Zr, Ti and V) on the microstructure stability and elevated-temperature properties of Al–Cu 224 cast alloys, ***Materials Science and Engineering: A*** 867 (2023): 144718. https://doi.org/10.1016/j.msea.2023.144718
3) K. Liu, S. Wang, **P. Hu**, L. Pan, X. G. Chen, Improved Thermo-Mechanical Fatigue Resistance of Al-Si-Cu 319 Alloys by Microalloying with Mo, ***Materials*** 2023, *16*(9), 3515. https://doi.org/10.3390/ma16093515
4) **P. Hu**, K. Liu, L. Pan and X. G. Chen, Effect of Mg on the elevated-temperature low cycle fatigue and thermo-mechanical fatigue behaviors of Al-Cu cast alloys, submitted to ***Materials Science and Engineering: A*** 885 (2023):145588. https://doi.org/10.1016/j.msea.2023.145588
5) **P. Hu**, K. Liu, L. Pan and X. G. Chen, The elevated-temperature mechanical and OP-TMF behavior of Al-9Si-3.5Cu alloy, under preparation.

Conference papers

1) **P. Hu**, K. Liu, X. G. Chen, L. Pan, F. Breton, Evolution of precipitates and mechanical properties in Al-Cu 224 cast alloys with various Mg additions, ***COM 2021*** 121(2021): 105-114.
2) K. Liu, S. Wang, **P. Hu**, L. Pan, X. G. Chen, Thermo-mechanical Fatigue Behavior and Its Evolution with Mo Addition in Al-Si Cast alloys, ***COM 2023***.

Scientific posters

1) **P. Hu**, K. Liu, X. G. Chen, Enhanced high-temperature mechanical properties of Al-Cu cast alloy by microalloying with Mg, ***REGAL 2020***.
2) **P. Hu**, K. Liu, X. G. Chen, Effect of microalloying with Mg on the creep resistance of Al-Cu 224 alloy, ***REGAL 2021***.
3) **P. Hu**, K. Liu, X. G. Chen, Enhanced low-cycle fatigue resistance at elevated temperature of Al-Cu cast alloy by microalloying with Mg, ***REGAL 2022***.
4) **P. Hu**, K. Liu, X. G. Chen, The out-of-phase thermomechanical fatigue behavior of Al-9Si-3.5Cu alloys, under preparation for ***REGAL 2023***.

Appendix I

Supplementary Materials for Chapter 2

Effect of Mg microalloying on elevated-temperature creep resistance of Al-Cu 224 cast alloys

Fig. I.1 shows all the creep curves of all the experimental alloys at different applied stresses, and the corresponding minimum creep rates were summarized in Table I.1.

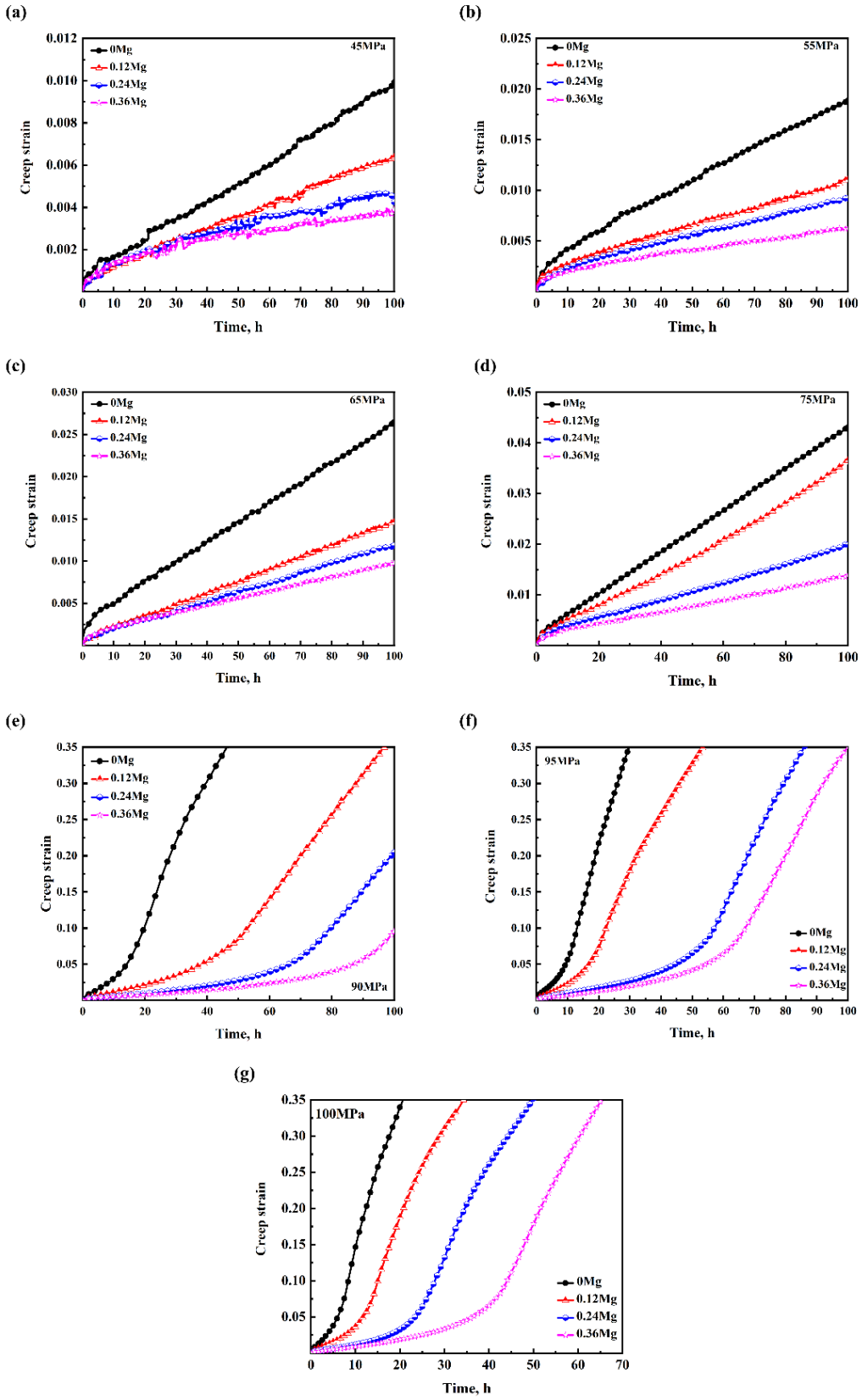

Fig. I.1 Creep curves of all the experimental alloys at different applied stresses.

Table I.1 The summary of the minimum creep rates in the second stage of all the experimental alloys.

Applied stress, MPa	Alloy	Minimum creep rate, s^{-1}	Applied stress, MPa	Alloy	Minimum creep rate, s^{-1}
45	0Mg	$1.94\times10^{-8}\pm4.22\times10^{-9}$	90	0Mg	$5.30\times10^{-7}\pm2.48\times10^{-7}$
	0.12Mg	$1.43\times10^{-8}\pm1.73\times10^{-9}$		0.12Mg	$2.72\times10^{-7}\pm3.55\times10^{-8}$
	0.24Mg	$1.09\times10^{-8}\pm2.41\times10^{-9}$		0.24Mg	$1.22\times10^{-7}\pm1.01\times10^{-8}$
	0.36Mg	$7.25\times10^{-9}\pm1.83\times10^{-9}$		0.36Mg	$7.50\times10^{-8}\pm6.16\times10^{-9}$
55	0Mg	$3.81\times10^{-8}\pm3.39\times10^{-9}$	95	0Mg	$9.28\times10^{-7}\pm2.40\times10^{-8}$
	0.12Mg	$2.25\times10^{-8}\pm2.66\times10^{-9}$		0.12Mg	$5.02\times10^{-7}\pm2.03\times10^{-7}$
	0.24Mg	$1.61\times10^{-8}\pm5.04\times10^{-9}$		0.24Mg	$2.32\times10^{-7}\pm6.81\times10^{-8}$
	0.36Mg	$1.33\times10^{-8}\pm1.99\times10^{-9}$		0.36Mg	$1.70\times10^{-7}\pm1.96\times10^{-8}$
65	0Mg	$5.39\times10^{-8}\pm1.50\times10^{-8}$	100	0Mg	$1.37\times10^{-6}\pm2.83\times10^{-7}$
	0.12Mg	$4.00\times10^{-8}\pm2.12\times10^{-9}$		0.12Mg	$7.46\times10^{-7}\pm6.36\times10^{-8}$
	0.24Mg	$3.34\times10^{-8}\pm3.35\times10^{-9}$		0.24Mg	$3.51\times10^{-7}\pm1.51\times10^{-8}$
	0.36Mg	$2.49\times10^{-8}\pm2.39\times10^{-9}$		0.36Mg	$2.53\times10^{-7}\pm1.97\times10^{-10}$
75	0Mg	$9.27\times10^{-8}\pm1.02\times10^{-8}$			
	0.12Mg	$6.24\times10^{-8}\pm1.73\times10^{-8}$			
	0.24Mg	$4.64\times10^{-8}\pm2.74\times10^{-9}$			
	0.36Mg	$3.20\times10^{-8}\pm2.41\times10^{-9}$			